Expedition 314 Site C0001[1]

Expedition 314 Scientists[2]

Chapter contents

Background and objectives

Integrated Ocean Drilling Program (IODP) Site C0001 (proposed Site NT2-03B) targets the uppermost 1000 meters below seafloor at the seaward edge of the Kumano Basin uplift (outer arc high) where the megasplay fault system branches and approaches the surface (see Figs. **F1, F2** in the "Expedition 314 summary" chapter). The Site C0001 summary log diagram is shown in Figure **F1.** Both inline and cross-line three-dimensional (3-D) seismic lines crossing Site C0001 are shown in Figure **F2.** Locations of drill holes at Site C0001 are plotted in Figure **F3** with 3-D seismic profile coverage.

The upper 1000 m drilled during this expedition provided an opportunity to access the thrust sheets uplifted by several branches of the megasplay fault system, as well as a thin overlying slope sediment cover sequence. The nature of the material in these thrust sheets was unknown. As with proposed Site NT2-01 (Sites C0003–C0005), the acoustically nonreflective nature of this section suggests that it may be composed of chaotically deformed accretionary prism sedimentary mélange transported from significantly greater depth.

The principal objective at this site was to obtain in situ density, resistivity, gamma ray values, porosity, *P*-wave velocity, and photoelectric factor (PEF) data through logging-while-drilling (LWD) and seismic-while-drilling operations. Together with later core samples, logs from this site discriminate among the structural possibilities and provide data on physical properties, strength, composition, and structure of the hanging wall of the main megasplay branch. The upper 1000 m of drilling at this site penetrated one or more subsidiary splay branches near the updip end of the splay system, affording an opportunity to compare fault development with Sites C0003–C0005.

LWD data at this site will also provide critical "pilot hole" information for later riser-based drilling. To achieve the ~3500 m total depth objective using the riser and weighted drilling mud involves setting multiple casing strings, the depth of each of which depends on the least principal stress, fracture strength of the formation, and pore fluid pressure gradient. The key part of this casing plan is the "top-hole" portion, where tolerances on mud weight are tight. Planning the casing program, therefore, requires excellent information on physical properties in the uppermost 1000 m.

Operations

Shingu, Japan, port call

Loading for three expeditions that spread out over 4 months was a huge task, and Typhoon FITOW caused delays in the original loading and laboratory rearrangement schedule at dock in Yokohama, Japan. Therefore, work at Shingu, Japan, was busy. Upon arriving in Shingu on 15 September 2007, drill pipes and drill collars were checked and listed aboard the D/V *Chikyu*. Instruments, laboratory supplies, mud chemicals, and logging tools were loaded. An official ceremony for launching the *Chikyu's* IODP operations was held in Shingu on 16 September upon arrival of the ship to port. Officials from IODP-Management International, U.S. National Science Foundation, Ministry of Education, Culture, Sports, Science and Technology of Japan, and Japan Agency for Marine-Earth Science and Technology (JAMSTEC) were in attendance. While performing maintenance on the drilling equipment, drill pipe was picked up for the first hole. The science party boarded the ship in Shingu on 19 September after undergoing helicopter underwater escape training and sea survival training at JAMSTEC headquarters in Yokosuka, Japan. A prespud meeting was held on 20 September by shipboard scientists with marine, drilling, and laboratory technical personnel. Numerous media interviews were conducted and ship tours were carried out during the port call.

Transit from Shingu to Site C0001

The *Chikyu* departed Shingu for Site C0001 at 1620 h on 21 September 2007. The 44 nmi transit was covered at an average speed of 5.06 kt. Upon arrival at the first site at 0100 h on 22 September, the ship was set in dynamic positioning (DP) mode and bighead transducers were lowered.

Hole C0001A

The summary of operations at Site C0001 is shown in Table T1. The drill string was spaced out in preparation for drilling and the Schlumberger Drilling and Measurement measurement-while-drilling (MWD) and annular-pressure-while-drilling (APWD) tools were tested in preparation for drilling pilot Hole C0001A (target depth = 1000 m LWD depth below seafloor [LSF]). The bottom-hole assembly (BHA) included a polycrystalline diamond compact (PDC) bit, crossover sub, MWD (PowerPulse) and APWD tools, stabilizer and fifteen 6¾ inch drill collars, and one jar (see Fig. F1 in the "Expedition 314 methods" chapter; Table T2). Tools were assembled and started running into hole between 0230 and 1030 h on 25

September 2007. The position of the hole was located and surveyed by remotely operated vehicle (ROV). After spud-in, drilling/MWD logging operations began at 1215 h. Based on the cumulative length of drilling pipe, the seafloor depth was estimated to be 2199.5 m (2228 m drillers depth below rig floor [DRF]).

A time version of the surface drilling parameters and downhole MWD measurements of equivalent circulating density (ECD), average annular pressure (APRS), and gamma ray value (GRM1) is given in Figure F4. The drillers attempted to maintain a 50 m/h rate of penetration (ROP). The instantaneous ROP averaged over 5 ft (1.52 m) (ROP_5ft) was higher for the first 1.75 h of drilling (0 to ~70 m LSF) because of the unconsolidated nature of the formation. After that, ROP was maintained close to 50 m/h while drilling, even though effective ROP was lower as a result of the time required to make pipe connections (every 38 m). From 380 m LSF (2330 h on 25 September), ECD and APRS sharply increased after each pipe connection and associated noncirculating time intervals. Normal ECD and APRS trends were recovered, at first within 5 min and further downhole with increased circulation time of up to 20 min. Pills of high-viscosity gel mud were regularly pumped to increase the density of the drilling fluid and to facilitate hole cleaning and stability. Characteristics of the high-viscosity gel mud are given in Table T3. At 0320 h on 26 September, major increases in ECD, APRS, and torque (from 5–7 to 15 kNm) before a new pipe connection were of major concern (~430 m LSF). A combination of backreaming, increasing pump pressure (standpipe pressure [SPPA]), and reducing surface weight on bit (SWOB) and ROP for ~2 h allowed a return to normal drilling conditions (0515 h; 520 m LSF). Drilling continued at lower ROP (22–30 m/h), reduced weight on bit (WOB), increased pump flow (from 500 to 570–590 gpm) and pumping time (dummy connection), and increased collar rotation speed (CRPM = 80–100 rpm) until the target total depth (TD) was reached at 1250 h on 27 September (after 49 h of drilling operations). The BHA was then pulled out of the hole and the drill bit cleared the seafloor at 1430 h on 27 September. The drill bit was recovered on the rig floor at 1200 h on 28 September.

Hole C0001B

Preparation for special-purpose geotechnical coring began on 29 September 2007, after a delay to change out excessively rusted drill collars. Hole C0001B was tagged at 2220 m DRF on 30 September (Table T1). Four cores were taken from the seafloor with the hydraulic piston corer system (HPCS). The top intervals

of HPCS cores are as follows (total core recovery = 30.82 m):

1. 2210 m DRF at 0400 h,
2. 2219.5 m DRF at 0645 h,
3. 2229 m DRF at 0945 h, and
4. 2238.5 m DRF at 1200 h.

Hole C0001C

Hole C0001C was the first LWD-MWD-APWD (hereafter referred to as LWD) hole drilled during Expedition 314. Operations began with making up the BHA, tool initialization, and tool calibration. The BHA included a PDC bit, various subs, LWD tools, fourteen 6¾ inch drilling collars, and one jar (Table **T3**). From bottom to top, the LWD tools (6¾ inch [17.15 cm] collars) included the geoVISION tool with a 23.18 cm button sleeve, the sonicVISION (four-receiver array) tool, the MWD (PowerPulse) tool, the seismicVISION tool, and the Azimuthal Density Neutron (adnVISION) tool (see Fig. **F1** in the "Expedition 314 methods" chapter). For the seismicVISION tool, memory and battery life are good for ~40 nonpumping hours; when circulating above 400 gpm, battery power is not used.

Installing the radioactive source for density measurement was completed at 0540 h on 1 October 2007, and the BHA was lowered to run into hole. Tool communication and function checks were conducted at 320 m DRF between 0745 and 0815 h on 1 October. At ~60 m above seafloor (1550 h on 1 October), the surface air gun array was activated and the seismicVISION tool was tested again. Simultaneously, a problem with the surface IDEAL depth recording system was found (see the **"Expedition 314 methods"** chapter). The geolograph, which tracks the position of the top drive and in-slip or out-of-slip displacement, malfunctioned but was returned to service at 1840 h. After tagging the seafloor at 2226.6 m DRF (2198.0 m mud depth below sea level [MSL]), hole position was confirmed and surveyed by ROV (1840–1915 h) (Table **T1**).

Hole C0001C was spudded at 1915 h with an initial pump rate of 550 gpm, ROP of 15–30 m/h, and bit rotation of 80 rpm. A graphic representation of the drilling parameters and gamma ray log is given in Figure **F5.** Below ~2237 m DRF (~7 m LSF), drilling proceeded with a more constant ROP of 25–30 m/h. ECD was constant at slightly <1 g/cm³. WOB and SPPA were kept to minimum while drilling this unconsolidated upper section. From 2110 h on 1 October to 0230 h on 2 October (duration = 5.33 h) drilling stopped for maintenance of rig floor equipment (leakage of wash pipe). After repairs, drilling continued at an ROP of 25 m/h. Between 2266 and 2304 m

DRF, a hole deviation survey showed that hole deviation was ~6° (6° at 2266 m and 5.45° at 2304 m). Operations stopped at 0530 h with TD at 78 m LSF. The BHA was pulled out of the hole and the hole position checked. ROV observations confirmed the pipe footprint on the seafloor was associated with pipe/hole deviation during the rig floor maintenance period while the bit was at shallow depth in unconsolidated formation. A decision to spud Hole C0001D without further delay was made at 0740 h on 2 October.

Hole C0001D

Hole C0001D was spudded at 0800 h on 2 October 2007 with the same BHA as Hole C0001C (see Table **T3**) after an ROV survey. LWD-MWD drilling/logging operations were conducted from the seafloor (2226 m DRF) to TD of 3202 m DRF (974 m LSF) after >5 days of drilling operations (Fig. **F6**). To avoid hole deviation, the BHA was jetted in to ~40 m LSF. Drilling advanced at an average ROP of 80 m/h then reduced to 25–30 m/h. WOB was kept at a minimum and SPPA was maintained slightly higher than in Hole C0001A (1.1 versus 1.0 MPa). APRS and ECD measurements show a normal (hydrostatic) trend increasing with depth until early morning on 3 October (~2700 m DRF; 470 m LSF), where the slope of the trend increased with increased bit rotation (from 75–80 to 100 rpm). Major reaming and sweeping operations with increased pump pressure and pump flow were conducted between 1245 and 1915 h because of difficult drilling conditions (sticky hole conditions from 2730 to 2773 m DRF; 502 to 545 m LSF). High SPPA was maintained (>15 MPa) for the remaining duration of drilling. The ROV observed stick-slip rotation of the drill pipe above seafloor below this interval. At 0730 h on 4 October, the bit was raised to 2600 m DRF (372 m LSF) for rig floor maintenance of the wireline blow-out preventer line (until 1615 h; duration = 8.75 h), followed by reaming and sweeping of the hole (until 2150 h; duration = ~2.5 h). From 2600 m DRF (372 m LSF), drilling operations continued with routine hole cleaning operations at each pipe connection. ECD decreased smoothly back to 1.2 g/cm³ and remained stable while ROP was reduced to ~15 m/h. At 1200 h on 7 October, the bit reached 3202 m DRF (974 m LSF), 26 m less than the planned TD for this hole. At this point, the DP system computer experienced a series of malfunctions and a red alert DP alarm sounded at 1126 h. The decision was made to trip out of the hole as quickly as possible. Tools were pulled out of the hole and, after having removed the radioactive source (at 0100 h on 7 October), all tools were recovered on the rig floor.

Transit to Site C0002

After pulling out of the hole because of the DP system failure, troubleshooting of the DP system took 6 days. Finally, approval to continue operations was received on 12 October 2007. At 2100 h on 12 October, the *Chikyu* moved 14 nmi northwest of the Site C0001 at 3.4 kt to avoid running the LWD tool string in a strong current. After assembling the LWD BHA and drill pipes to a depth of 700 m, the ship drifted to the location of Site C0002 with 1.5 kt speed at 1430 h on 13 October. Upon arrival at Site C0002 at 2145 h, the ship was set in DP mode.

Data and log quality

Hole C0001A

Available data

Hole C0001A was drilled with the MWD-APWD tools installed in the drill string. All data were sent to the surface by the drilling fluid telemetry system (see Fig. **F3** and text in the **"Expedition 314 methods"** chapter). At the end of the drilling operation, time and depth information were merged and data were processed following the data flow presented in **"On-board data flow and quality check"** in the "Expedition 314 methods" chapter. Data included

1. Surface drilling control parameters: ROP (m/h), hook load (HKLD) (kkgf), SWOB (kkgf), and standpipe pressure (SPPA) (psi);
2. Downhole drilling parameters: drill bit (collar) rotation (CRPM_RT) (rpm), PowerPulse turbine rotation speed (TRPM_RT) (rpm), stick-slip (STICK_RT) (rpm) and shock indicators (shock risk [SHKRSK_RT], and shock peak [SHKPK_RT]) (g);
3. Annular pressure data: average annular pressure (APRS_MWD) (psi), annular temperature (ATMP_MWD) (°C), and equivalent circulating density (ECD_MWD) (g/cm³); and
4. Gamma ray values (GRM1) (gAPI) for further depth correlation over the depth interval (2181.75–3227.83 m DRF; 0–101.43 m LSF).

Depth shift

For this hole, the mudline (seafloor) was identified from the first break in the GRM1 log found at 2226.4 m DRF (Fig. **F7**). The GRM1 log is particularly noisy at the seafloor interface because the fast ROP (jet-in) in the unconsolidated formation is incompatible with a reliable statistical count of the radioactive elements of the formation and possible flow of mud around the bit. Despite all sources of uncertainty, the chosen value shows an acceptable discrepancy of –1.6 m with respect to water column height based on cumulative

pipe length. The depth-shifted version of the surface and downhole drilling data and downhole ECD, APRS, and GRM1 logs are given in Figure **F8.** To help correlate time and depth versions of the data, the time-depth relationship for Hole C0001A is given in Figure **F9.**

Logging data quality

Except for the GRM1 log of the MWD tool, which is directly related to the formation properties (lithology), all other logs are direct surface drilling and downhole measurements. APRS and ECD derived from APRS expectably increase with depth, except between 430 and 520 m LSF, where drillers had to combine backreaming, increased pump pressure (SPPA), and reduced SWOB and ROP to increase circulation. As GRM1 has a high depth of investigation, it is considered reliable despite the lack of hole shape (caliper) data. No repeat data were available in this hole, but we will later show that the GRM1 log correlates well with the gamma ray log of the geoVISION resistivity (GVR) tool in Hole C0001D except for a few depth intervals discussed in the next section.

Holes C0001C and C0001D

Available data

Holes C0001C and C0001D were drilled with LWD-MWD-APWD tools installed in the drill string. Similar to Hole C0001A, all MWD-APWD data were transmitted in real time, including a limited set of LWD data. This data set includes bulk density (RHOB_DH_ADN_RT) and bulk density correction (DRHO_DH_ADN_RT) computed downhole (with a less sophisticated algorithm than the one used at the surface with the memory data); thermal neutron ratio (TNRA_ADN_RT) and thermal neuron porosity (TNPH_ADN_RT); average borehole diameter from the ultrasonic caliper (ADIA_ADN_RT); gamma ray (GR_RAB_RT) and resistivities (bit [RES_BIT_RT], ring [RES_RING_RT], shallow [RES_BS_RT], medium [RES_BM_RT], and deep [RES_BD_RT]) from the GVR tool; hole deviation data such as relative bearing (RB_RT); hole azimuth (HAZI_RT), and hole deviation (DEVI_RT); sonic compressional Δt; and semblance (DTCO and CHCO) from the sonic tool (see Table **T2** in the "Expedition 314 methods" chapter). As previously stated in **"Operations,"** real-time transfer of seismic data failed because of problems with the downhole picking of wave arrivals in a high-noise environment.

When LWD tools were recovered on the rig floor, various problems were encountered that required modifying the data flow presented in Figure **F8** in the "Expedition 314 methods" chapter. Figure **F10** il-

lustrates the data flow used for Holes C0001C and C0001D. Memory data from the geoVISION were successfully downloaded and converted to depth. Sonic data were downloaded, but merging downhole time data with surface time-depth information initially failed. Both files were sent to Schlumberger's shore base in Shekou (China) for depth conversion preprocessing and then were sent back to the ship for further processing and analysis. Downloading data from the adnVISION tool was impossible on board because of damage to the output port on the tool; therefore, in an attempt to download the data, the tool was sent to the Shekou base. The memory data from the adnVISION tool were returned to the *Chikyu* shortly before the end of Expedition 314. The seismicVISION tool experienced a similar problem and was sent to the Schlumberger SKK Drilling and Measurement Center (Fuchinobe, Japan), where the data were successfully downloaded and sent back to the ship by file transfer protocol for onboard processing and analysis.

Drilling in Hole C0001C was aborted after <9 h of operation (including ~5 h of rig floor equipment repair) (see "Hole C0001C" in "Operations"). MWD, real-time, and memory data from the geoVISION, sonicVISION, and seismicVISION tools cover the depth interval 0–74 m LSF. Because of poor velocity contrast between mud and formation velocity (to ~200 m LSF), sonic data from Hole C0001C have not been processed, though raw waveforms are available at sio7.jamstec.go.jp. Only one check shot above seafloor was acquired at this site (see "Log-seismic correlation"). adnVISION memory is presently unavailable, with only a limited set of real-time data available for Hole C0001C. For Hole C0001D, transfer of adnVISION real-time data to the surface was lost below 510 m LSF, limiting the set of available data to real-time MWD and memory geoVISION, sonicVISION, and seismicVISION data from 0 to 973 m LSF (2193 to 3201 m DRF). adnVISION memory data for 0–510 m LSF were eventually recovered. However, no memory data for the hole below 510m LSF could be recovered.

Depth shift

For Holes C0001C and C0001D, the mudline (seafloor) was identified from the first break in the gamma ray (GR) and resistivity (RES_RING, RES_BIT, RES_BD, RES_BM, and RES_BS) logs (Figs. F11, F12). In Hole C0001C, the mudline was picked at 2230.5 m DRF, a 4 m discrepancy from drillers depth (2226.5 m DRF). In Hole C0001D, the mudline was picked at 2228 m DRF, again differing from drillers depth, this time by 2 m (2226 m DRF). For both holes, uncertainty in picking the mudline is clearly

within ±1 m because the top few meters of the unconsolidated formation was washed out by drilling fluid and resulted in mixing (formation suspension) at the mudline interface, blurring gamma ray and resistivity readings.

For Holes C0001C and C0001D, the depth-shifted versions of the main drilling data and geophysical logs are given in Figures F13 and F14, respectively. Figures F15 and F16 present the time-depth relationship linking the time (Figs. F5, F6) and depth (Figs. F13, F14) versions of the data from Holes C0001C and C0001D.

Logging data quality
Hole C0001C

Figure F13 shows the quality control logs for Hole C0001C LWD data. The target ROP of 30 m/h (±5 m/h) was generally achieved until 36.6 m LSF, where rig floor maintenance stopped drilling operations for 5 h (see "Hole C0001C" in "Operations"). Drilling continued at a slightly lower ROP (20–25 m/h) until operations stopped completely at 74 m LSF because of hole deviation exceeding 6°. This ROP was sufficient to record 1 sample per 4 cm over the majority of the hole. WOB was minimal (approximately null in the upper 35 m LSF and ~2 kkgf below). SPPA was maintained at 1.2 MPa for the entire drilling period, and no noticeable change in APRS and ECD was observed.

Time after bit (TAB) measurements were taken at time intervals of ~5 min for ring resistivity and 4 min for gamma ray logs, except in a short depth interval that corresponds to the 5 h of rig floor repairs. Theoretical TAB measurements for density and neutron porosity in this interval are ~43 and 46 min, respectively. Note that these values have been computed because (1) the data themselves have not been transmitted in real time (not selected) and (2) the memory data are not available at the time of this writing; however, density and porosity measurements had been selected to be transferred in real time and are thus available. Memory data were recovered late in Expedition 314 and provide actual TAB data. The real-time density caliper log (ADIA), which gives the average diameter of the LWD borehole, is the best indicator of borehole conditions. The density caliper log, which should measure a value of 8.5 inches (21.6 cm) for a perfect in-gauge hole, instead shows values ranging between 9 and 10 inches. (22.9–25.4 cm) for the entire depth interval (0–74 m LSF) except between 5 and 11 m and between 33.5 and 46 m LSF, where noticeable washouts (ADIA = >10 inches [25.4 cm]; standoff = >1.5 inches [3.8 cm]) were detected. These washouts are associ-

ated with major decreases in the bulk density log (RHOB), where bulk density corrections (DRHOB) could not be fully compensated for this major washout and are thus underestimated (Fig. F13). Otherwise, a standoff <1 inch (2.5 cm) between the tool and the borehole wall indicates high-quality density measurements with an accuracy of ±0.015 g/cm³.

Comparison between deep button (RES_BD) and shallow button (RES_BS) resistivity values shows that drilling fluid invasion is null or not significant, confirming the short TAB readings.

Based on experience gained in Hole C0001D (see next section), sonic data were not processed because the velocity contrast between mud and formation is too low throughout the uppermost 200 m LSF.

The quality of GVR images is good, but images suffered from hole ovalization and/or tool eccentricity resulting from hole deviation. No significant resolution loss is observed with variation in ROP except in the shallow section (first couple of meters) where the images were degraded by the rapid ROP and low rotation rate of the bit.

Hole C0001D

Figure F14 shows the quality control logs for the Hole C0001D LWD data. To avoid deviation of the hole as with Hole C0001C, the hole was started with rapid jetting-in (0–55 m LSF). Except for this shallow depth interval, the target ROP of 25 m/h (±5 m/h) was achieved to 340 m LSF. Effective ROP then slightly decreased with local increases in APRS and ECD, requiring minor backreaming (340–520 m LSF). Concomitant with the major increases in APRS and ECD, an increase in SPPA and a decrease in ROP was necessary to maintain drilling fluid circulation (from 520 to TD = 972 m LSF). For this lower depth interval (520–972 m LSF) increased SWOB was necessary to compensate for increasing stick-slip, which was particularly high (>200 rpm) in the high-ECD zone (520–580 m LSF) with a high level of shocks (740–920 m LSF). At ~575 m LSF, the hole slightly deviated by 2°, but hole deviation never exceeded 4° to TD.

Except during pipe connections, backreaming, and wiper trips, TAB measurements are ~5–10 min for ring resistivity and 4–8 min for gamma ray logs. Theoretical TAB measurements are ~40–60 min for density/porosity; however, while real-time density and neutron porosity logs are available, they are limited to the upper section of the hole (0–510 m LSF). adnVISION memory data for 0–510 m LSF were obtained shortly before the end of Expedition 314. All adnVISION memory and real-time data below 510 m LSF were lost because of tool failure. The ADIA log,

which is indicative of borehole condition, is also limited to this depth interval. Except for the 40 m where caliper readings are unreliable, the density caliper shows almost in-gauge value (standoff between tool and the formation = ~1 inch [~2.5 cm] to 190 m LSF). From 190 to 480 m LSF (loss of real-time data) the ADIA is highly anticorrelated with the RHOB, especially where ADIA exceeds 10 inches (25.4 cm) and where DRHOB is underestimated (Fig. F14).

To fill the gap in ADIA and further assess borehole conditions below 480 m LSF, a comparison between natural gamma ray logs from Holes C0001A (GRM1, MWD tool, and real time) and C0001D (GR, GVR tool, and memory), horizontally separated by ~65 m, is presented in Figure F17. To ~500 m LSF, GRM1 and GR are particularly well correlated, at least at a meter scale, confirming proper reading of both tools. Correlation remains relatively high from 500 to 875 m LSF, except in the following depth intervals: 530–590, 625–650, 730–750, 780–860, and 900–925 m LSF, where GR (Hole C0001D) is lower than GRM1 (Hole C0001A). Careful inspection of the depth and time version of the data reveals that low GR with respect to GRM1 corresponds to periods of SPPA and low ROP in Hole C0001D, suggesting washouts at these depth intervals. SPPA in Hole C0001D is between 15 and 17 MPa, slightly above (1–2 MPa) SPPA in Hole C0001A (note the significant shift in SPPA by ~4 MPa between 522 and 556 m LSF), but most importantly the ROP in Hole C0001D is significantly lower (mostly below 15 m/h) than in Hole C0001A (mostly above 15 m/h). Major decreases in sonic *P*-wave velocity (V_P) and resistivity for the two largest intervals (530–590 and 780–860 m LSF) favor this interpretation. Major potential washouts are identified in orange and minor potential washouts in yellow. Scalar logging data in these depth intervals must be interpreted with caution.

As for Hole C0001C, comparison between RES_BD and RES_BS resistivity values shows that drilling fluid invasion is null or not significant (even with a slightly lower ROP than in Hole C0001C) and confirm short TAB readings.

The sonicVISION data for Hole C0001D were processed on board the *Chikyu* by the Schlumberger Data Consulting Services (DCS) specialist, using two primary filtering sequences. The first "wide" sequence uses a broad bandwidth filter and the second "leaky-P" sequence uses a narrow filter designed to pass leaky *P*-wave mode arrivals. The composite sonic velocity curve that the DCS specialist prepared for this site includes data from both processed logs (Table T4). In the upper half of the hole from 0 to 524 m LSF and below 874 m LSF, the wide data were

superior and were used to assemble the composite log. From 524 to 874 m LSF, the data from the wide and leaky-P processing were used in the composite.

Quality control analysis of the sonic data is based on examination of the plots showing sonic waveforms and slowness coherence images for the common receiver data and common source data (Figs. F18, F19, F20, F21, F22, F23).

The sonic data from 0 to 175 m LSF show a strong arrival with slowness expected for waves traveling in drilling fluid (an example of data in this interval is shown as "mud arrival" in Fig. F18). This arrival is expected to be large when the formation velocity is very low. We see no sign of a distinct arrival from the formation. We conclude that the formation velocity must be near that of the mud because if it were higher it would be more distinct. The interval 175–325 m LSF is a region in which there is a clear formation arrival distinct from the mud arrival (examples of data in this interval are shown in Figs. F19, F20). The sonic data seem quite continuous and reliable. There is a narrow zone from 192 to 202 m LSF in which the formation slowness drops back into the mud arrival. It is unclear whether this signal is an increase in slowness or a washout in the hole. The interval between 325 and 476 m LSF (Fig. F21 shows an example of data from this interval) is characterized by reasonably continuous slowness coherence broken by occasional gaps one to several meters thick. The picks in these gaps are usually higher slowness than the neighboring reliable picks. This creates apparent fluctuations in velocity that would be detrimental to the creation of synthetic seismograms. From 476 to 874 m LSF the gaps between reliable picks become larger, until the gaps dominate (an example of data in this interval is shown in Fig. F22). At this point, the sonic log is unreliable if used as is, although there are probably good values to be identified by using the coherence plots. From 874 m LSF to the deepest point reached by the sonicVISION tool at 964 m LSF the data improve. The picks are clear and fairly continuous (an example of data in this interval is shown in Fig. F23).

The following comments on the processed sonicVISION data were provided by the Schlumberger DCS specialist:

> The compressional slowness curve was labeled based on the basic idea of making a continuous curve. Therefore, for intervals where both monopole *P*-wave/*S*-wave (MPS)-wide, and leaky-P processed data have low coherence and are hard to pick, I labeled it along the basic trend of coherence.

> Above 172 m LSF, it's hard to say whether labeled slowness is formation compressional or

mud arrival. I suggest that it is the mud arrival, because its slowness value is more or less constant at 200 µs/ft.

> Meanwhile, considering very slow formation with a slowness close to mud, mud arrival could have some interference with the formation signal.

> Velocities in the interval 422 to 872 m LSF are less accurate. In this interval, slowness was picked using both the MPS-wide but also leaky-P processed data. While the leaky-P processing strongly attenuates noise traveling through the mud and the tool, leaky-P transmission is dispersive and this can lead to poor picks if the filter band-pass is not exactly right.

> Note leaky-P processing is applicable only to very slow or extremely slow formations and should not be used to process data for fast or intermediate formations.

Overall, the quality of the resistivity image data is good in Hole C0001D (Fig. F14; Table T5). Except for two short intervals (541–543 and 602–603 m LSF) showing a stick-slip vertical line indicative of nonrotation of the GVR tool/stick-slip, consistency in image quality between the shallow, medium, and deep data is indicative of good quality. From 529 to 629 m LSF, where hole problems occurred, data losses are more common, but even in this section the general structural patterns are apparent. Interpretation of resistivity image data is further discussed in "Structural geology and geomechanics."

Log characterization and lithologic interpretation

Log characterization and identification of logging units

Hole C0001C

Hole C0001C was drilled as the initial hole for LWD data; however, it was terminated at 78 m LSF because of poor hole conditions and inclination of the borehole (see "Operations"). Resistivity images are affected by the inclination of the borehole, and hence, the dynamic response in particular exhibits conductive and resistive striping of the borehole wall. Resistivity peaks in the lower section (~50–70 m LSF) correspond to slight lows in the gamma ray log response and could represent higher contents of sand-sized particles (either terrigenous sand or volcanic ash). Also present in the image logs are small conductive patches that may be reduction spots. Distinct horizontal conductive-resistive-conductive bands (~1 m thick) typically correspond to a peak and dip in the

button resistivity responses. These features may be artifacts, as there are no corresponding changes in the gamma ray or density log responses (Fig. F24). Overall, the characteristics of Hole C0001C are similar to those of Hole C0001D, Subunit IA (see next section).

Hole C0001D

We separated data from Hole C0001D into logging units on the basis of visual inspection of the gamma ray log and from resistivity log responses and images. The real-time density log was available to 500 m LSF. Based on the caliper log, however, only the upper 200 m LSF section was thought to be reliable, and it was not used for logging unit characterization. The overall log responses of both gamma ray and resistivity increase with depth. These vertical patterns may be a manifestation of compaction. The three primary logging units were defined based on contrasts in the log baselines and trends. The sonic traveltime log exhibited similar large-scale trends, where reliable (see "Data and log quality"). The three primary logging units were divided further into eight logging subunits (Table T6). Although the reasons for variation are not always obvious, statistical investigation of these units confirmed their distinctiveness (Fig. F25).

The real-time caliper log showed good borehole quality for the upper 200 m LSF before degrading slightly with some variability for the rest of the recorded section. The good-quality section falls within logging Unit I (0–198.9 m LSF). This interval exhibits fairly low and consistent values on both the gamma ray and resistivity logs. Near the base of logging Unit I, logging Subunit IB (190.5–198.9 m LSF) is characterized by a distinct series of strong negative and weak positive peaks in the gamma ray log. These responses could be due to interbeds of silt or sand-sized material with clay-rich sediment. A distinct increase in the gamma ray log baseline and a gradually increasing trend with depth define logging Unit II (198.9–529.1 m LSF). The resistivity values exhibit a small baseline increase but are similar to those in logging Unit I and remain fairly constant throughout the unit. Logging Unit II exhibits subtle internal variation and is divided into three subunits. Statistically, logging Subunits IIA (198.9–344.0 m LSF) and IA are similar, whereas logging Subunits IIB (344.0–434.7 m LSF) and IIC (434.7–529.1 m LSF) are similar in their resistivity profiles. However, they exhibit large enough changes in gamma ray and sonic profiles to justify statistical separation (Fig. F26).

The boundary between logging Units II and III (529.1–976 m LSF) coincides with a systematic change in the log characteristics (Fig. F27); all the curves below the boundary show strong increasing trends. In detail, however, the boundary is transitional and includes a highly fractured interval (see "Structural geology and geomechanics"). Logging Subunit IIIA (529.1–628.6 m LSF) displays large statistical variability in all the logs, and high-frequency fluctuations can be seen on the logs and images. Logging Subunits IIIB (628.6–904.9 m LSF) and IIIC (904.9–976 m LSF) are statistically well constrained but exhibit much higher ranges in gamma ray and resistivity log values and lower mean sonic traveltimes than other logging units and their subunits (Figs. F25, F26).

Log-based lithologic interpretation

Logging Unit I (slope sediments)

Logging Unit I consists of slope sediments that are well imaged by the seismic data (see "Log-seismic correlation"). Logging Subunit IA is characterized by nearly constant gamma ray values and gradually increasing resistivity. Small ranges of variation in log response indicate uniform lithology. Borehole images show that the sediments in logging Subunit IA are composed of alternating beds of relatively conductive and resistive layers a few decimeters to a few meters thick. Sedimentary structures cannot be recognized by borehole images because of the inadequate resolution of RAB images (see "Structural geology and geomechanics").

Changes in gamma ray values in logging Subunit IA include four decametric cycles at intervals 0–54, 54–100, 100–156, and 156–191 m LSF (Fig. F28). Gamma ray values gradually increase with depth in the upper three intervals, and several meter-scale cycles are also observed within the interval. Most of these cycles are characterized by decreasing gamma ray values uphole. The lowermost interval (156–191 m LSF) is characterized by higher frequency submeter-scale gamma ray fluctuations. The four main cycles may reflect abrupt changes in the sedimentary sequence, including the formation of subtle angular discontinuities in the seismic section (Fig. F29), but they are not necessarily a result of changes in sediment composition or texture.

Log-core correlation at Ocean Drilling Program (ODP) Site 808 off Shikoku Island (Mikada, Becker, Moore, Klaus, et al., 2002) provides some constraints on our interpretation of lithology for logging Unit I in Hole C0001D. Gamma ray values in Hole C0001D, logging Subunit IA, range from 56 to 64 gAPI (Fig. F28), similar to those of Site 808 logging Subunits 2a and 2c (58–66 gAPI) and different from the values of 38–55 gAPI seen in Site 808 logging

Unit 1 (Table T7). Therefore, the lithology in logging Subunit IA could be silty sediments and hemipelagic mud.

Alternating beds of conductive and resistive sediment characterize logging Subunit IB. A negative peak on the gamma ray log to ~20 gAPI occurs in the lower part of this subunit, which is consistent with sandy sediments. The layers evidently dip to the north and gradually steepen with depth. No significant structural discontinuities can be observed at the top and bottom of this subunit; therefore, we interpret the base of logging Subunit IB as an unconformity between slope sediments and the accretionary prism (see "Structural geology and geomechanics").

Logging Units II and III (accretionary prism sediments)

Logging Unit II is divided into three subunits. In logging Subunit IIA a general increase in gamma ray and resistivity suggests a gradual decrease in porosity with depth. The gamma ray log also indicates possible meter-scale cycles. In the lower part of logging Subunits IIB and IIC, the gamma ray and other logs exhibit at least five different lower frequency, sharp-based, decameter-scale sequences. Sequences of both decreasing and increasing gamma ray values can be identified (Fig. F28). The uppermost section of logging Subunit IIB does not show the same clear pattern, but a sharp change in dips within that section may indicate structural overprint on original depositional features. Higher frequency variations inside these subunits outline minor sequences of gently increasing gamma ray values.

Changing trends in bedding dips within logging Unit II are probably related to structural deformation (possible tilting and rotation) given the abrupt changes of dip and direction without noticeable changes in composition (Fig. F29). Interpretation of the resistivity images suggest the presence of tilted blocks with varying dip angles and azimuths. Dominant bedding dips identified on the images are roughly south-dipping and changing to other orientations at tilted and/or deformed intervals.

There is very little evidence to constrain interpretations of lithology within logging Unit II. However, if we compare the gamma ray values to those for Site 808 logging Subunit 4a, they are similar (Table T7). Also noteworthy at Site 808 was the presence of breakouts in hemipelagic mud intervals. In Hole C0001D breakouts are confined to logging Units I and II. This favors hemipelagic mud as the likely lithology for logging Unit II.

Interpretation of the "transitional section" from logging Unit II to Unit III (Subunit IIIA) is subject to un-certainties indicated by drilling-related borehole damage and also by the effect of fractures intersecting the borehole wall, as clearly seen on the resistivity images (Fig. F27). The increased gamma ray values at these points mask and overprint the signature of the possible original sedimentary features on the logs. The base of logging Subunit IIC is also strongly affected by fracturing.

Logging Unit III displays the most distinctive features of the entire section drilled in Hole C0001D: increased resistivity as shown on the static processed resistivity images, overall increased gamma ray values, increased resistivity, and sonic traveltime average values that drop at the depths where the hole was intersecting faults and fractures (650, 800, 835, and 860 m LSF). The images show no evidence of intense deformation below 885 m LSF.

Logging Subunit IIIC and the lowermost part of logging Subunit IIIB exhibit more homogeneous base values in comparison to the overlying section. This suggests a difference in sedimentary and depositional features between the upper subunits of logging Unit III and the lower subunits. However, there is currently insufficient evidence to determine the lithology of Unit III.

Physical properties

This section presents physical property measurements acquired at Site C0001. Because the adnVISION tool failed, the image-derived density data (IDRO), and neutron porosity data (TNPH) could only be retrieved from the uppermost 506 m. Resistivity and *P*-wave velocity were successfully retrieved for the full borehole depth.

Density

The IDRO data for Hole C0001D are plotted in Figure F30. In the 0–44 m LSF interval, the density values in Hole C0001D are highly scattered between 1.1 and 1.7 g/cm³, with a somewhat decreasing trend with depth. However, these data may not be very reliable, partly because the LWD tools were jetted in for the first 70 m. Below 44 m LSF, Hole C0001D density values are scattered between 1.6 and 1.8 g/cm³ until reaching ~160 m LSF. Note that the density between 80 and 160 m LSF remains almost constant at 1.7 g/cm³.

Density increases from ~1.7 g/cm³ at 160 m LSF to ~1.8 g/cm³ at 196.6 m LSF. Within logging Subunit IB, the log shows a sudden drop in density value to ~1.1 g/cm³. There is a significant density contrast between formations immediately above and below the logging Unit I/II boundary. Density of the lower for-

mation is ~0.1 g/cm³ lower than that of the upper formation. Below 200 m LSF the scatter in the density log gradually increases. The span of the scattering is ~1.5–1.8 g/cm³ between 280 and 340 m LSF and increases to ~1.5–1.9 g/cm³ between 340 and 470 m LSF. The density decreases between 470 and 490 m LSF and increases finally to ~1.8 g/cm³ at the bottom of the hole.

Neutron porosity

TNPH data are highly scattered (Fig. F31). The porosity data were smoothed using a 4.5 m running average to reduce scattering.

The overall trend of the Hole C0001D neutron porosity curve is characterized by a slightly decreasing trend with depth. The neutron porosity log steadily decreases from the seafloor to reach ~60% at 190 m LSF (base of logging Unit I). A marked increase in porosity occurs at the boundary between logging Units I and II, where it increases from 60% to as much as 68% across the 30 m interval from 190 to 220 m LSF. Then in logging Unit II, porosity decreases gradually from ~68% at 220 m LSF to ~59% at 465 m LSF. In the interval between 465 and 485 m LSF, porosity increases again to 75% then decreases to 62% at 490 m LSF. Below 490 m LSF the porosity log increases again to 66% at the bottom of the hole.

The overall TNPH porosity values appear to be high compared to those normally seen at other sites in the Nankai accretionary prism (e.g., sites drilled during ODP Legs 190 and 196 at similar depths).

Resistivity and estimated porosity

Resistivity logs

Figure F32 shows the smoothed logs of the five different resistivity measurements: ring; bit; and shallow, medium, and deep button resistivity. A moving average using a 21 point (~3 m interval) window was applied to smooth the resistivity values. It highlights the differences among different resistivity measurements. Superposition of the deep, medium, and shallow button resistivity measurements shows generally very good agreement. The bit resistivity measurement integrates a larger volume of formation than the button and ring resistivities, thus producing a smoother signal.

More systematic comparisons between different resistivity logs were made through cross correlations between them. Figure F33 shows two resistivity cross-plots: bit and ring resistivity and shallow and deep button resistivity. The ring resistivity is systematically higher than the bit resistivity. Although their difference is ~0.05 Ωm at low resistivity (<1.5 Ωm), it increases to as much as 0.3 Ωm as the formation re-

sistivity increases (>1.5 Ωm). These highest values of resistivity correspond to the deepest part of the hole and the highest temperatures. The bit resistivity provides a measurement in a volume less affected by borehole freshening (caused by cold drilling fluid) than the ring measurement because of its position in the tool assembly and its greater depth of investigation. This may explain the systematic lower resistivity of the ring measurement compared to the bit measurement. The cross-plot between shallow and deep button measurements (Fig. F34) also indicates that in the range of medium resistivity (1.5–2.5 Ωm) the difference between the two measurements is negligible. This difference increases below 1.5 Ωm such that the deep resistivity is 0.2 Ωm higher than the shallow resistivity and decreases above 2.5 Ωm such that deep resistivity tends to become lower than shallow resistivity. This difference, however, still remains within the scatter.

A comparison of the five available resistivity logs is shown in Figure F35. High noise levels in the upper 70 m LSF may be artifacts of jetting in without rotation. The downhole trends seem to be identical for the five logs. Because the bit resistivity log shows the least scatter and can represent the formation resistivity better than the others because of the greatest depth of investigation, the following description is based on the bit resistivity log.

Resistivity values generally increase with depth. In logging Unit I, resistivity values gradually increase from 0.9 to 1.1 Ωm. At the base of this logging unit (173–191 m), resistivity slightly increases by ~0.1 Ωm. This evolution is followed by the logging Unit I/II boundary, where the resistivity values fluctuate between ~0.3 and 1.7 Ωm. Logging Unit II is characterized by a nearly constant resistivity value overall, with a slightly increasing trend of resistivity from 1.02 to 1.22 Ωm over logging Subunits IIA and IIB and a virtually constant resistivity (average ~1.1 Ωm) in logging Subunit IIC. This logging unit is followed by the transition zone (Subunit IIIA), which is characterized by a higher degree of variation in the resistivity signal. Logging Unit III is generally characterized by a clear increasing trend of resistivity from 0.9 to 2.4 Ωm. Only in the interval between 815 and 855 m LSF was a marked decrease in resistivity value observed.

Estimation of temperature profile

The in situ temperature profile was estimated from the regional surface heat flow of 60 mW/m² (Kinoshita et al., 2003), and assuming 1 W/(m·K) thermal conductivity for the upper 200 m LSF and 1.5 W/(m·K) below 200 m LSF and 2°C surface temperature. The resulting temperature reaches 45°C at 973 m LSF.

Estimation of porosity from resistivity

The TNPH and IDRO data only extend to half the borehole depth. Thus, an estimate of porosity from the resistivity data is proposed in this section using Archie's law, as explained in the "Expedition 314 methods" chapter, including the borehole temperature effect on fluid resistivity. This transformation has been calibrated with porosities measured on cores from the Muroto transect of the Nankai prism at Sites 1175, 1176, and 808, the only ones available at that time. The structural position of Site C0001 in the Kumano transect is somewhat intermediate between the positions of Sites 1175 and 1176 and Site 808 in the Muroto transect. The values of the Archie's law parameters necessary to best fit these data are $a = 1$ and $m = 2.4$ (Fig. F36). It should be noted again that the resistivity-derived porosity estimate is not intended to provide the "true" porosity but remains a very useful estimate, especially below 500 m where no other data exist.

From the seafloor to the boundary between logging Units I and II, the resistivity-derived porosity decreases gradually to ~52% at 196 m LSF (Fig. F37).

The resistivity-derived porosity log derived from the bit resistivity measurement presents a steep increase from 52% at 196 m LSF to 55% at 200 m LSF with a local peak of 58% at 197.8 m LSF.

Below 200 m LSF, the resistivity-derived porosity decreases with depth to ~46% at 428 m LSF. There is an abrupt increase to 48% at 438 m LSF, with a 51% peak at 434.5 m LSF. Below 438 m LSF, the resistivity-derived porosity decreases slowly again to 45% at 528 m LSF (1 m above the base of logging Unit II).

At 534 m LSF resistivity-derived porosity jumps from 45% to 50% over a 1 m interval. Beneath this interval, there is a zone of rapid decrease, reaching ~40% at 633 m LSF. This zone includes two wide oscillations of ~5% amplitude, each spanning a 20–25 m depth interval, which could be attributed to the disrupted zone identified in the resistivity images but could also be attributed to poor hole conditions.

Below 633 m LSF, the resistivity-derived porosity decreases more gently, reaching 31% at 969 m LSF. A notable deviation from this trend occurs between 810 and 910 m LSF, where it increases from ~34% at 810 m LSF to ~37% at 859 m LSF and then decreases rapidly to rejoin the overall gently decreasing porosity trend.

In summary, the profile presents an abrupt step at 200 m LSF to higher values and two zones significantly departing from the general decreasing trend, which are characterized by a relative increase in value (428–633 and 810–910 m LSF).

A porosity profile was also calculated using IDRO (see the "Expedition 314 methods" chapter). The comparison of the resistivity-derived porosity with TNPH and the porosity derived from IDRO shows that the resistivity-derived porosity only fits IDRO-derived porosity well in logging Unit I. In logging Unit II, the resistivity-derived porosity mimics the evolution of the lowest values of IDRO-derived porosity. The difference between the two logging units may be a consequence of significant lithologic change (Fig. F37).

P-wave velocity

Sonic *P*-wave velocity was calculated from compressional wave slowness logs (DTCO). *P*-wave velocity generally increases with depth (Fig. F35). In each logging unit (I, II, and III), the increase in velocity with depth is approximately a linear relationship. The gradients of velocity with depth are 0.76, 0.98, and 1.39 m/s per meter, respectively, for logging Units I, II and III, indicating that velocity increase accelerates with depth.

The formation velocity starts to be identified below 175 m LSF (see "Data and log quality"). Above this depth, velocities are likely to be those of the drilling fluid. Such a transition causes a jump in V_P at this depth and is almost certainly an artifact. The boundary zone between logging Units I and II is characterized by relatively low velocities (1600–1670 m/s) compared to those in formations immediately above and below (1650–1750 m/s). However, the absolute values of velocity in the boundary zone may not represent those of the formation because no clear distinction between formation and mud arrival could be made (see "Data and log quality").

P-wave velocity in logging Unit II is characterized by a monotonic increase in values with minor fluctuations (with a cycle of ~25 m). This is somewhat in contrast with resistivity logs, which have no clear increasing or decreasing trend with depth.

Sonic velocity in logging Unit III is characterized by a general increase in value with depth, with several major low-velocity zones where velocities decrease with depth (529–600, 660–695, 773–827, 884–894, and 915–965 m LSF) (Fig. F35). Below each decreasing velocity region, the velocities increase again to the main trend line. The shallowest low-velocity zone corresponds to the disrupted zone identified in the resistivity images and could be attributed to poor hole conditions. From ~722 to ~901 m LSF the sonic log shows a mixture of high- and low-frequency components. At the Subunit IIIB/IIIC boundary (905 m LSF), there is a significant increase in velocity (to a

value >2600 m/s), followed by the deepest of the decreasing velocity zones.

Comparison of *P*-wave velocity with other properties

Figure F38 shows cross-plots between *P*-wave velocity and other properties such as resistivity (bit) and resistivity-derived porosity. Porosities used here are those estimated from the bit resistivity log. Both the velocity versus resistivity and the velocity versus resistivity-derived porosity cross-plots show generally good correlations. In the velocity versus resistivity plot, low resistivity data corresponding to logging Unit II and logging Unit I (corresponding to the deeper parts of the unit) appear to overlap (some Unit I data are hidden beneath Unit II data), mainly because resistivity is not well resolved between the two units, whereas velocity is better resolved. However, in the velocity versus resistivity-derived porosity plot there seems to be a good match between these porosities.

Structural geology and geomechanics

Structural interpretations are based on resistivity image data (see the "Expedition 314 methods" chapter). Our interpretations were primarily drawn from the shallow level of investigation, with a 34 cm estimated diameter of investigation, in Hole C0001D. The small variability of the images between shallow, medium, and deep levels of investigation with the resistivity imaging tool indicates good quality data, even in a section between 529 and 629 m LSF where drilling problems were encountered.

Identification of bedding planes needed special care and was achieved by comparing images and logging data at this site. The process of dynamic normalization sometimes creates artifacts that have features similar to bedding planes. In order to reduce such misinterpretation, we compared several different dynamic and static normalization images with bit resistivity, ring resistivity, and gamma ray logs.

Bedding

Bedding dips are mostly gentle (<10°) throughout the upper 400 m LSF of the hole with the exception of higher values within logging Subunit IB (190.5–198.9 m LSF) and immediately beneath it (Figs. F39, F40, F41). Below 400 m LSF, bedding dips gradually become steeper (averaging ~10°–20° at the base of the hole) and include values up to 60°. Bedding dips are more difficult to discern in the deeper parts of the hole (below 200 m LSF and particularly between

800 and 880 m LSF); here the higher and more uniform resistivity values and/or lack of coherent bedding planes do not provide the necessary image contrast to easily interpret bedding. Interpretation of the logging Unit I/II boundary is discussed in "Conclusions."

Natural fractures

Natural fractures can be divided into the three following classes (Fig. F40):

1. Steep conductive fractures (~75°–90°) trending northwest–southeast and most commonly occurring from ~640 m LSF to the base of the hole,

2. Shallower dipping conductive and resistive fractures (~30°–75°) trending northwest–southeast and occurring throughout the hole (including below 640 m LSF), and

3. Conductive and resistive fractures of variable trend but predominantly northeast–southwest that are distributed throughout the hole.

These three fracture classes are distinct from drilling-induced tensile fractures which are described separately.

The shallower dipping fractures (Classes 2 and 3) generally can be fitted well with a single sinusoid, although some fractures are less distinct and consequently result in uncertainties in dip and azimuth. The conductivity of these fractures is often difficult to determine, particularly where fractures interact with conductive borehole breakouts or tensile fractures. The fracture aperture was too small to measure in almost all cases. This narrow aperture makes these fractures more difficult to recognize than the steeper conductive fractures that occur in the bottom half of the borehole.

The steep conductive fractures (Class 1) commonly have apertures of 50–60 mm, as measured in the images (Fig. F42). The fractures are steep and can extend along the length of the borehole for ~10–20 m. The fractures are undulating and typically have been compositely approximated by several sinusoids along their entire length. Although steep conductive fractures occur from 640 m LSF to the base of the hole, they are most intensely developed from 785 to 875 m LSF, which correlates with a zone of decreased resistivity and higher resistivity-derived porosity (see "Physical properties"). Because the steep fractures are locally offset by shallower dipping, less conductive fractures (Classes 2 and 3), we believe the former are natural fractures, formed before the borehole was drilled, and predate the more shallowly dipping fractures. In a few cases, offset of the steep conductive fractures can be determined (Fig. F42) and show normal fault offset.

Disrupted zone

At ~529 m LSF, breakouts stop and shallowly dipping bands of resistivity (interpreted as bedding) become partially to completely disrupted. For example, at 550–551 m LSF, circular bodies of high-resistivity material are separated horizontally and locally enveloped by high-conductivity material. At 584 m LSF high-conductivity material appears to intrude upward into the overlying high-resistivity layer (Fig. **F43**).

Borehole breakouts and drilling-induced tensile fractures

Breakouts comprise a strikingly obvious feature in the upper half of the borehole (Figs. **F39**, **F44**). To 110 m LSF the breakouts are associated with fractures that are perpendicular to them (Fig. **F44**). We interpret these fractures as drilling-induced tensile fractures (DITFs). The breakouts are obvious to 530 m LSF and patchy in the lower half of the hole, but the associated DITFs are generally less apparent. In general, the DITFs are more common in the lower 400 m of the hole, whereas breakouts are more common in the upper 530 m of the hole. An exception is the upper 70–100 m LSF, where strong breakouts and DITFs coexist. The azimuths of all breakouts and DITFs are nearly exactly perpendicular (Fig. **F45**).

The variable occurrence and character of breakouts suggest distinct zones and boundaries. We interpret the abrupt change in breakout occurrence at ~530 m LSF (see **"Disrupted zone"**) as resulting from an increase in borehole pressure during drilling rather than physical properties of the sediments (see **"Analysis of breakouts and drilling-induced tensile fractures"**). This is in contrast to the occurrence of breakouts at Site 808 (McNeill et al., 2004; Ienaga et al., 2006), which showed a relationship with lithology. Within the 70–530 m LSF zone of strong breakouts, their character (conductivity, width, and homogeneity) allows division into three zones: ~70–200, 200–300, and 300–530 m LSF (Fig. **F39**). Transitions between these zones coincide with log character change and mark logging unit boundaries at Subunits IB/IIA and IIA/IIB, respectively. On a meter scale, no clear correlation is observed between changing sediment properties from logs and breakout character. See **"Log characterization and lithologic interpretation"** for further details. No major change in breakout character is observed with depth of investigation (shallow or medium versus deep) except for increased conductivity of the widest breakouts in the shallow image. No significant or consistent relationship between breakout width and hole depth is observed.

Analysis of breakouts and drilling-induced tensile fractures

Breakouts form perpendicular to the orientation of maximum horizontal principal stress (S_{Hmax}) and parallel to the minimum principal horizontal stress (S_{hmin}) (Zoback et al., 2003). Accordingly, in Hole C0001D S_{Hmax} is oriented 336° or north-northwest (Fig. **F44**). Because the breakouts and DITFs are oriented parallel to the borehole, which is vertical, one of the principal stresses is also vertical.

The occurrence of DITFs provides constraints on the magnitudes of stresses at this site. Figure **F45** shows stress polygons at four different depths in Hole C0001D (80, 720, 820, and 910 m LSF) where we observed clear tensile fractures (Fig. **F44**) (see the **"Expedition 314 methods"** chapter for details on determination of stress polygons). The red line in each plot is the trace of S_{Hmax} and S_{hmin}, along which the hoop stress becomes zero. This calculation assumes hydrostatic pore pressure and uses the APWD to constrain the borehole pressure (see Zoback et al., 2003, for details of calculation). The occurrence of DITFs indicates that the state of stress should lie somewhere above the red line.

Although the actual coefficient of friction value is not available for these weak sediments, Figure **F46** implies that it should be at least 0.6 or higher in order to allow a possible stress range that can induce tensile hoop stresses at the borehole wall. If the coefficient of friction was <0.6, the stress polygon would shrink and lie under the red line and the prism would be in an impossible state of stress (assuming that the breakouts conform to the Mohr-Coulomb failure model). Since weak sediments tend to have low resistance to shear stress, we assume a frictional coefficient of 0.6 for faults in this site.

At 80 m LSF, almost all possible magnitudes of S_{Hmax} and S_{hmin} are within the strike-slip fault stress regime ($S_{Hmax} > S_v > S_{hmin}$) and lie close to the state of frictional equilibrium; that is, the upper left boundary of the stress polygon (Fig. **F46A**). At 720, 820, and 910 m LSF, the possible state of stress should lie in any region above the red lines, in which case the faulting stress regime could be any type. At other depths, where no tensile fractures were observed, the magnitudes of S_{Hmax} and S_{hmin} should be below the tensile stress criterion (red line). This means that the state of stress should lie close to the red lines in Figure **F45** unless there are drastic changes in stress field with depth.

During drilling, the borehole pressure gradient (indicated by equivalent circulating density calculated from annulus pressure) was kept nearly constant at

hydrostatic state from the seafloor to ~500 m LSF, and thereafter it was elevated significantly over the hydrostatic pressure. This probably suppressed breakouts in the lower part of the hole.

Conclusions

Logging Unit I/II boundary: an unconformity

The seismic reflector corresponding to the logging Unit I/II boundary at 198.9 m LSF had previously been inferred to be either a fault or unconformity. The image data do not show significant disruption of bedding here except for within logging Subunit IB. Subunit IB shows a systematic increase in bedding dip from 16° to 46° at 191–192 m LSF then a gradual decrease to 22° at its base (Fig. F41). The dip of beds within logging Unit II is generally gentle (<7°), except for the uppermost beds that show steeper dips (14°–17°). The moderately dipping beds of Subunit IB could be explained by oblique stratification of sediments or slumping along a stratigraphic contact rather than tectonic fracturing or faulting.

Disrupted zone: fault or mass transport deposit?

The block in matrix and possible layer injection textures of the disrupted layer (Fig. F43) are similar to stratal disruption observed in mass transport deposits or in tectonically disrupted units from exhumed accretionary prisms (Cowan, 1985). Accordingly, we interpret the interval between 529 and 629 m LSF as a mass transport deposit or fault zone. The combination of environment, thickness of the zone, physical properties (including increased porosity), and comparison with seismic reflection data suggest to us that this is a fault zone. The resistivity-derived porosity decreases below the 529–629 m LSF interval (see "Physical properties"). Therefore, the most likely fault type would be normal, moving less consolidated material down to overlie more consolidated material. However, this assumes faulting of an undisrupted stratigraphy with porosity decreasing gradually with depth as a result of compaction. In an accretionary prism with a long history of deformation, this pattern may not occur, thus preventing determination of fault type; therefore, thrust faulting may also be a likely scenario.

Breakouts and drilling-induced tensile fractures: north-northwest shortening and east-northeast extension and predictions of fault types

The breakouts unequivocally show S_{Hmax} shortening at ~335° and extension at ~065° (Fig. F44). This indicates that the accretionary prism at Site C0001 is shortening perpendicular to the trend of the plate boundary and major prism structures and not parallel to the Global Positioning System (GPS)-constrained displacement of the Kii Peninsula to the northwest nor the plate tectonic convergence direction of the Philippine Sea plate and southwest Japan (300°–315°) (Miyazaki and Heki, 2001; Heki, 2007; Seno et al., 1993). Thus, the difference between the shortening direction of the prism at Site C0001 and the plate convergence direction must be accounted for elsewhere in either convergence oblique to the trend of the prism and/or in strike-slip faulting.

Log-seismic correlation
Overall logging unit correlation

Logging Unit I corresponds to the hemipelagic sediments between the seafloor and ~200 m seismic depth below seafloor (SSF) (Fig. F29). Logging Subunit IB corresponds to a thin low-amplitude reflection overlying the strong positive reflection at 200 m SSF that defines the base of logging Unit I. Logging Unit II corresponds to a zone of southeast-dipping, generally low amplitude reflections across these boundaries. Reflections intersect the borehole at the logging Subunit IIA/IIB and IIB/IIC boundaries, but there is no change in the general character of the reflections. The boundary between logging Units II and III correlates with a change in reflectivity from low amplitude above the boundary to high amplitude below the boundary. Logging Subunit IIIA corresponds to a series of high-amplitude, laterally continuous reflections that appear on the southeast side of the borehole that are cut off by the inferred fault that intersects the borehole at the base of this subunit.

Check shot survey data

Check shot data at Site C0001 were acquired at 16 depths in Holes C0001C (1 depth) and C0001D (15 depths) (Fig. F47; Table T8). These data sample depths from the seafloor to 635 m LSF. Attempts to acquire data at six stations deeper in Hole C0001D were unsuccessful because the battery in the seismicVISION tool failed. Between 3 and 20 (typically 10) air gun array shots were fired at each station. Noisy traces and traces with poor first arrival waveforms were deleted. The remaining traces were filtered (trapezoidal, minimum phase, and 30-40-150-200 Hz band-pass) and stacked to produce the traces shown in Figure F47. The first arrival wavelet is unambiguous on all traces, although noise makes identifying the true first break difficult on a few of the traces.

The first arrival times were picked manually as illustrated in Figure F47. These are the "raw first arrival" times in Table T8. We applied a damped least-squares inversion to the observed depth-time data (Lizarralde and Swift, 1999). This inversion determines a smooth velocity versus depth curve by varying the arrival times by amounts that are within their uncertainty. We estimated the uncertainty of the arrivals to be ~0.2 ms. We used a damping coefficient of 0.05 because it produced a chi squared (χ^2) value consistent with the optimal balance between over- and underfitting the data. The smoothed interval velocities and adjusted arrival times are shown in Table T8. The improvement in estimated interval velocities, indicated by the smoothness of the curve and the general downward increase of velocity (Fig. F48), is dramatic. The accompanying changes in arrival times are very small. We used the smoothed arrival picks and the tool depths as the check shot curve, which we then used for synthetic seismogram preparation.

The smoothed interval velocity curve and sonic P-wave velocity data are generally similar (Fig. F49). The largest mismatch is from 0 to 175 m LSF, where the check shot curve is ~60–80 m/s faster than the sonic log. In this interval, the processed sonic log data did not show an arrival that could be reliably separated from the mud arrival (see "Data and log quality"). Therefore, we interpret that the check shot velocity is a better representation of the long wavelength velocity depth function in this depth range. Both the check shot and sonic log velocities show a general leveling of velocity at ~500 m LSF then a resumption of the downward increasing trend below ~550 m LSF.

We were not able to construct a meaningful vertical seismic profile (VSP) using these data. We tried a number of filtering and gain combinations but could not identify coherent upward traveling reflections. We attribute this to noise from the vibration of the drill pipe in the current and other sources of downhole noise.

Density log data

Density data, along with P-wave velocity data, are necessary to calculate a synthetic reflection seismogram. At Site C0001, density data were logged using the adnVISION tool; however, the tool was damaged during the operation and we could not retrieve any data from its memory until the final days of the expedition, too late to be used for this analysis. During the LWD operation, a subset of the data was sent to the surface by mud pulse from the bottom in real time (see the "Expedition 314 Methods" chapter). Figure F50A shows these real-time bulk density data

(RHOB), which were obtained in Hole C0001D from the seafloor to ~500 m LSF. However, the data in the 15–45 m LSF interval are noisy. To improve the log for use in synthetic seismogram generation, we spliced in the real-time density data from Hole C0001C from above the seafloor to 49 m LSF and assumed a constant density to the sea surface (Fig. F50B). The density curve of Hole C0001C was shifted up by ~1 m to correlate with that of Hole C0001D at the seafloor.

The merged Hole C0001C/C0001D real-time density log is well behaved to just above a 200 m LSF zone of interest that correlates with a strong positive impedance reflector on the 3-D seismic data. The density log, however, varies strongly, with obviously incorrect (as low as 1.1 g/cm³) density values at this boundary. During synthetic seismogram generation, these variations produce a series of emergent reflections just below the boundary. The real-time density log below the 200 m LSF boundary continues to be noisy; based on the real-time ultrasonic caliper data the real-time densities below this boundary may be suspect (see "Data and log quality").

To produce a more realistic density log that does not produce spurious reflections on the synthetic seismogram at the 200 m boundary and below, we created a pseudodensity log derived from the thermally corrected ring resistivity–derived porosity log (see "Physical properties"). To obtain a formation matrix density, the real-time density-derived porosity data were cross-plotted against the ring resistivity porosity data; where the values were approximately equal to each other, it was assumed that the values were real. The corresponding logging density values were then used to derive a matrix density of 2.64 g/cm³, and the fluid density was assumed to be that of seawater (1.03 g/cm³). The matrix and fluid density values along with the resistivity-derived porosity were then used to derive the pseudodensity curve, based on the following equation:

$$\rho_b = \rho_{ma}(1 - \phi) + \rho_f\phi,$$

where ρ_b is the pseudodensity, ρ_{ma} is the matrix density, ρ_f is the fluid density, and ϕ is porosity. The resulting pseudodensity log is a smoother curve than the real-time density log (Fig. F50C).

We merged the spliced real-time density curve (Fig. F50B) and this pseudodensity curve (Fig. F50C) into a preferred density curve designed to produce the fewest spurious reflections in the resulting synthetic seismogram. To create the composite density curve, we used the spliced real-time data from the sea surface to just above the unrealistically low density values in the 200 m LSF zone and pseudodensity data

for the 200 m zone and from this zone to the bottom of the hole (Fig. **F50D**).

Sonic log data

The sonicVISION tool is designed for use in higher velocity materials than those commonly encountered while drilling slope and accreted sediments. The Schlumberger DCS representative processed the raw sonic waveforms on board using a range of filters and interpreted the formation slowness based on a mixture of mixed process (MP) wide and leaky-P mode processed waveforms (see the **"Expedition 314 methods"** chapter). The resulting slowness values are most reliable in the areas of low noise and where the velocities are distinct from the borehole mud velocities, which are in this case close to that of water. For example, in Hole C0001D the slowness values above ~175 m LSF (Fig. **F49**) are suspect, as are the values in zones with poor hole conditions or low signal-to-noise ratio. The quality of these logs was qualitatively determined by examining the waveforms and coherency plots, referencing the method of processing used for the picking, and assessing whether the data are either noisy or close to the mud arrival. Areas where hole conditions were poor and/or drilling operations may have affected the quality of the derived slowness values are detailed in **"Data and log quality."**

The picked sonic values produced a sonic log that was then calibrated using the check shot data for the site. For Hole C0001D, the seismicVISION tool stopped working after an observation at 635.2 m LSF and acquired no data deeper in the hole. We base the time-depth relationship below the deepest check shot values by assuming a linear drift curve from ~635 m LSF to total depth (Fig. **F51A**). The explanation of the use of drift curves to calibrate sonic logs is available in the **"Expedition 314 methods"** chapter. The calibrated sonic log differs most significantly from the picked sonic log in the shallow areas (shallower than ~175 m LSF) in which the calibrated curve has significantly higher velocities.

Synthetic seismogram

Using the favored density log (Fig. **F51C**), created by splicing the real-time density from Holes C0001C and C0001D, the pseudodensity curve, and the calibrated sonic log (Fig. **F51B**), corrected using the long-wavelength component of the time-depth relationship determined by check shots (Fig. **F51A**), we generated a synthetic seismogram (Fig. **F51D**). The synthetic seismogram in general agrees well with the reflectivity of the 20 cross-line traces on Inline 2480 in the vicinity of the borehole (Fig. **F51G**) for the regions from seafloor to ~192 m LSF. However, the 8 m

zone of low densities and slightly lower velocities just above 200 m LSF produces a negative polarity reflection in the synthetic seismogram that does not agree with the seismic data that instead exhibit a strong positive polarity reflection with evidence of composite tuned reflection character at its base. Additionally, from 200 to ~528 m LSF, the synthetic seismogram exhibits a series of reflections not present in the seismic data that are largely transparent over this interval. The ~25 m cycles observed in the sonic log over this region may be the cause of this anomalous reflectivity (see **"Structural geology and geomechanics"** for discussion of the sonic log). In the synthetic seismogram, a series of strong reflections exist within the low-velocity zone from ~523 to 640 m LSF before transitioning to occasional reflectivity below this zone. There is a general increase in reflectivity in the seismic data around the depths of the low-velocity zone and through the bottom of the hole. One additional anomalous reflection is present in the synthetic seismogram at ~901 m LSF that is generated by the change to higher velocities in the deepest parts of the hole; however, this change may be a function of increased signal-to-noise ratio rather than a true change in velocity, as evidenced by the lack of such a strong reflection at that depth on the seismic data.

Strong reflector at 200 m LSF

A prominent reflector is observed in the 3-D prestack time-migrated seismic volume (Moore et al., 2007) at a depth of ~3.2 s two-way traveltime around Site C0001, which separates the package of reflective slope sediments from an underlying seismically transparent unit (Fig. **F46**). This reflector approximately correlates with the boundary between logging Units I and II at ~200 m LSF. The reflector is traceable in the cross-lines of the 3-D seismic volume across the entire ~12 km width of the volume (Fig. **F52**). This reflector exhibits a strong positive polarity waveform (Fig. **F53**), similar to that expressed at the seafloor, which requires an increase in acoustic impedance (velocity × density) with depth.

The synthetic seismogram computed using the calibrated sonic log and the best available density log (Fig. **F51**) shows a negative polarity reflection at the ~200 m LSF boundary (Fig. **F54A**), which does not match the observed reflector in the 3-D seismic data. To test the sensitivity of this reflector to the specific densities within the 8 m zone above the ~200 m LSF boundary, we created a series of models based on the pseudodensity curve with density lows to 1.4 g/cm³ at the 200 m LSF boundary in an attempt to match both the low resistivity and low density values recorded in that zone (Fig. **F54B–F54D**). All of these

tests produce a negative polarity reflection. Even removing the 8 m zone entirely produces a small negative polarity reflection simply because of the density decrease (by 0.13 g/cm^3) at the logging Unit I/II boundary (Fig. **F54E**). With the strong possibility that the 8 m zone had poor hole conditions (see description of the real-time caliper in **"Data and log quality"**) and the observation of a velocity and density increase just above this zone, we ran an additional test where the 8 m zone is instead a density high (Fig. **F54F**). This model more appropriately reproduces the strong positive reflector from the top of the zone but still produces an erroneously large second reflector off the base of the zone. Our final and best synthetic model at this site is one where the top of the 8 m interval is a density peak and the base of the interval returns to lower density values over ~16 m (Fig. **F54G**). Both this model and the previous model use a 2.1 g/cm^3 density value based on the hemipelagic muds of Site 808. Our final model results in a positive reflection at the top of the 8 m thick zone and a complicated response at the base of the 200 m LSF layer, consistent with the local seismic reflection character.

Discussion and synthesis

Site C0001 sampled deep into the thrust sheet of what has previously been interpreted as a shallow branch of the megasplay fault in the Kumano transect region (Moore et al., 2007). A 976 m interval was drilled and logged, made up of apparently strongly deformed mudstones with some silty to sandy sediments. Prior to drilling and based on seismic interpretation, this interval was hypothesized to represent relatively old and well-lithified mudstone of the interior of the Nankai accretionary prism overlain by ~200 m of hemipelagic slope deposits. Log and vertical seismic data largely support this overall model and provide the first in situ information on physical properties, lithology, structure, and state of stress in this key element of the Nankai subduction system. Cores collected during subsequent Expedition 315 tested these interpretations of log data and provided age and textural information not available from the logs.

Importantly, the riserless drilling at Site C0001 fulfilled a key project goal of piloting the planned deep-riser drilling at this location. For the riser hole planned in NanTroSEIZE Stage 2, it was imperative that we obtain information on the rock properties and potential qualities for drilling and casing of the uppermost kilometer as preparation for installation of riser casing. Drilling parameters and physical property logging have accomplished this goal, and the well planning for the riser operation will proceed with this knowledge. In particular, establishing the uppermost few hundred meters of a riser borehole actually requires riserless drilling, because the near-surface sediments are generally not strong enough to withstand the hydrostatic pressure in a riser column of weighted mud extending to the sea surface more than 2000 m above the seabed. Hence, the strength and in situ pore pressure in the sediments are key parameters in determining how deep the drilling must proceed in open hole before casing can be set, the blowout preventer connected, and the riser set up for mud-based drilling.

Make-up of the thrust sheet

As described in the sections of this chapter, we found that the interior of the thrust sheet is remarkably homogeneous in apparent composition, with gamma ray and resistivity values indicating that mudstones dominate. In addition, the high seismic/sonic velocity (reaching >2700 m/s at 1000 m LSF) and relatively low apparent porosity suggest that the rocks in the lower part of the drilled section are overconsolidated relative to their present depth below the surface and have therefore been uplifted with erosion of a significant overlying section or alternatively have been diagenetically altered by cementation at their present depth. The available information favors the former interpretation.

The "disrupted zone" extending from 529 to 629 m LSF may be a zone of major tectonic deformation, as described in the **"Log-seismic correlation"** and **"Structural geology and geomechanics"** sections of this chapter. This disrupted zone corresponds exactly to the discontinuous patch of anomalously bright, moderately seaward-dipping reflectivity in the seismic profiles (see Fig. **F2**). If so, it is possible that it represents a zone of dilated fractures. The seismic imaging suggests that the zone is underlain by a steeply dipping fault (Figs. **F3, F46**) with shallowly dipping bedding abutting the fault, consistent with interpretation of the zone as one of the following:

1. A thrust fault that has been rotated to a steep dip by subsequent thrusting on a deeper structure;
2. A normal fault on the backlimb of a deeper thrust structure, accommodating the hanging wall folding; or
3. A thrust reactivated as a normal fault.

The interpretation will require analyses of core samples, such as age determination, to assess which is most likely.

State of stress and pore pressure

The borehole breakout and drilling-induced tensile fracture information presented in this chapter place bounds on the orientation and permissible magnitude of the ambient principal stresses at this location. Two different zones of breakouts are divided by the disrupted zone (~529–629 m LSF), with strong breakouts but few DITFs above, and less-prominent breakouts but well-developed DITFs below. The orientation of S_{Hmax} at ~335° azimuth is perpendicular to the trend of the major prism structures and significantly oblique to the far-field plate tectonic relative motion vector of 300°–315° (Miyazaki and Heki, 2001; Seno et al., 1993; Heki, 2007). This implies significant partitioning between convergent and strike-slip motion within the outer accretionary prism, consistent with the apparent stress state favoring strike-slip faulting implied by analysis of the tensile fractures and breakouts. To produce tighter constraints on stress magnitude will require information on sediment strength and on ambient pore fluid pressure. The former can be provided by core studies; the latter is more difficult based on the available data. While installing casing during later expeditions, it may be possible to perform leak-off tests that will provide information on S_{hmin} and ambient pore pressure.

No direct pore fluid pressure information was obtained during Expedition 314; however, the MWD-APWD data provide information on borehole annular pressure in the circulating fluid (seawater plus occasional mud pills) while drilling. Normally during drilling in open hole, this value should remain near the hydrostatic pressure except when heavy mud is being pumped into the hole or when the formation is "packing off" around the drill string. Therefore, it typically shows transient higher pressures at intervals while drilling. However, in both Holes C0001A and C0001D, the APWD and related ECD measurements became elevated and remained elevated from the ~500 m LSF level to the bottom of the hole. This is in marked contrast to other sites drilled during this expedition and may only represent charging of formation fractures with drilling fluids during pumping and sweep operations. Alternatively, it may be a qualitative indicator of elevated in situ ambient pressure in the boreholes.

References

Cowan, D.S., 1985. Structural styles in Mesozoic and Cenozoic mélanges in the western Cordillera of North America. *Geol. Soc. Am. Bull.,* 96(4):451–462. **doi:10.1130/0016-7606(1985)96<451:SSIMAC>2.0.CO;2**

Heki, K., 2007. Secular, transient and seasonal crustal movements in Japan from a dense GPS array: implication for plate dynamics in convergent boundaries. *In* Dixon, T., and Moore, C. (Eds.), *The Seismogenic Zone of Subduction Thrust Faults:* New York (Columbia Univ. Press), 512–539.

Ienaga, M., McNeill, L.C., Mikada, H., Saito, S., Goldberg, D., and Moore, J.C., 2006. Borehole image analysis of the Nankai accretionary wedge, ODP Leg 196: structural and stress studies. *Tectonophysics,* 426(1–2):207–220. **doi:10.1016/j.tecto.2006.02.018**

Kinoshita, M., Goto, S., Hamamoto, H., and Yamano, M., 2003. Heat flow distribution and thermal regime across the Nankai accretionary complex. *Eos, Trans. Am. Geophys. Union,* 84(46)(Suppl.):T42C-06. (Abstract)

Lizarralde, D., and Swift, S., 1999. Smooth inversion of VSP traveltime data. *Geophysics,* 64(3):659–661. **doi:10.1190/1.1444574**

McNeill, L.C., Ienaga, M., Tobin, H., Saito, S., Goldberg, D., Moore, J.C., and Mikada, H., 2004. Deformation and in situ stress in the Nankai accretionary prism from resistivity-at-bit images, ODP Leg 196. *Geophys. Res. Lett.,* 31(2):L02602. **doi:10.1029/2003GL018799**

Mikada, H., Becker, K., Moore, J.C., Klaus, A., et al., 2002. *Proc. ODP, Init. Repts.,* 196: College Station, TX (Ocean Drilling Program). **doi:10.2973/odp.proc.ir.196.2002**

Miyazaki, S., and Heki, K., 2001. Crustal velocity field of southwest Japan: subduction and arc-arc collision. *J. Geophys. Res.,* 106(B3):4305–4326. **doi:10.1029/2000JB900312**

Moore, G.F., Bangs, N.L., Taira, A., Kuramoto, S., Pangborn, E., and Tobin, H.J., 2007. Three-dimensional splay fault geometry and implications for tsunami generation. *Science,* 318(5853):1128–1131. **doi:10.1126/science.1147195**

Seno, T., Stein, S., and Gripp, A.E., 1993. A model for the motion of the Philippine Sea plate consistent with NUVEL-1 and geological data. *J. Geophys. Res.,* 98(B10):17941–17948. **doi:10.1029/93JB00782**

Zoback, M.D., Barton, C.A., Brudy, M., Castillo, D.A., Finkbeiner, T., Grollimund, B.R., Moos, D.B., Peska, P., Ward, C.D., and Wiprut, D.J., 2003. Determination of stress orientation and magnitude in deep wells. *Int. J. Rock Mech. Min. Sci.,* 40(7–8):1049–1076. **doi:10.1016/j.ijrmms.2003.07.001**

Figure F1. Summary log diagram, Site C0001. LSF = LWD depth below seafloor. PEF = photoelectric factor. Black tadpoles = bedding, red tadpoles = fracture, tadpole line = dip direction of plane.
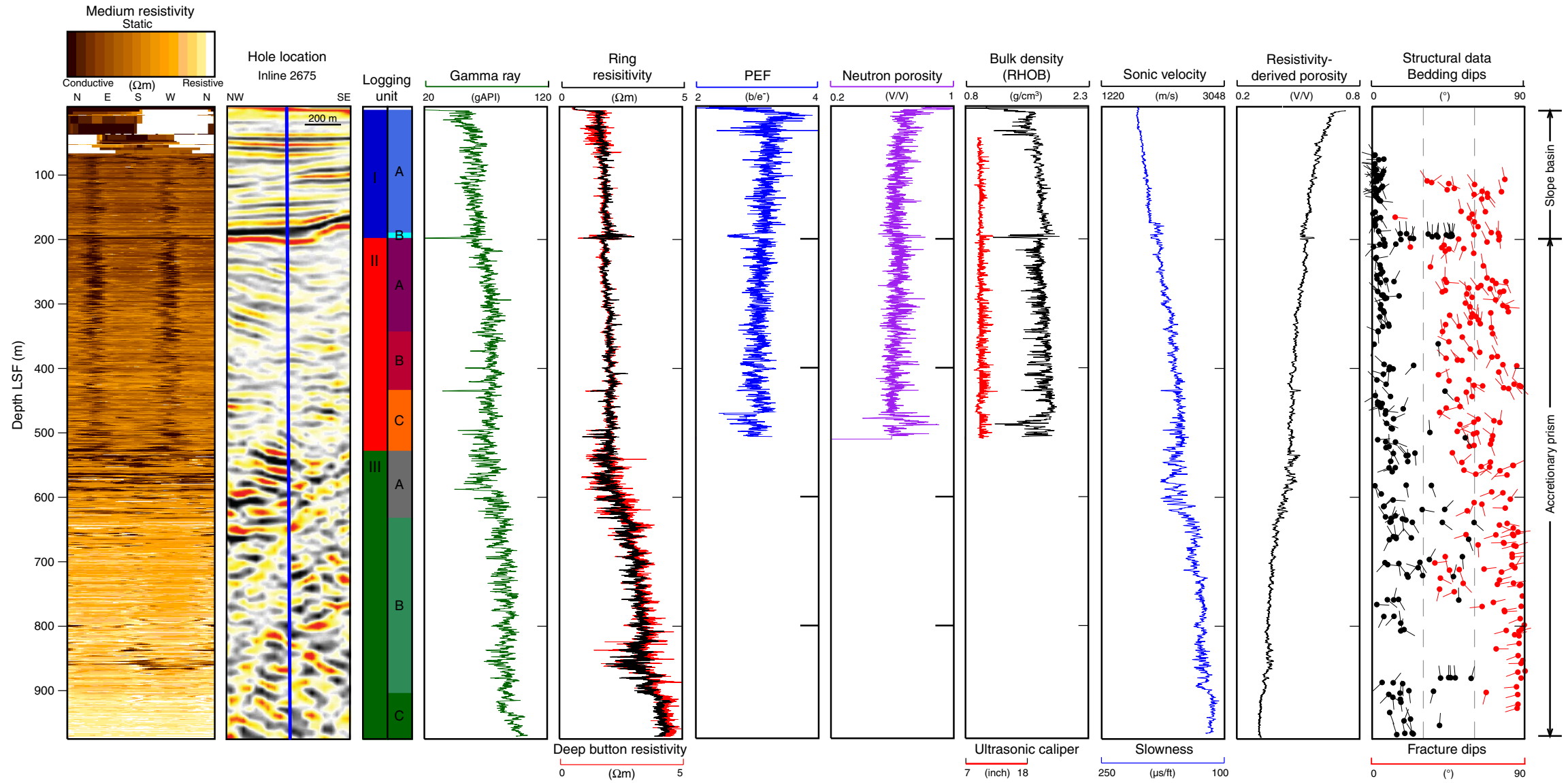
Figure F2. Three-dimensional seismic profile crossing Site C0001 (Moore et al., 2007). Profile location is plotted in Figure **F3.** **A.** Inline 2675. Site C0004 location is also shown. **B.** Cross-line 5475. VE = vertical exaggeration.
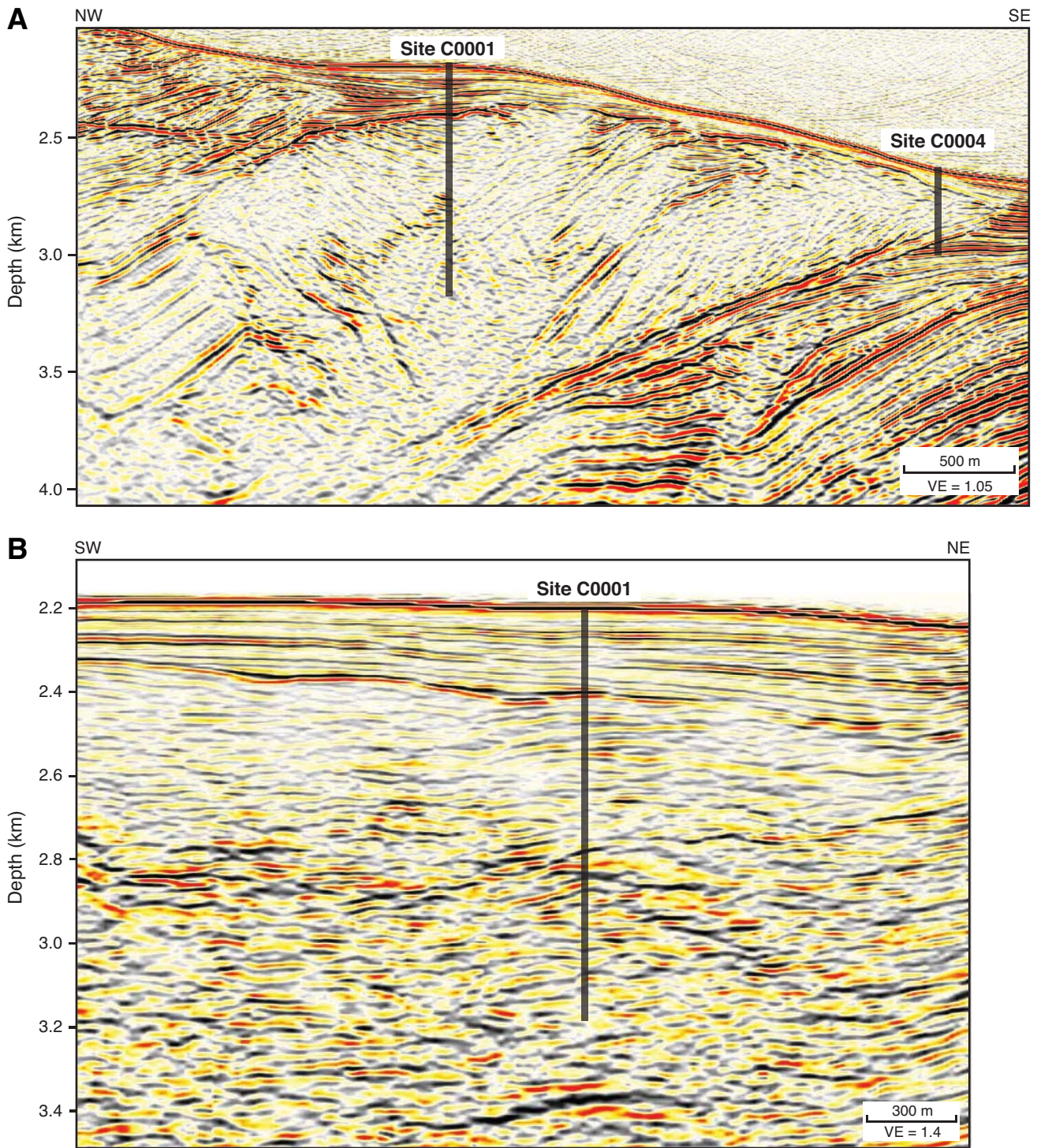
Figure F3. Locations of drill holes at Site C0001. Solid lines = seismic profile coverage.
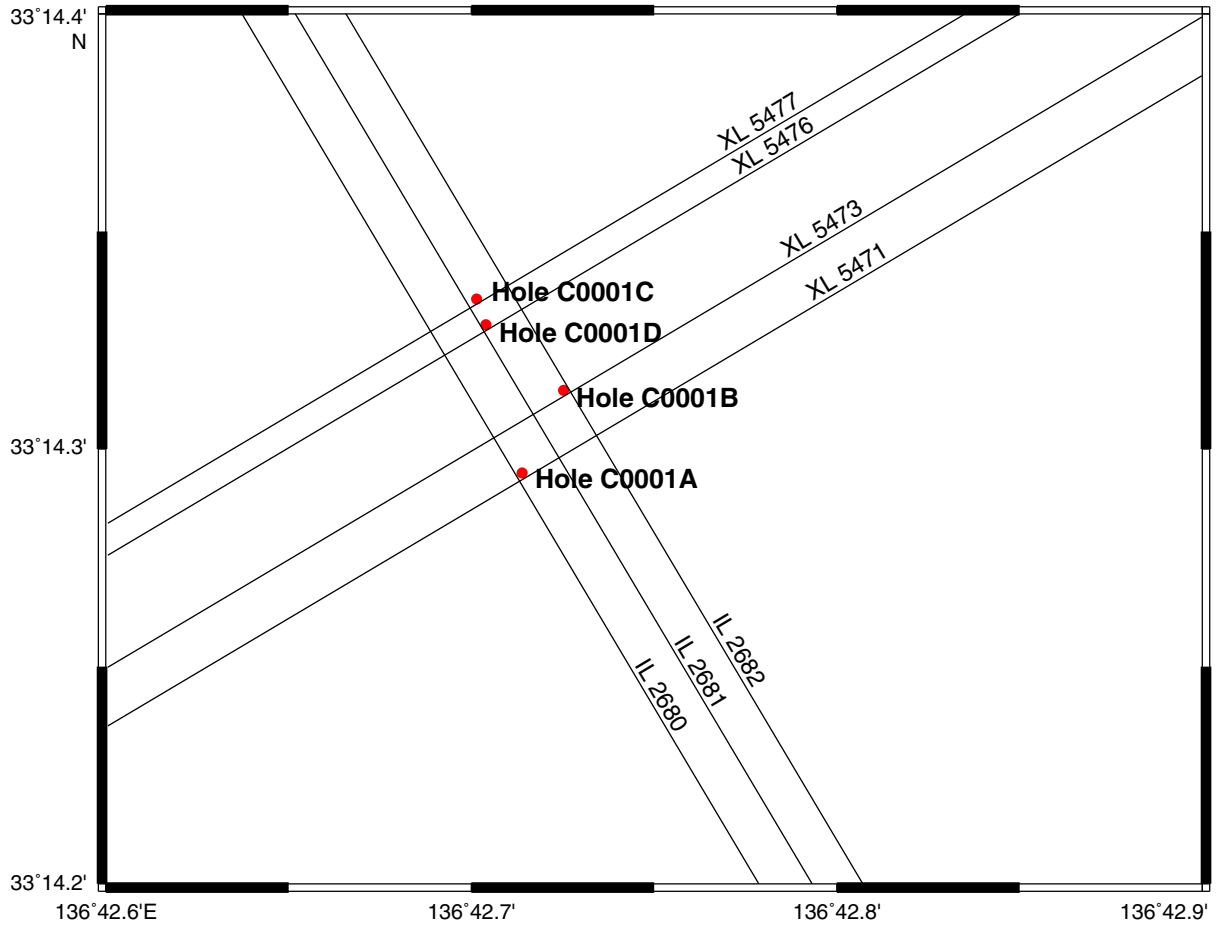
Figure F4. Drilling parameters and gamma ray log plotted vs. time for MWD-APWD operations in pilot Hole C0001A. GRM1 = gamma ray log from the MWD tool (real time), ECD = equivalent circulating density, APRS = average annular pressure, TRPM = MWD turbine rotation speed (off = <1500 or >4500 rpm, on = 1500–4500 rpm), TRPM_RT = TRPM (real time), CRPM = collar rotation, SWOB = surface weight on bit, HKLD = hook load, SPPA = standpipe pressure, ROP = rate of penetration, ROP_5ft = 5 ft averaged ROP, LSF = LWD depth below seafloor, DRF = drillers depth below rig floor.
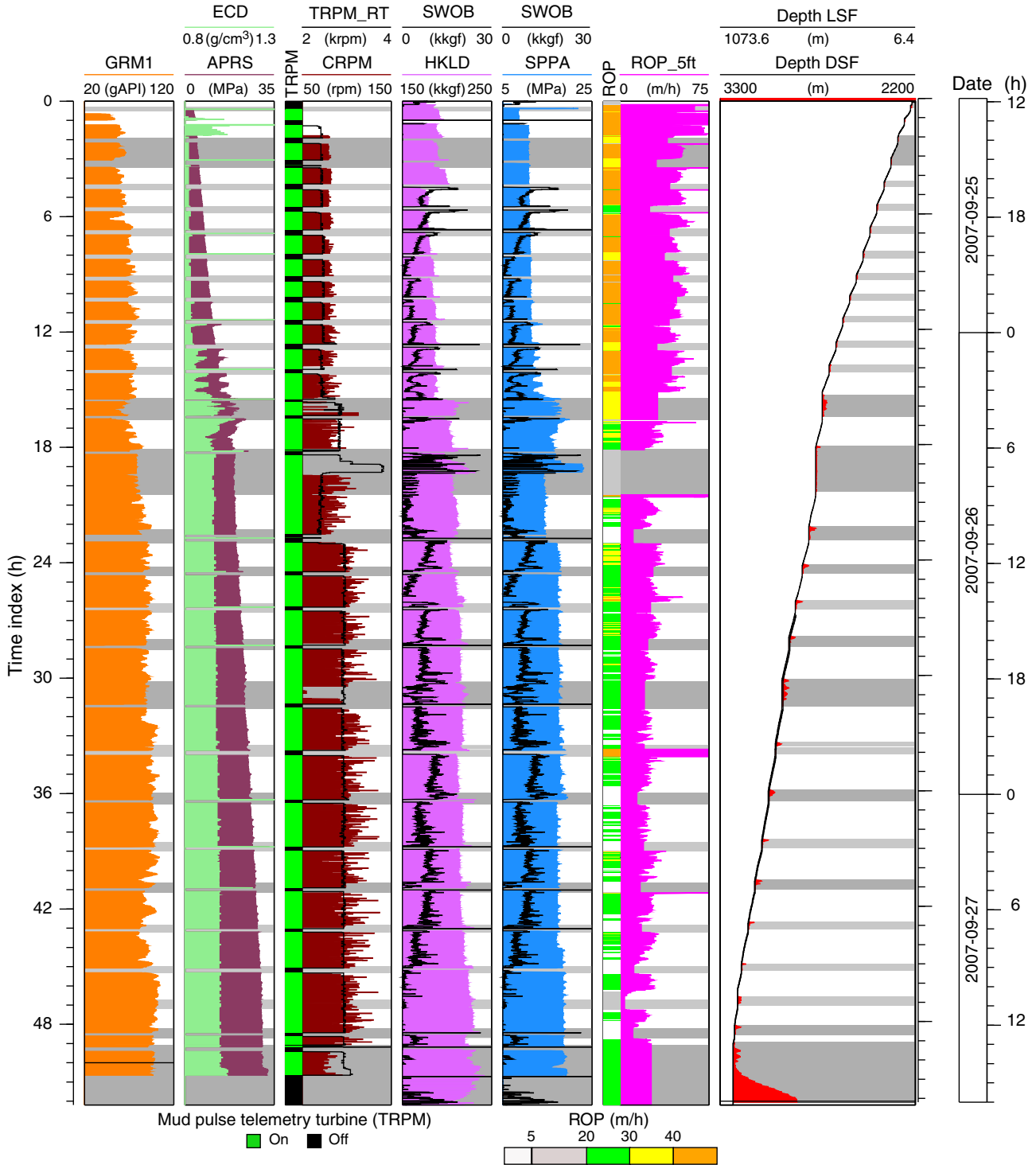
Figure F5. Drilling parameters and gamma ray log plotted vs. time for MWD-APWD operations in pilot Hole C0001C. GR_RAB_RT = gamma ray resistivity-at-the-bit rotation (real time), ECD = equivalent circulating density, APRS = average annular pressure, TRPM = MWD turbine rotation speed (off = <1500 or >4500 rpm, on = 1500–4500 rpm), TRPM_RT = TRPM (real time), CRPM = collar rotation, SWOB = surface weight on bit, HKLD= hook load, SPPA = standpipe pressure, ROP = rate of penetration, ROP_5ft = 5 ft averaged ROP, LSF = LWD depth below seafloor, DRF = drillers depth below rig floor.
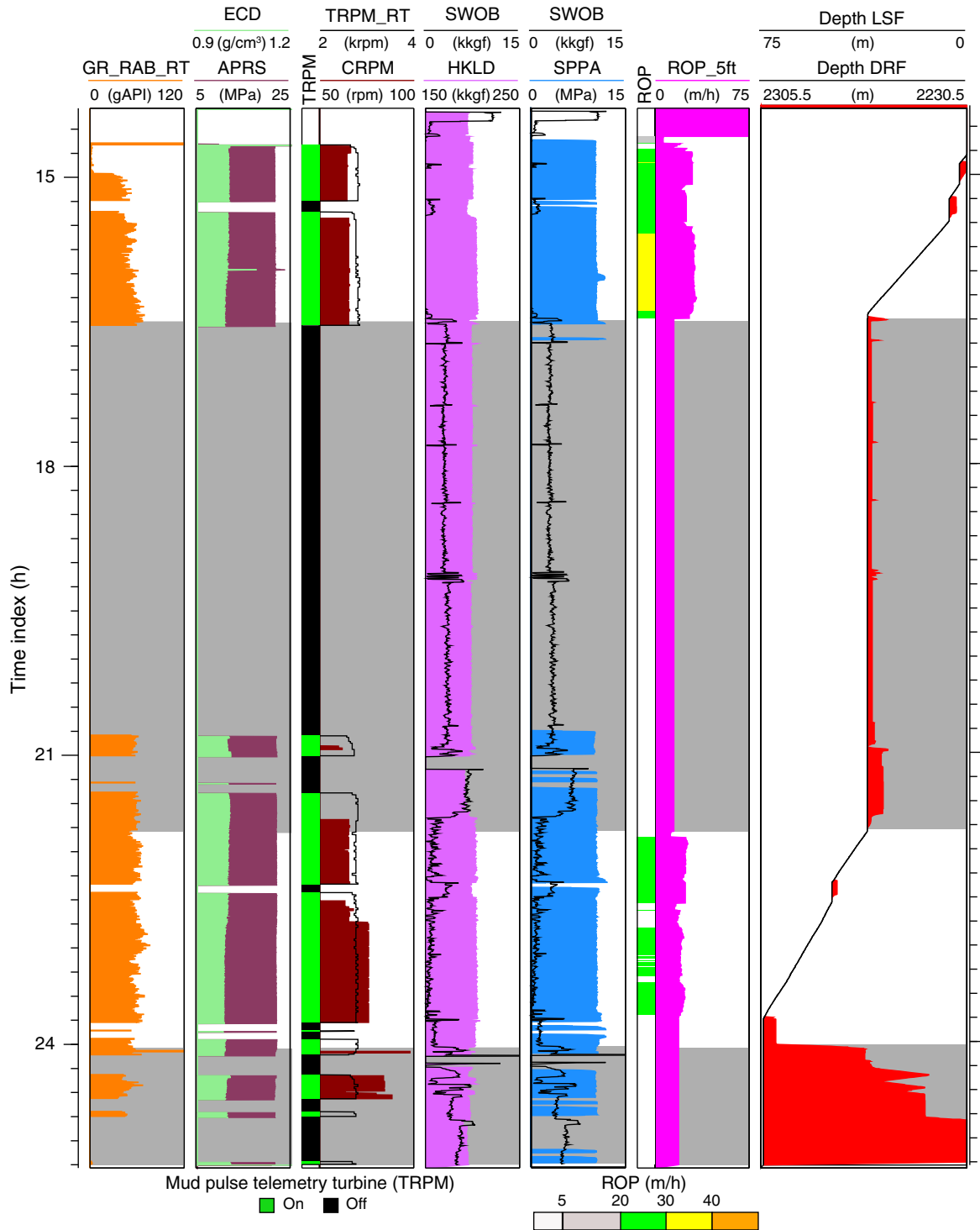
Figure F6. Drilling parameters and gamma ray log plotted vs. time for MWD-APWD operations in pilot Hole C0001D. GR_RAB_RT = gamma ray resistivity-at-the-bit rotation (real time), ECD = equivalent circulating density, APRS = average annular pressure, TRPM = MWD turbine rotation speed (off = <1500 or >4500 rpm, on = 1500–4500 rpm), TRPM_RT = TRPM (real time), CRPM = collar rotation, SWOB = surface weight on bit, HKLD = hook load, SPPA = standpipe pressure, ROP = rate of penetration, ROP_5ft = 5 ft averaged ROP, LSF = LWD depth below seafloor, DRF = drillers depth below rig floor.
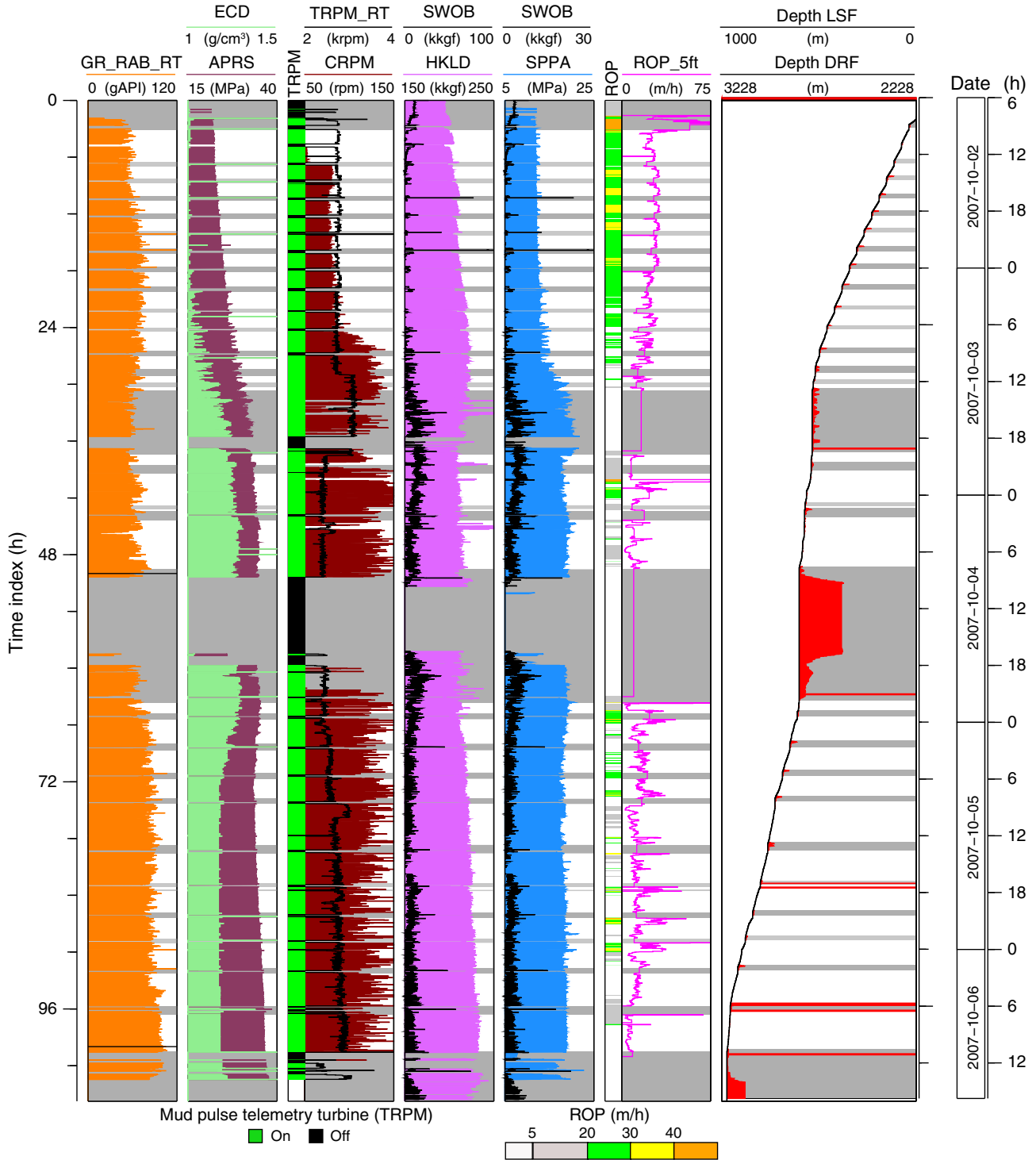
Figure F7. Mudline identification in Hole C0001A using real-time gamma ray log of the MWD tool. The mudline is identified by a break in the GRM1 log at 2226.4 m drillers depth below rig floor (DRF). LSF = LWD depth below seafloor.
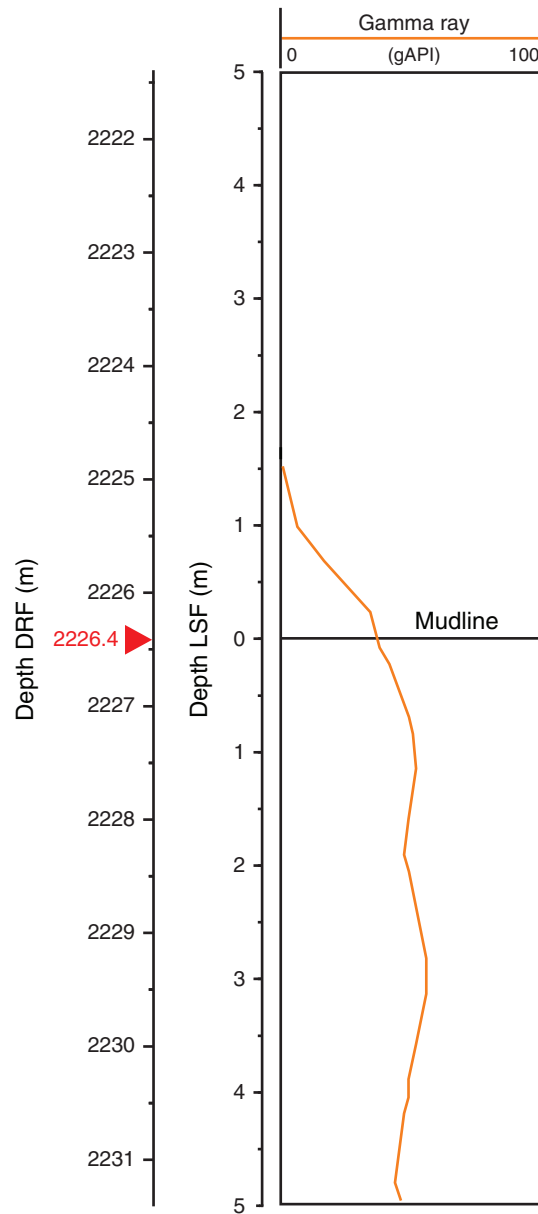
Figure F8. Control logs of Hole C0001A. LSF = LWD depth below seafloor, ROP = rate of penetration, SWOB = surface weight on bit, SPPA = standpipe pressure, ECD = equivalent circulating density, APRS = average annular pressure, GRM1 = gamma ray (MWD).
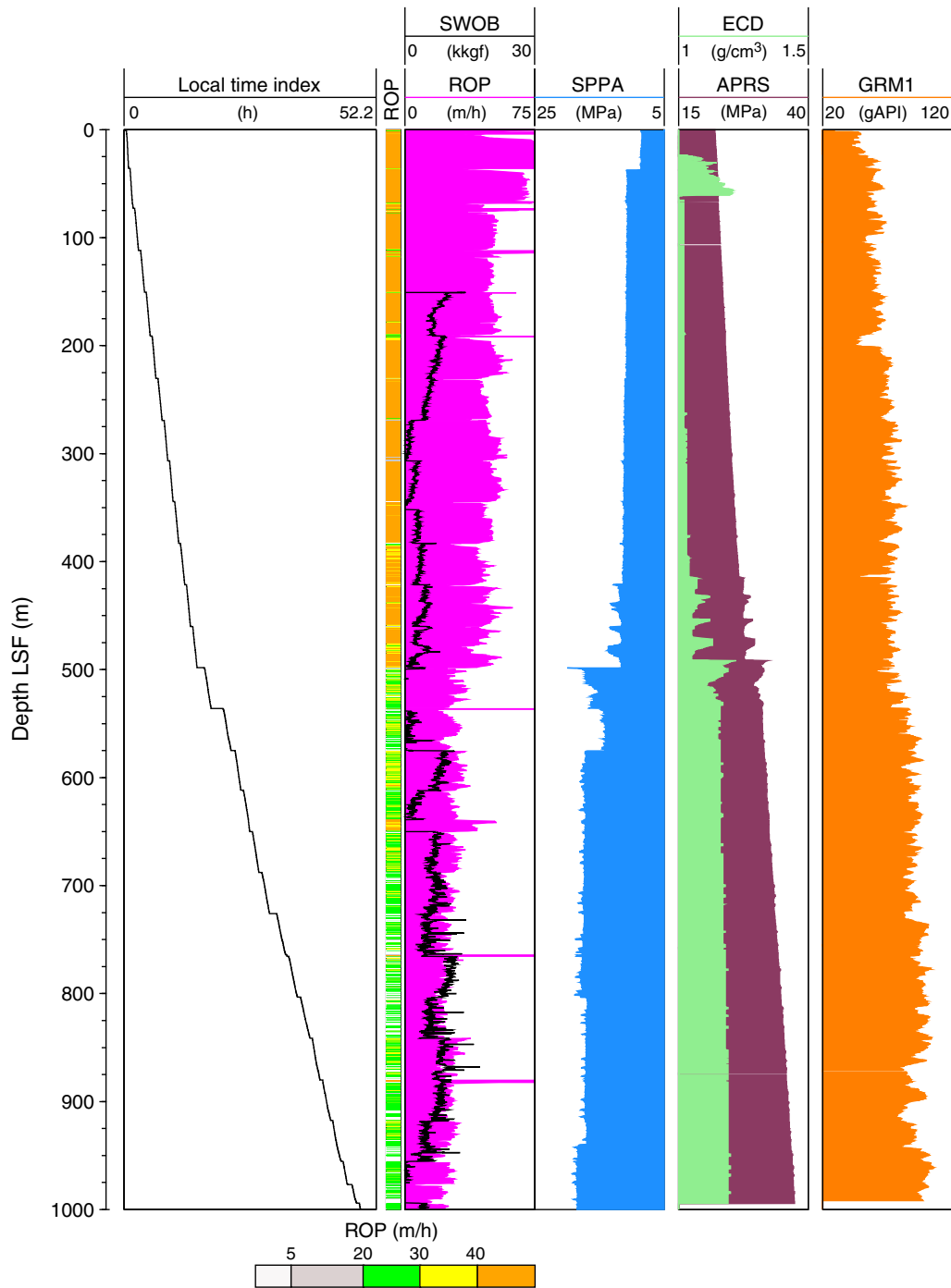
Figure F9. Plot of time-depth relationship in Hole C0001A. LSF = LWD depth below seafloor.
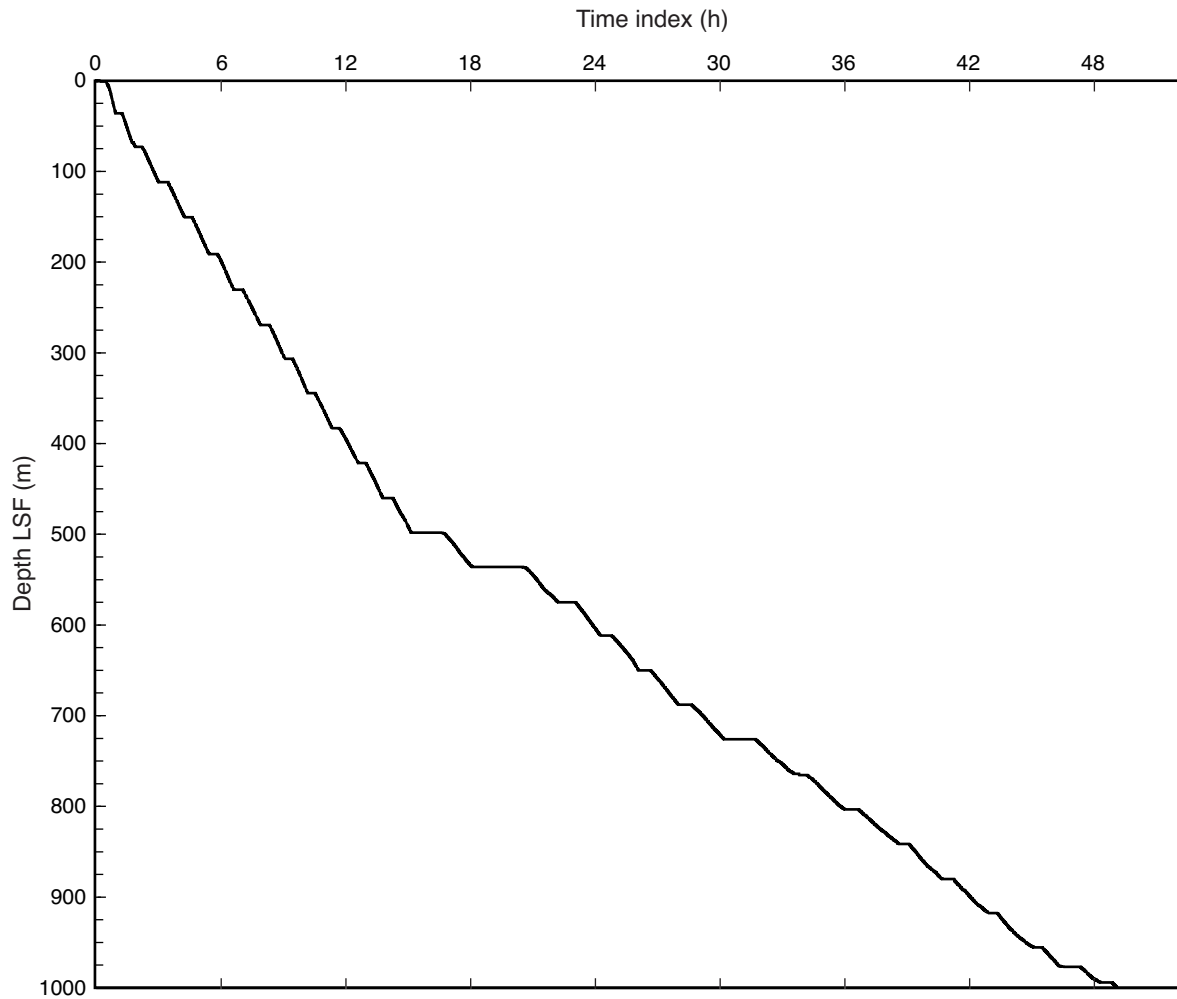
Figure F10. Data flow for Holes C0001C and C0001D. MWD = measurement while drilling, APWD = annular pressure while drilling, LWD = logging while drilling, IDEAL = integrated drilling evaluation and logging system (Schlumberger), GVR = geoVISION resistivity tool, ADN = Azimuthal Density Neutron tool (adnVISION), LAS = log ASCII standard format, DCS = Data Consulting Service (Schlumberger).
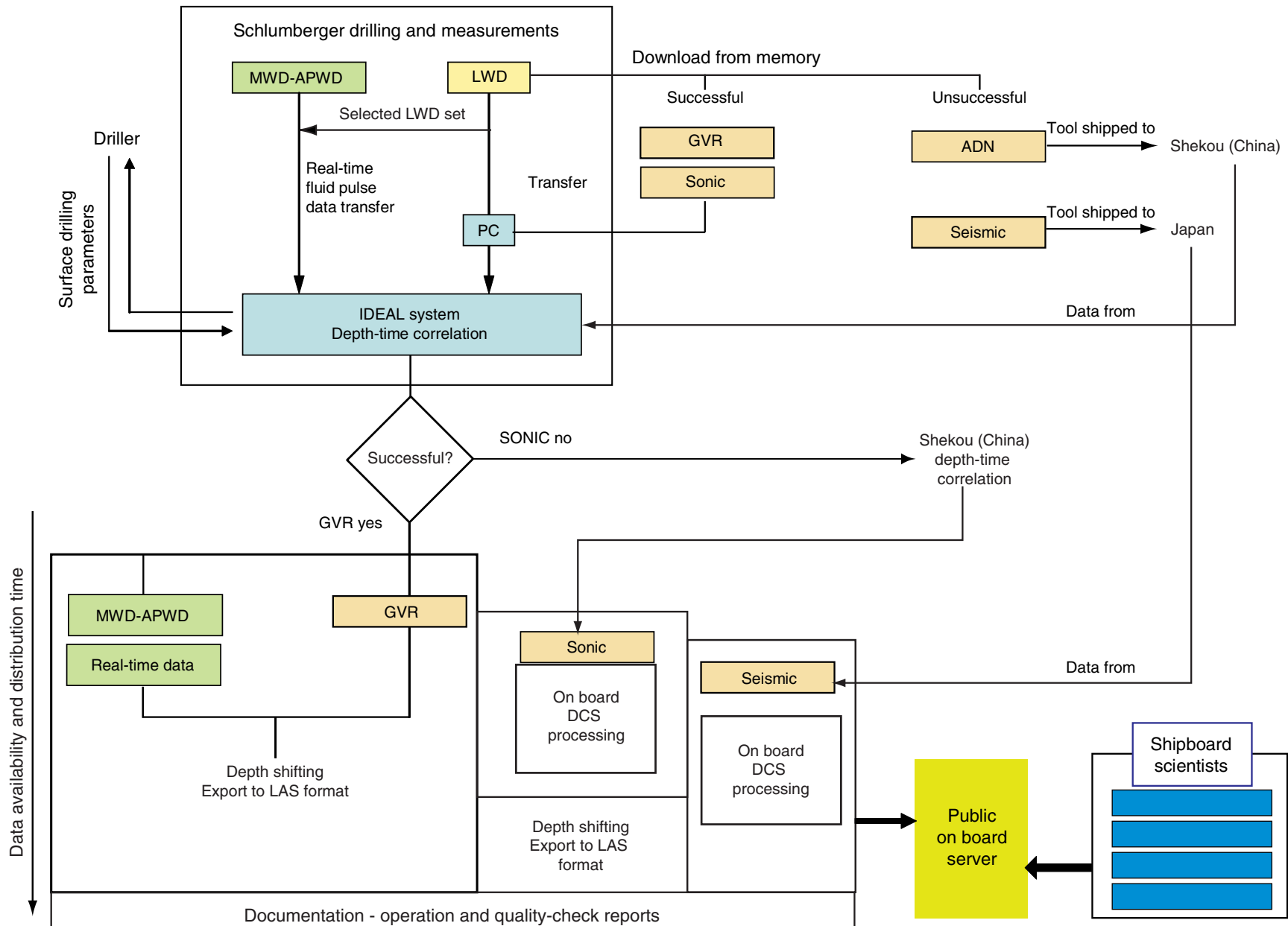
Figure F11. Identification of mudline in Hole C0001C using gamma ray and resistivity logs of the geoVISION tool (memory data). The mudline is identified by a break in the gamma ray and resistivity logs at 2230.5 m drillers depth below rig floor (DRF). Note that resistivity data are plotted on a linear scale. LSF = LWD depth below seafloor.
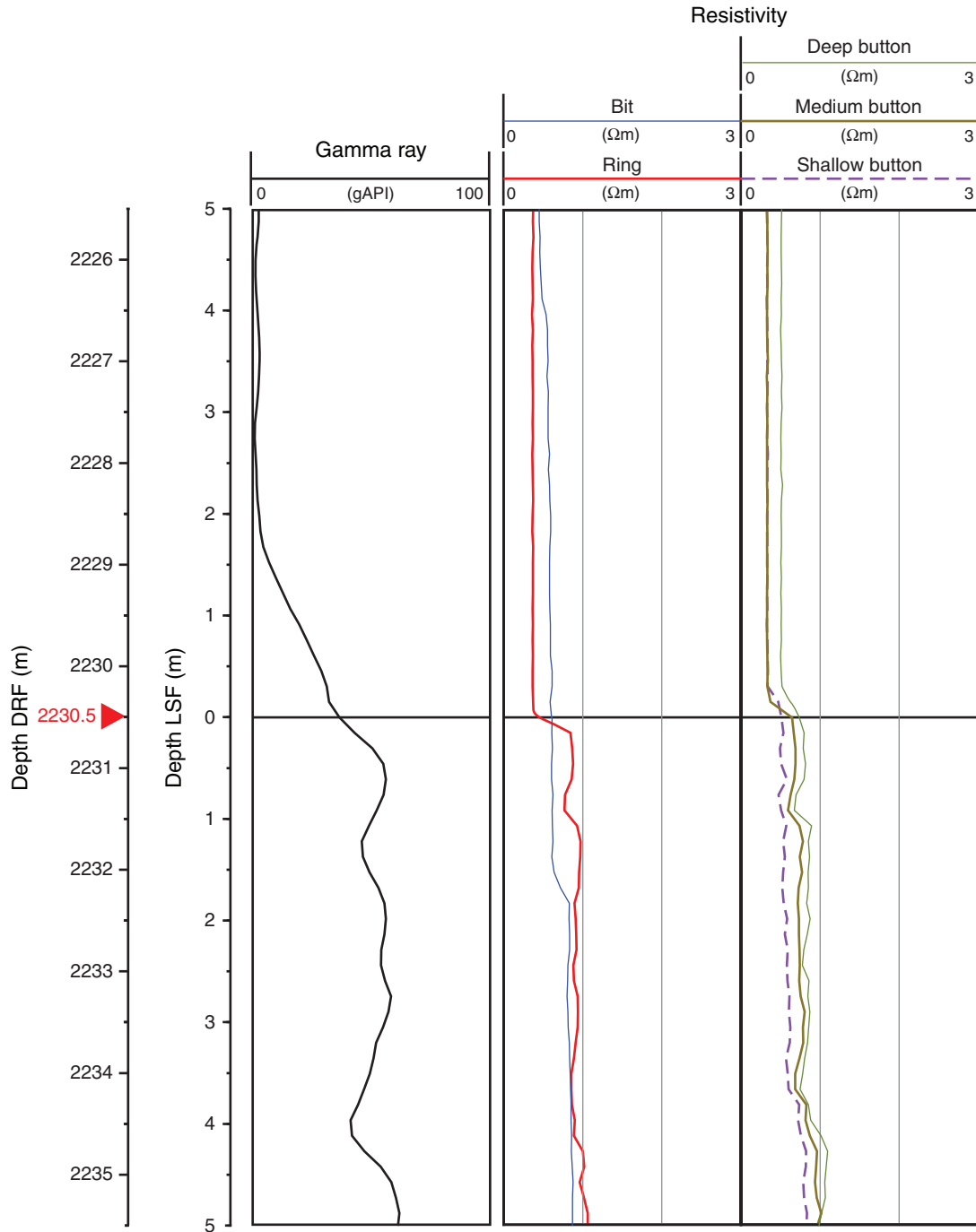
Figure F12. Identification of mudline in Hole C0001D using gamma ray and resistivity logs of the geoVISION tool (memory data). Mudline is identified by a break in the gamma ray and resistivity logs at 2228 m drillers depth below rig floor (DRF). Note that resistivity data are plotted on a linear scale. LSF = LWD depth below seafloor.
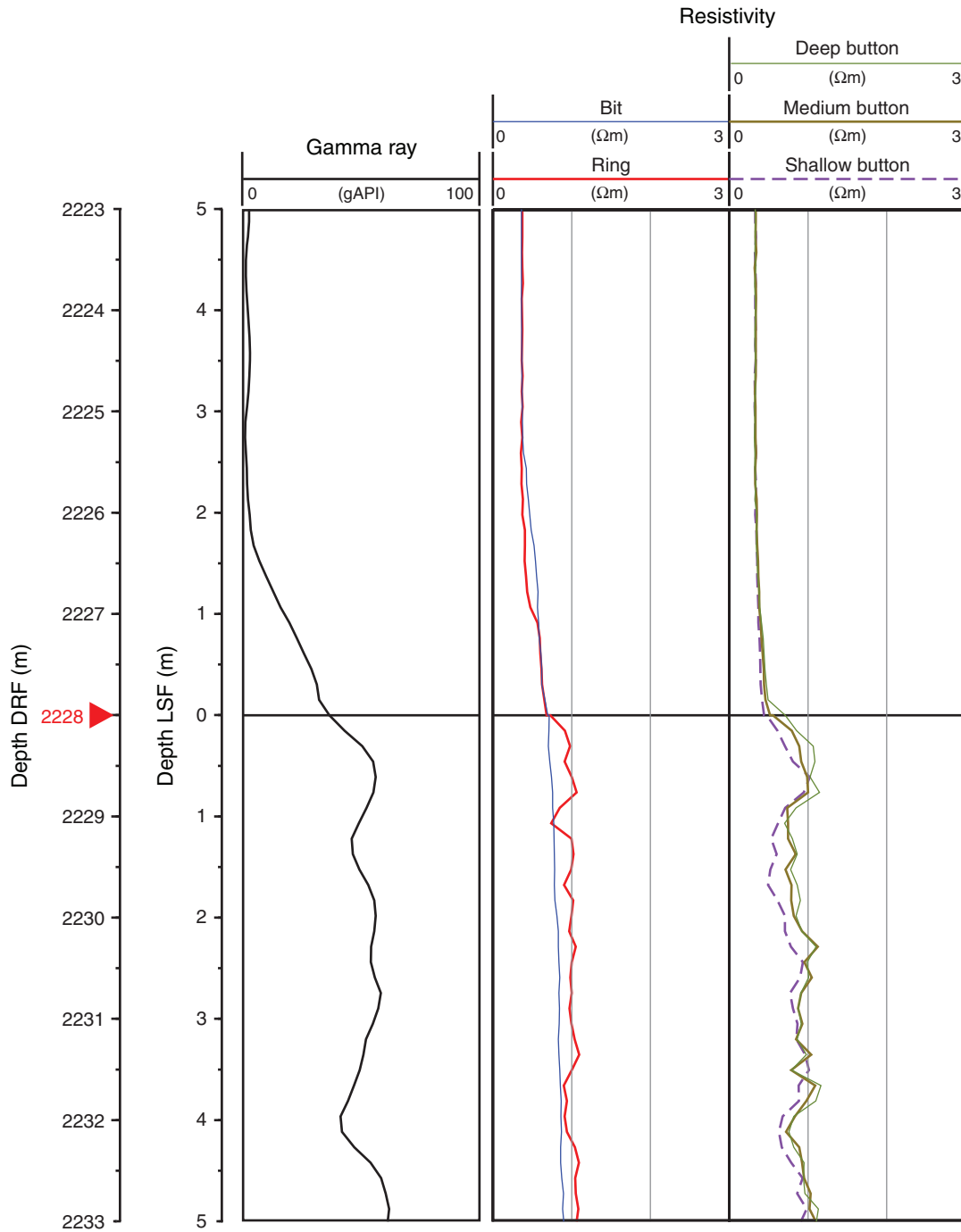
Figure F13. Control logs of Hole C0001C. LSF = LWD depth below seafloor, SWOB = surface weight on bit, ROP = rate of penetration, SPPA = standpipe pressure, HDEVI = hole deviation, ADIA = average borehole diameter, ECD = equivalent circulating density, APRS = average annular pressure, STICK = stick slip indicator, SHK= shock indicator, GR = gamma ray, TAB_RAB_BD = time after bit deep button resistivity, TAB_RAB_RING = time after bit ring resistivity, TAB_RAB_BIT = time after bit resistivity, TAB_RAB_GR = RAB gamma ray time after bit, RES_BIT = resistivity at bit, RES_ BD = deep bottom resistivity, RES_RING = resistivity at ring, RHOB = bulk density, DHRO = bulk density correction.
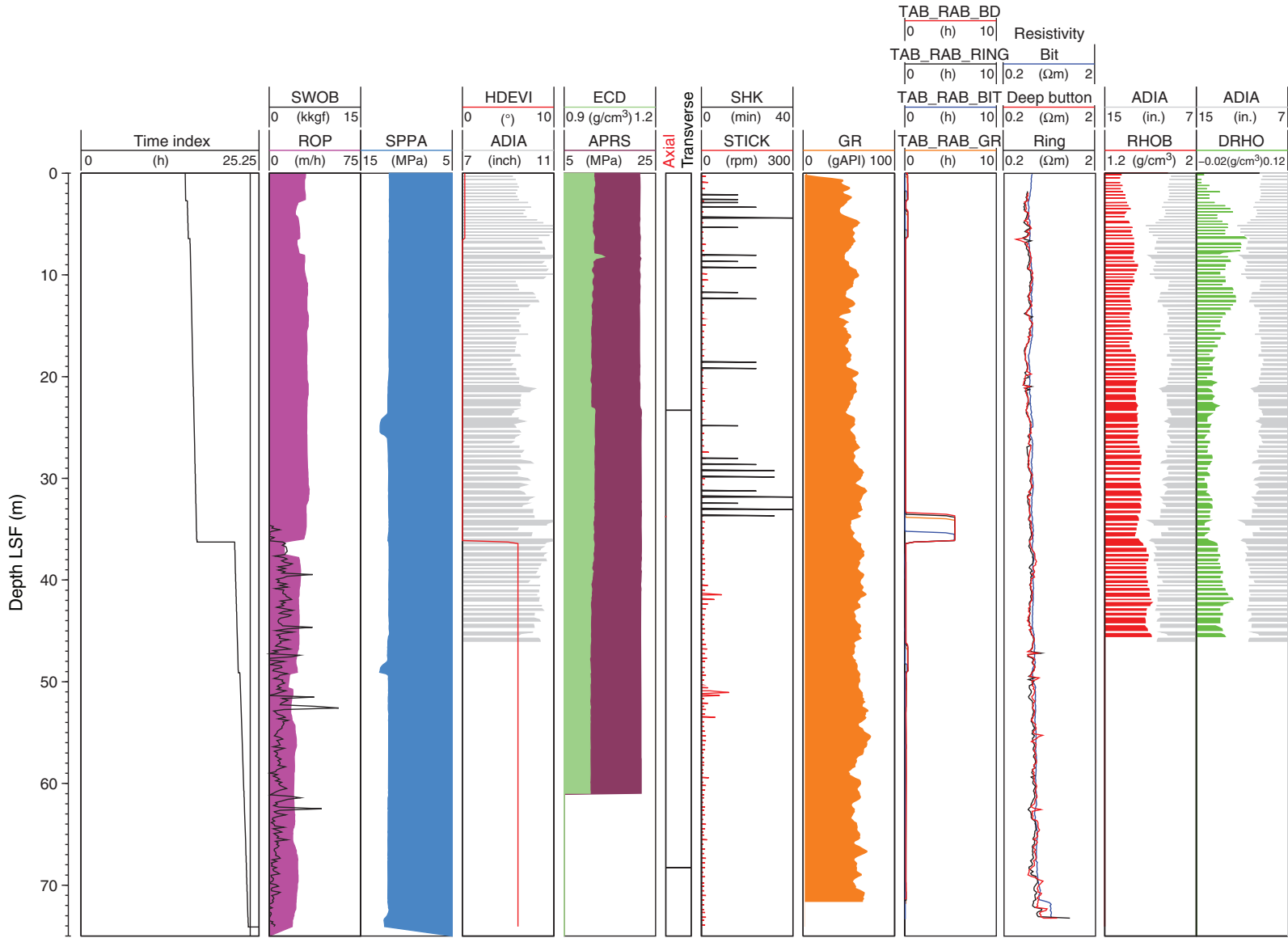
Figure F14. Control logs of Hole C0001D. LSF = LWD depth below seafloor, SWOB = surface weight on bit, ROP = rate of penetration, SPPA = standpipe pressure, HDEVI = hole deviation, ADIA= average borehole diameter, ECD = equivalent circulating density, APRS = average annular pressure, STICK = stick slip indicator, SHK= shock indicator, GR = gamma ray, TAB_RAB_BD = time after bit deep button resistivity, TAB_RAB_RING = time after bit ring resistivity, TAB_RAB_BIT = time after bit resistivity, TAB_RAB_GR = RAB gamma ray time after bit, RES_BIT = resistivity-at-the-bit, RES_ BD = deep button resistivity, RES_RING = resistivity at ring, RHOB = bulk density, DRHO = bulk density correction, V_P = sonic velocity, DTCO = compressional wave slowness, GVR = geoVISION resistivity tool. First vertical color-coded sonic column is indicative of the processing (blue = mostly wide frequency algorithm/processing, green = combination of wide and leaky-P processing). The second vertical column is indicative of data confidence (green = reasonably continuous data interpreted to show formation slowness). (**Figure shown on next page.**)
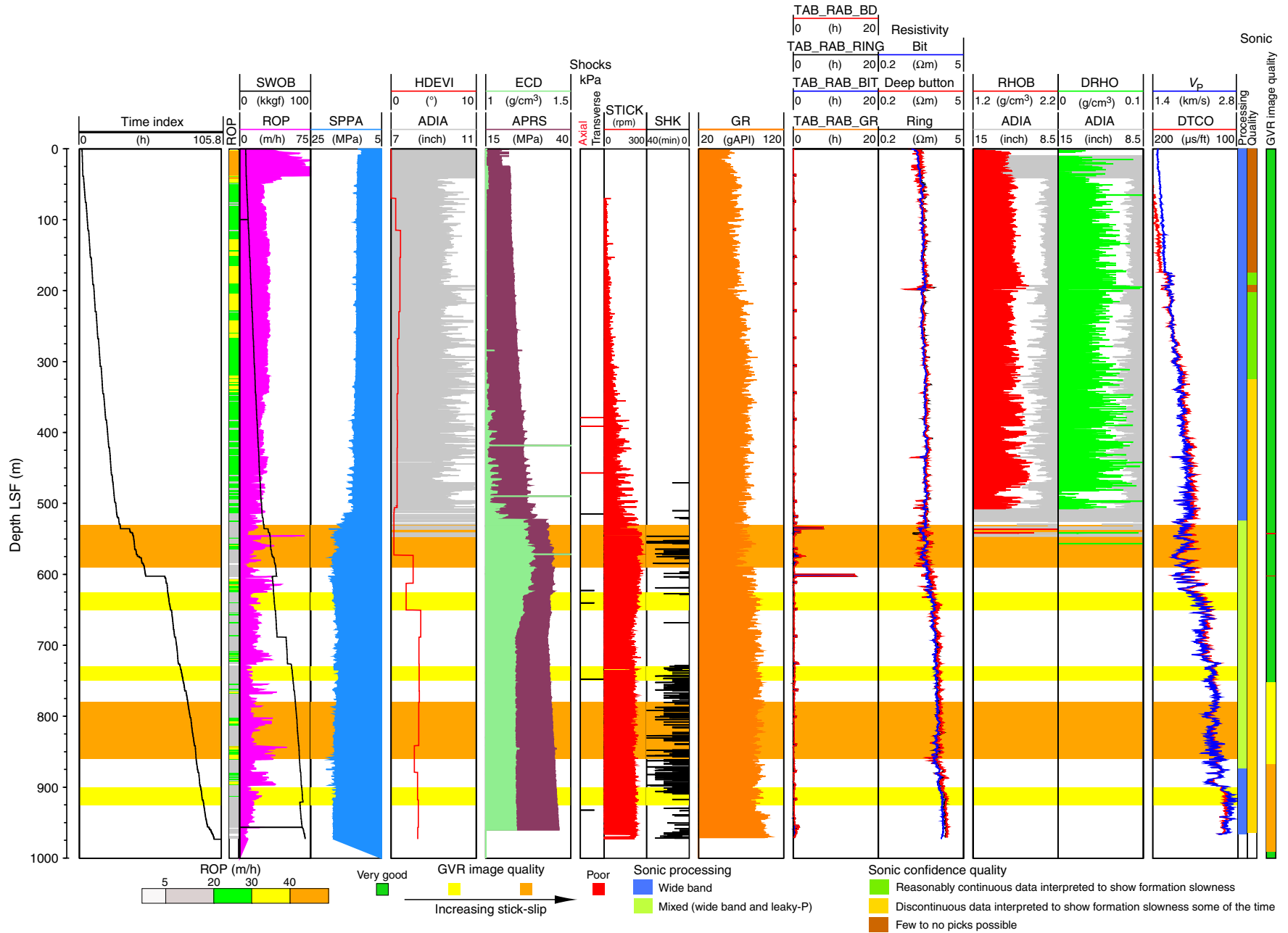
Figure F15. Plot of time-depth relationship in Hole C0001C. LSF = LWD depth below seafloor.
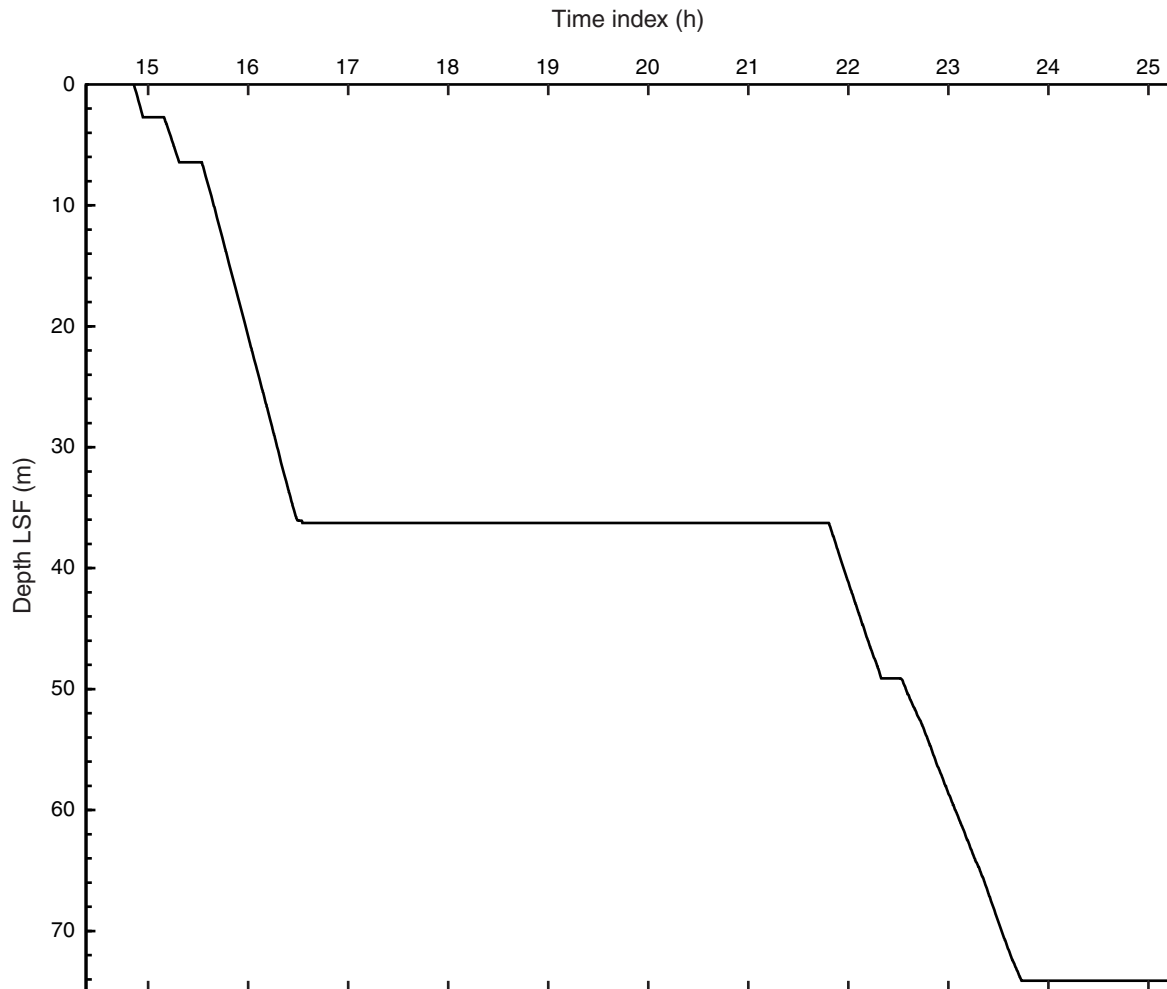
Figure F16. Plot of time-depth relationship in Hole C0001D. LSF = LWD depth below seafloor.
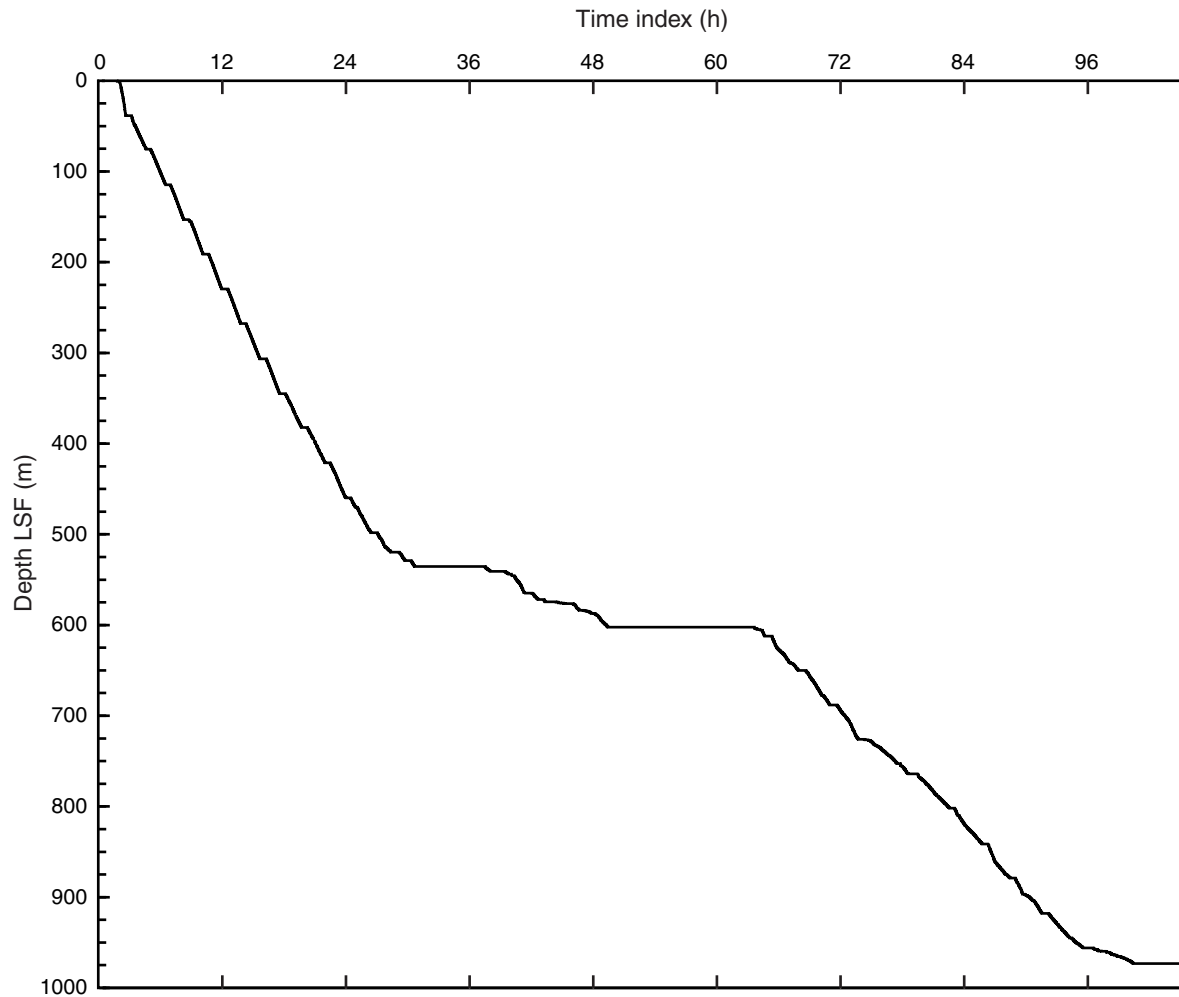
Figure F17. Investigation of borehole condition in Hole C0001D by comparing real-time gamma ray log (GRM1) in Hole C0001A with geoVISION memory gamma ray log (GR) in Hole C0001D. Orange bands = low rate of penetration (ROP) and high standpipe pressure (SPPA) (potential major washouts with possible impact on sonic and resistivity data), yellow bands = potential minor washouts associated either with higher ROP and/or lower SPPA (no noticeable effects on the deep investigation measurements such as V_P and resistivity). LSF = LWD depth below seafloor.
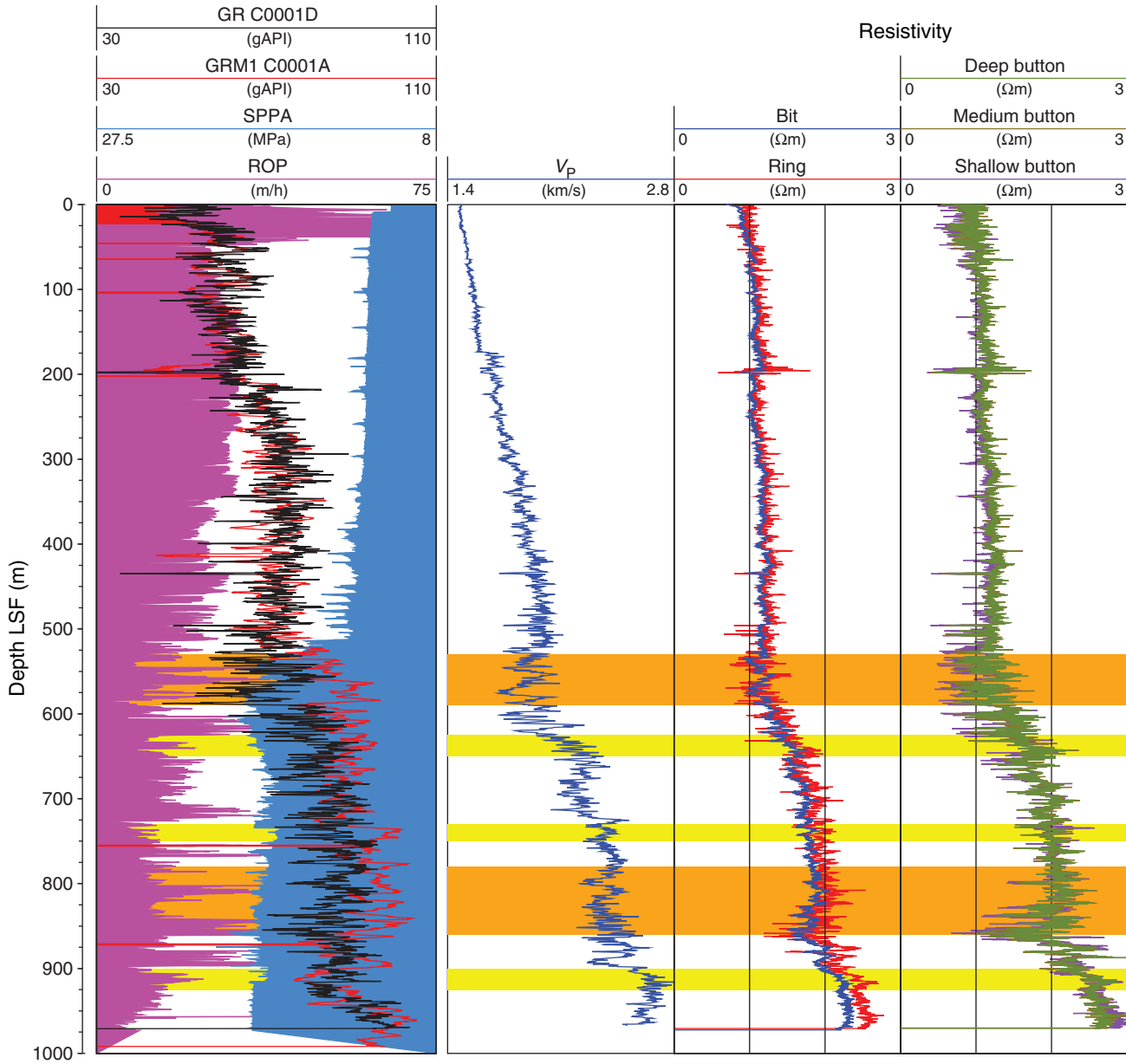
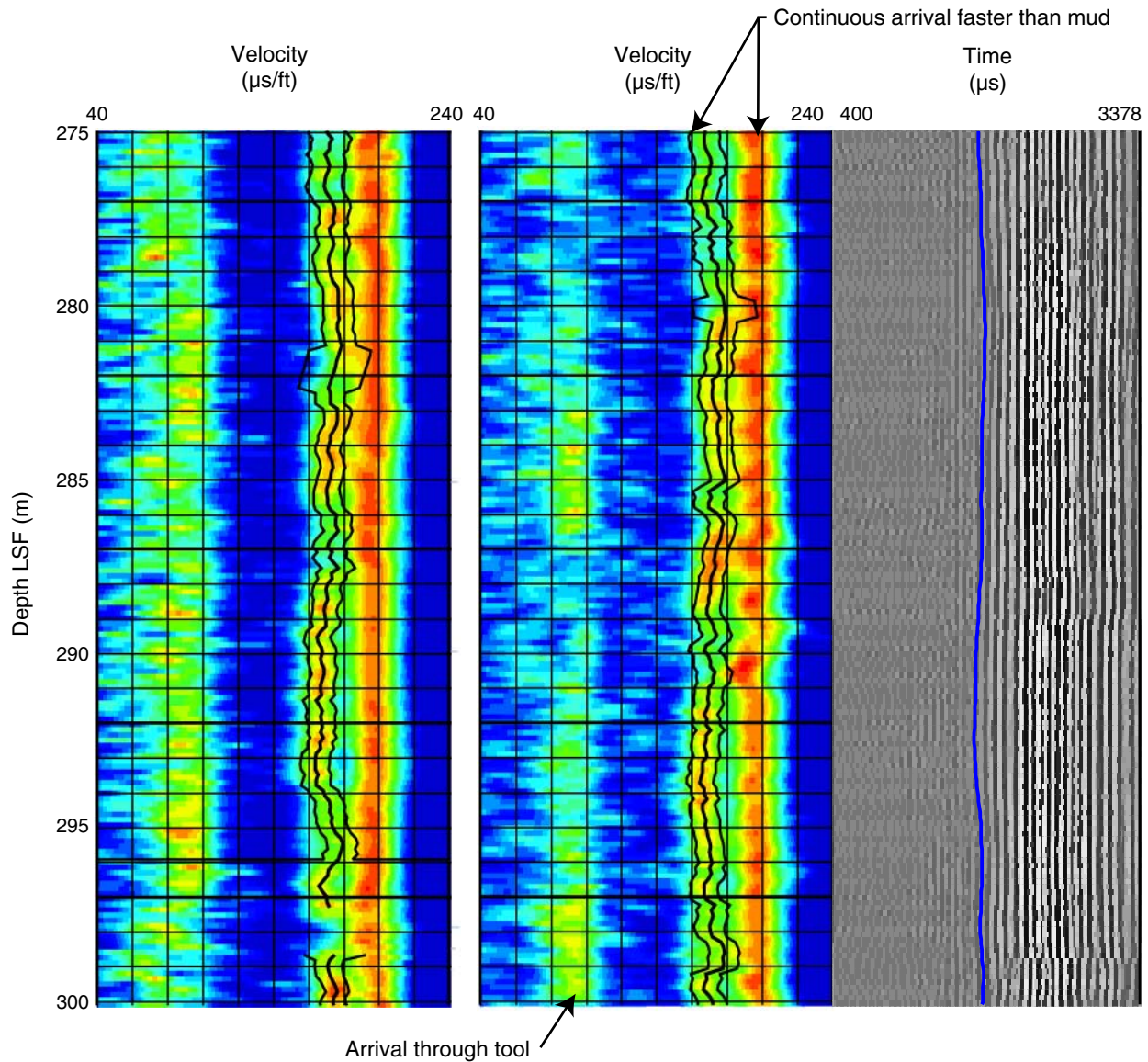**Figure F18.** sonic VISION tool sonic log quality control plot from 0 to 25 m LWD depth below seafloor (LSF). Color panels = slowness coherence plots for the common source and common receiver configurations of the tool. Horizontal axis = slowness, with higher slowness (lower velocity) to the right. Warm colors = high signal strength at a particular slowness. Black lines = manual picks made by Schlumberger Data Consulting Services specialist. Gray-scale plot shows seismograms with time increasing to the right. Blue line = arrival pick associated with slowness identified in picks on left. Final slowness value at a depth is given by the mean of the slownesses picked in the common source and common receiver configurations. This serves to compensate for tool position in the hole.
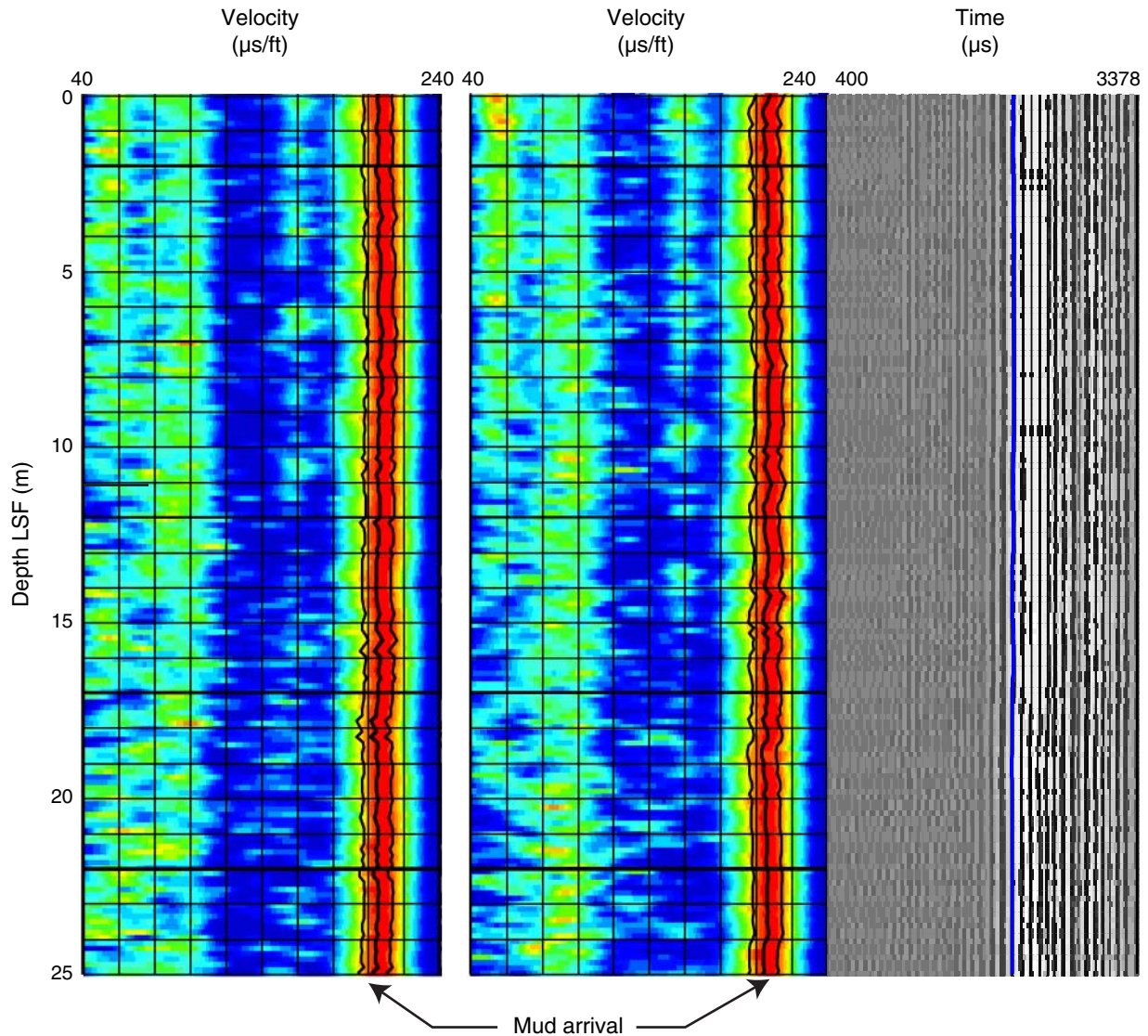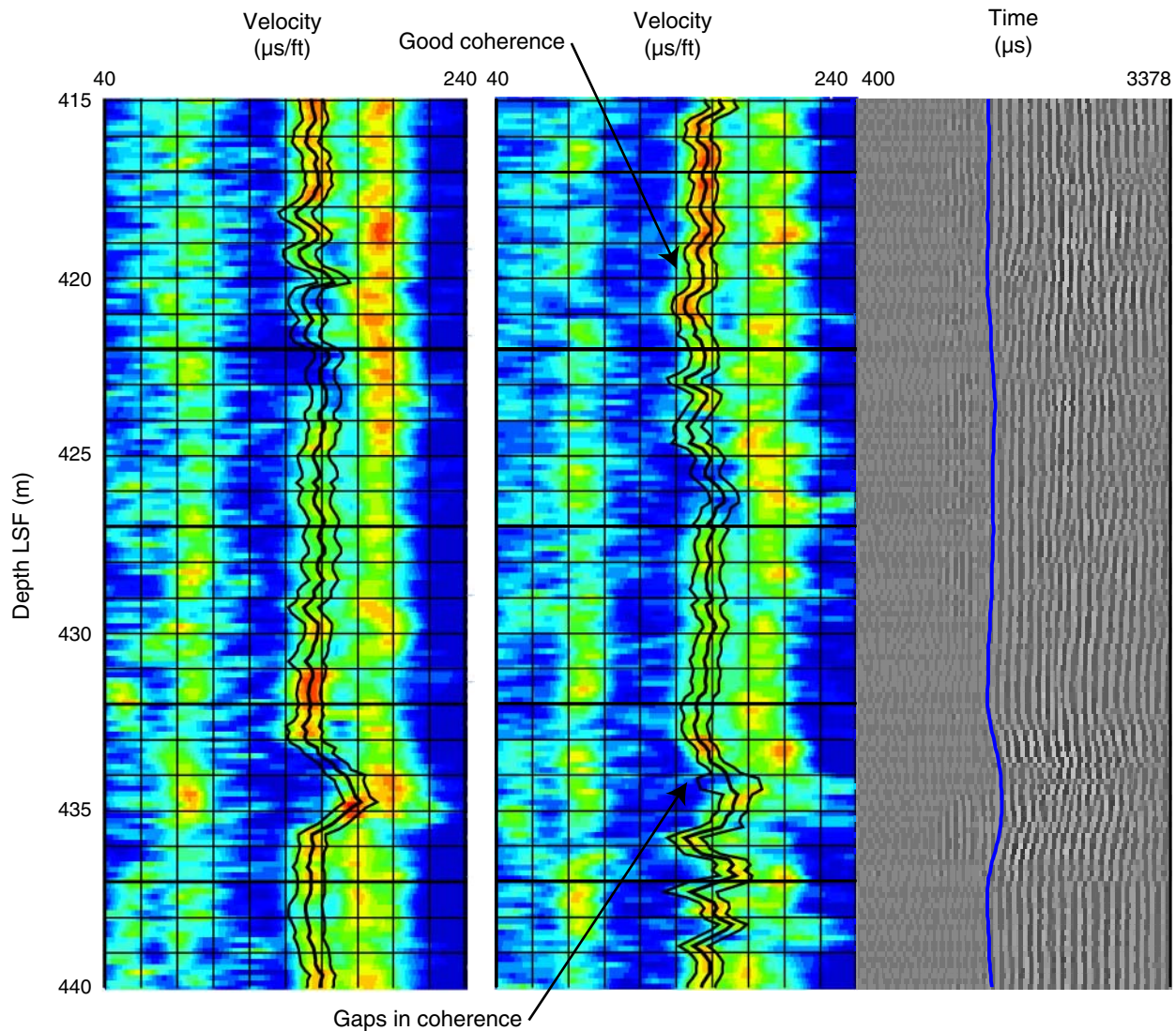
Figure F19. Sonic log quality control plot from 175 to 200 m LWD depth below seafloor (LSF). Color panels are slowness coherence plots for the common source and common receiver configurations of the tool. Horizontal axis is slowness, with higher slowness (lower velocity) to the right. Warm colors = high signal strength at a particular slowness. Black lines = manual picks made by Schlumberger Data Consulting Services specialist. Grayscale plot shows seismograms with time increasing to the right. Blue line = arrival pick associated with slowness identified in picks on left. Final slowness value at a depth is given by the mean of the slownesses picked in the common source and common receiver configurations. This serves to compensate for tool position in the hole.
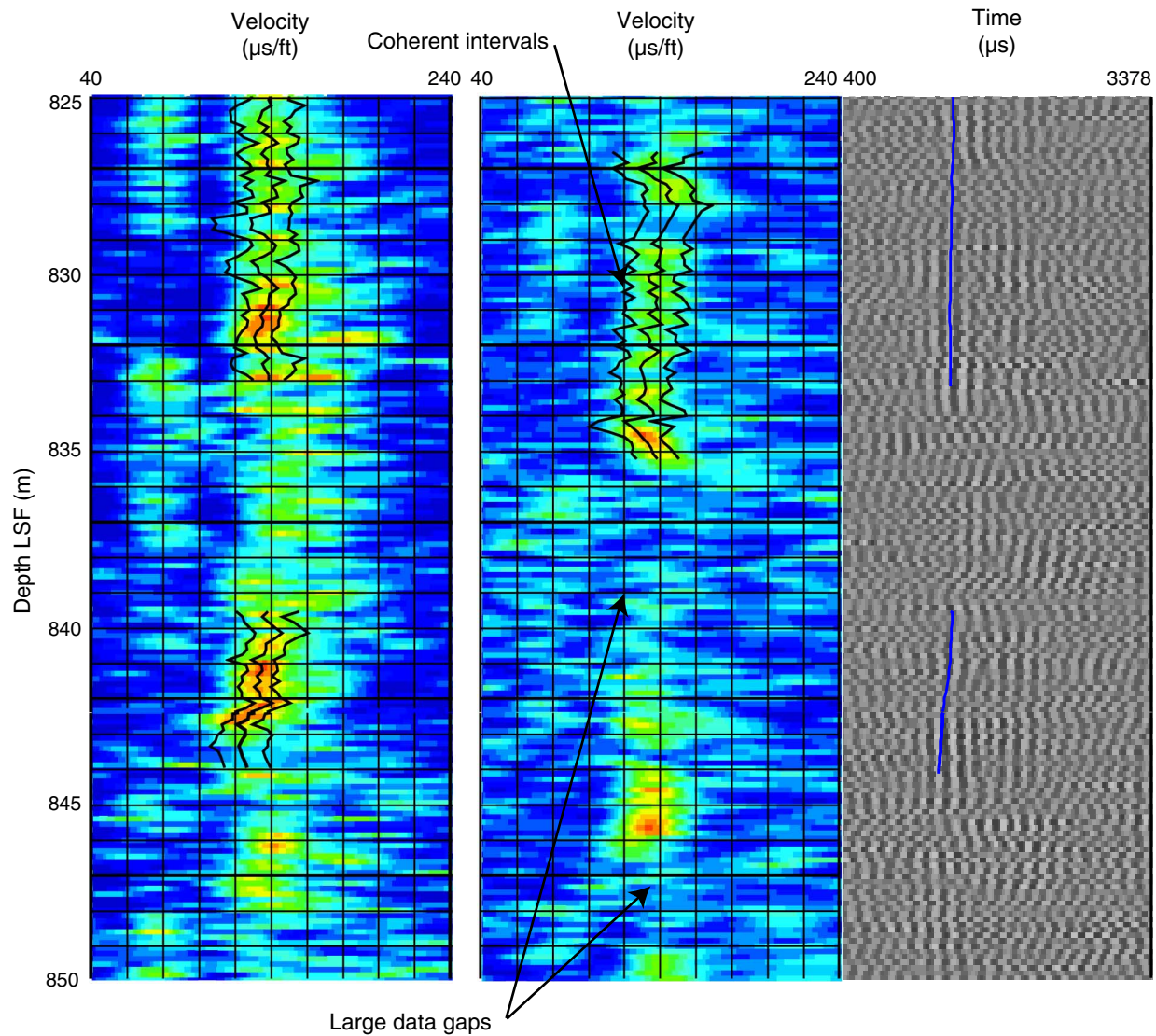
Figure F20. Sonic log quality control plot from 275 to 300 m LWD depth below seafloor (LSF). Color panels are slowness coherence plots for the common source and common receiver configurations of the tool. Horizontal axis is slowness, with higher slowness (lower velocity) to the right. Warm colors = high signal strength at a particular slowness. Black lines = manual picks made by Schlumberger Data Consulting Services specialist. Grayscale plot shows seismograms with time increasing to the right. Blue line = arrival pick associated with slowness identified in picks on left. Final slowness value at a depth is given by the mean of the slownesses picked in the common source and common receiver configurations. This serves to compensate for tool position in the hole.

Figure F21. Sonic log quality control plot from 415–440 m LWD depth below seafloor (LSF). Color panels are slowness coherence plots for the common source and common receiver configurations of the tool. Horizontal axis is slowness, with higher slowness (lower velocity) to the right. Warm colors = high signal strength at a particular slowness. Black lines = manual picks made by Schlumberger Data Consulting Services specialist. Grayscale plot shows seismograms with time increasing to the right. Blue line = arrival pick associated with slowness identified in picks on left. Final slowness value at a depth is given by the mean of the slownesses picked in the common source and common receiver configurations. This serves to compensate for tool position in the hole.

Figure F22. Sonic log quality control plot from 825–850 m LWD depth below seafloor (LSF). Color panels are slowness coherence plots for the common source and common receiver configurations of the tool. Horizontal axis is slowness, with higher slowness (lower velocity) to the right. Warm colors = high signal strength at a particular slowness. Black lines = manual picks made by Schlumberger Data Consulting Services specialist. Grayscale plot shows seismograms with time increasing to the right. Blue line = arrival pick associated with slowness identified in picks on left. Final slowness value at a depth is given by the mean of the slownesses picked in the common source and common receiver configurations. This serves to compensate for tool position in the hole.

Figure F23. Sonic log quality control plot from 900–925 m LWD depth below seafloor (LSF). Color panels are slowness coherence plots for the common source and common receiver configurations of the tool. Horizontal axis is slowness, with higher slowness (lower velocity) to the right. Warm colors = high signal strength at a particular slowness. Black lines are manual picks made by Schlumberger Data Consulting Services specialist. Grayscale plot shows seismograms with time increasing to the right. Blue line = arrival pick associated with slowness identified in picks on left. Final slowness value at a depth is given by the mean of the slownesses picked in the common source and common receiver configurations. This serves to compensate for tool position in the hole.
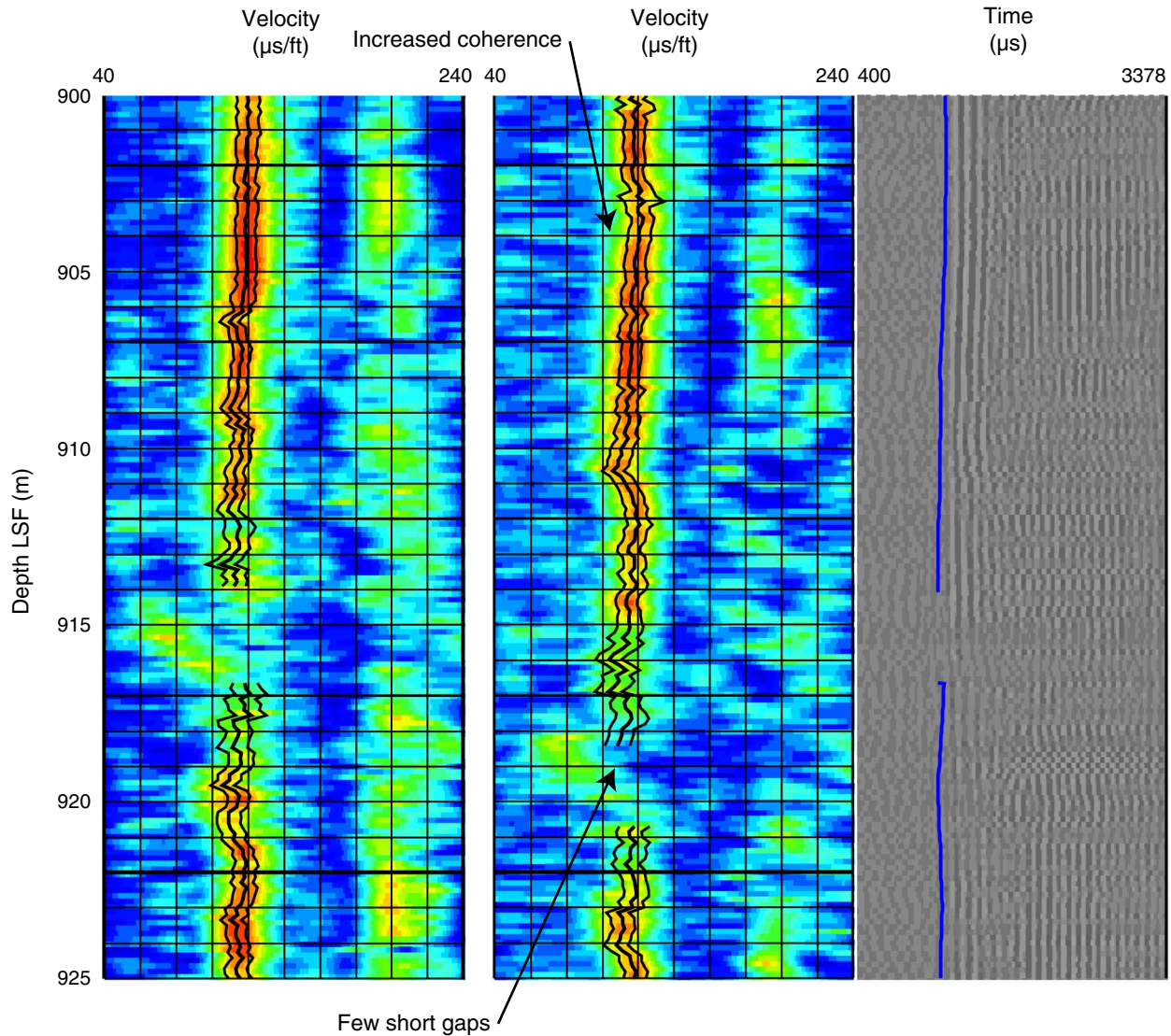
Figure F24. Display of LWD log data and resistivity images obtained at 78 m LWD depth below seafloor (LSF) in Hole C0001C. ROP = rate of penetration.
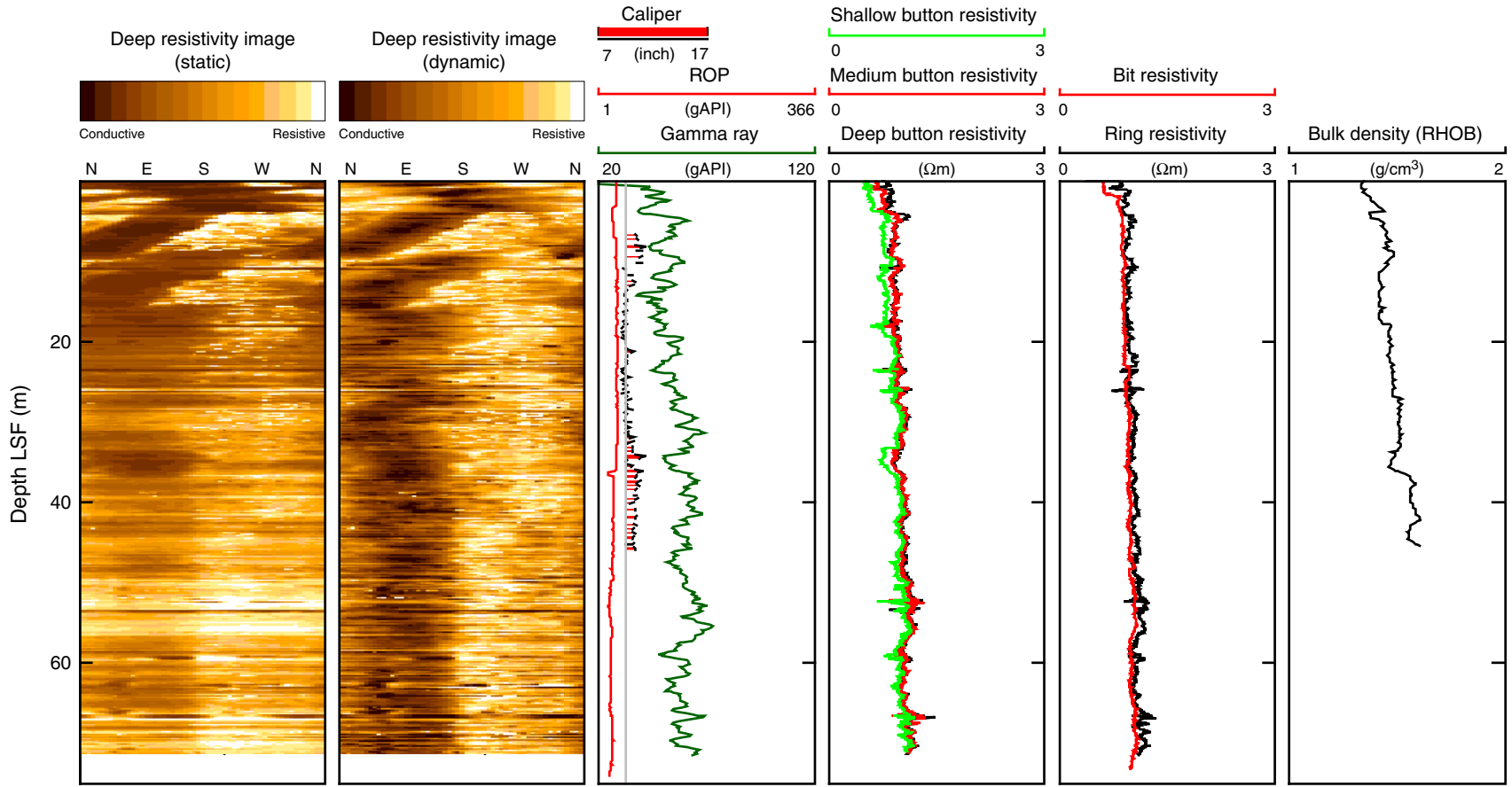
Figure F25. Statistical variation exhibited by main logging units.
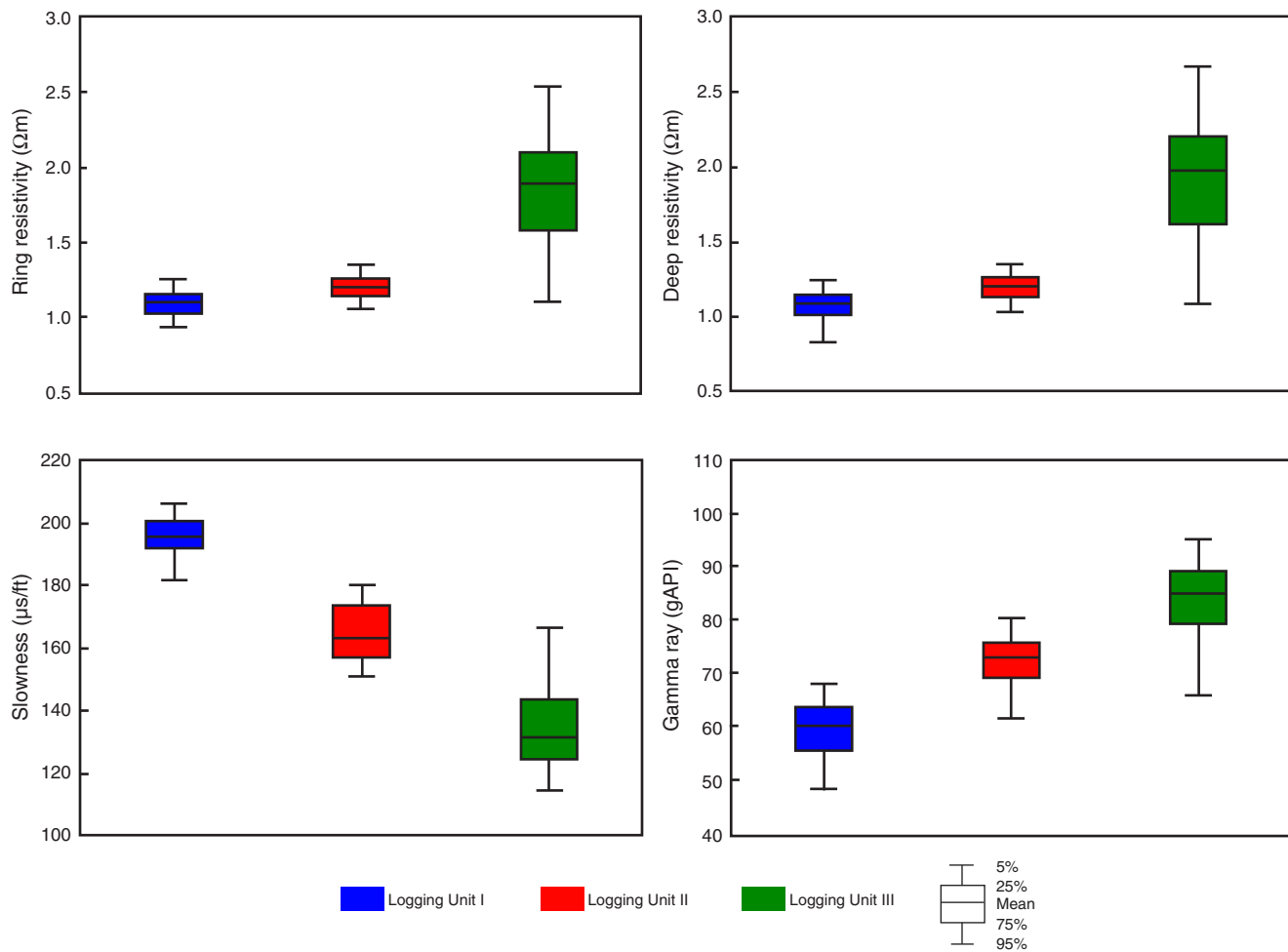
Figure F26. Statistical variation exhibited by logging subunits.
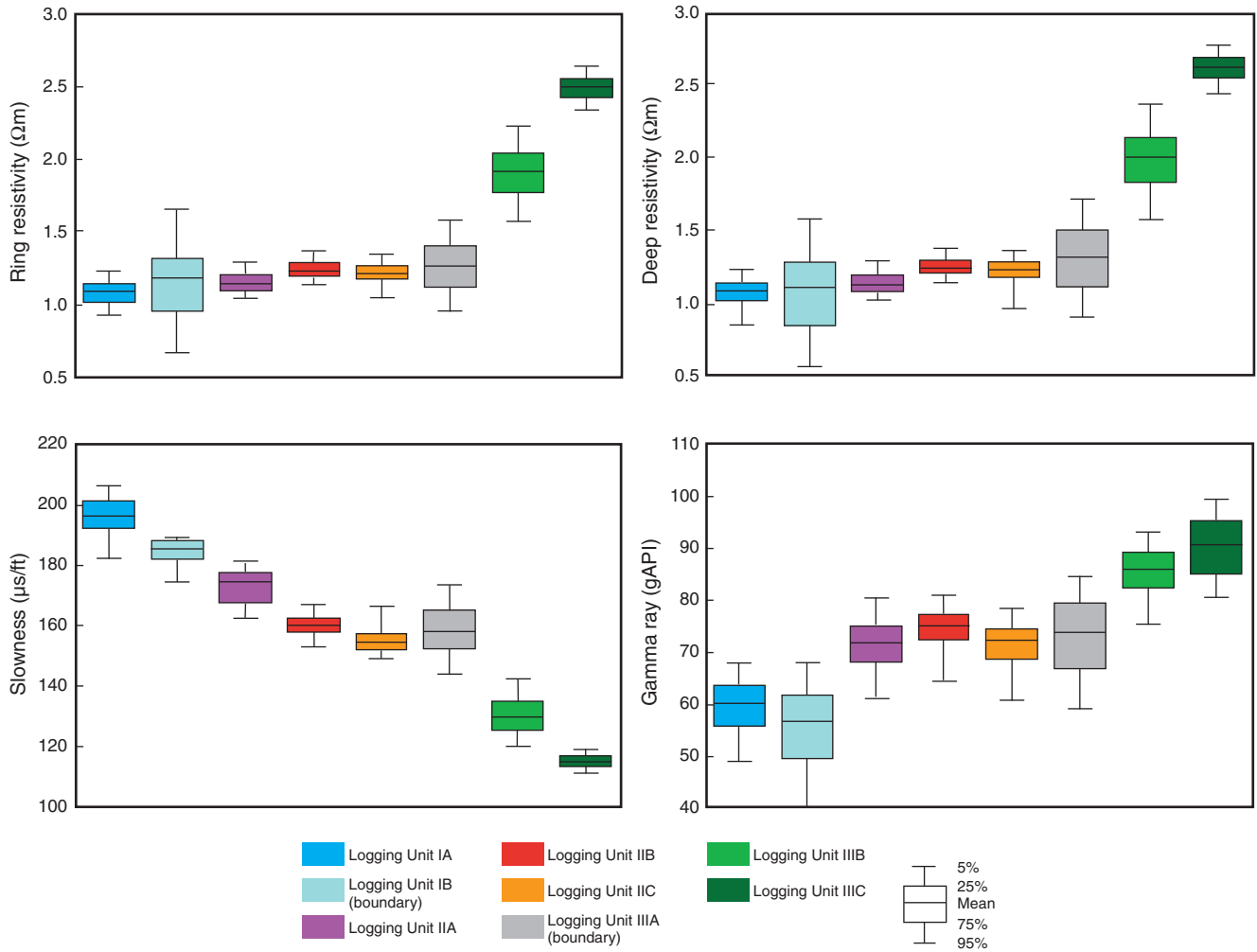
Figure F27. Log-plot illustrating variation in log responses between logging Units II and III. LSF = LWD depth below seafloor.
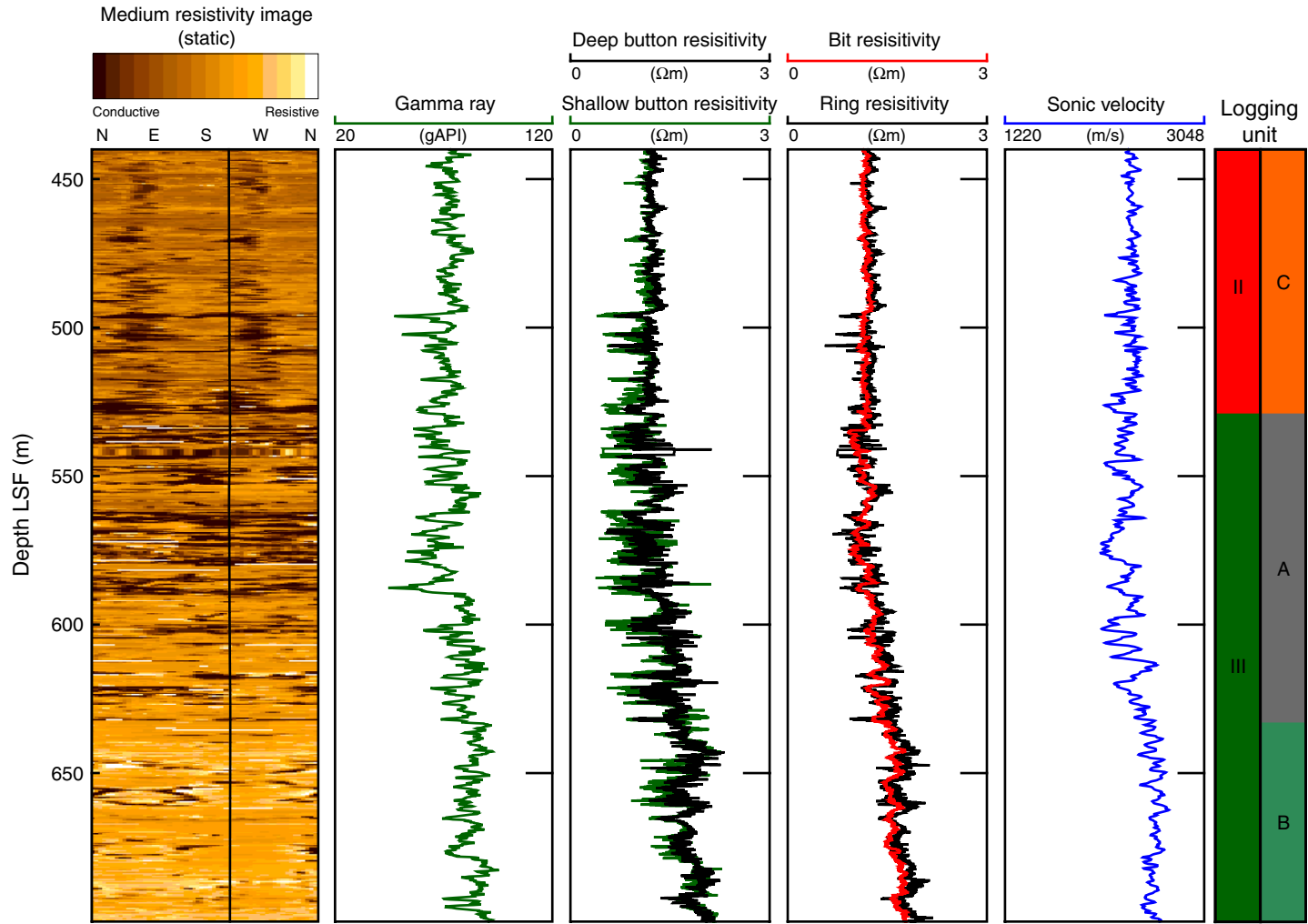
Figure F28. Trends and cyclicity in the gamma ray log and resistivity at bit (RAB) image (shallow, static) for the full section. LSF = LWD depth below seafloor. Orange arrows = meter-scale trends, black arrows = decametric trends, blue arrows = four decametric cycles in logging Subunit IA.
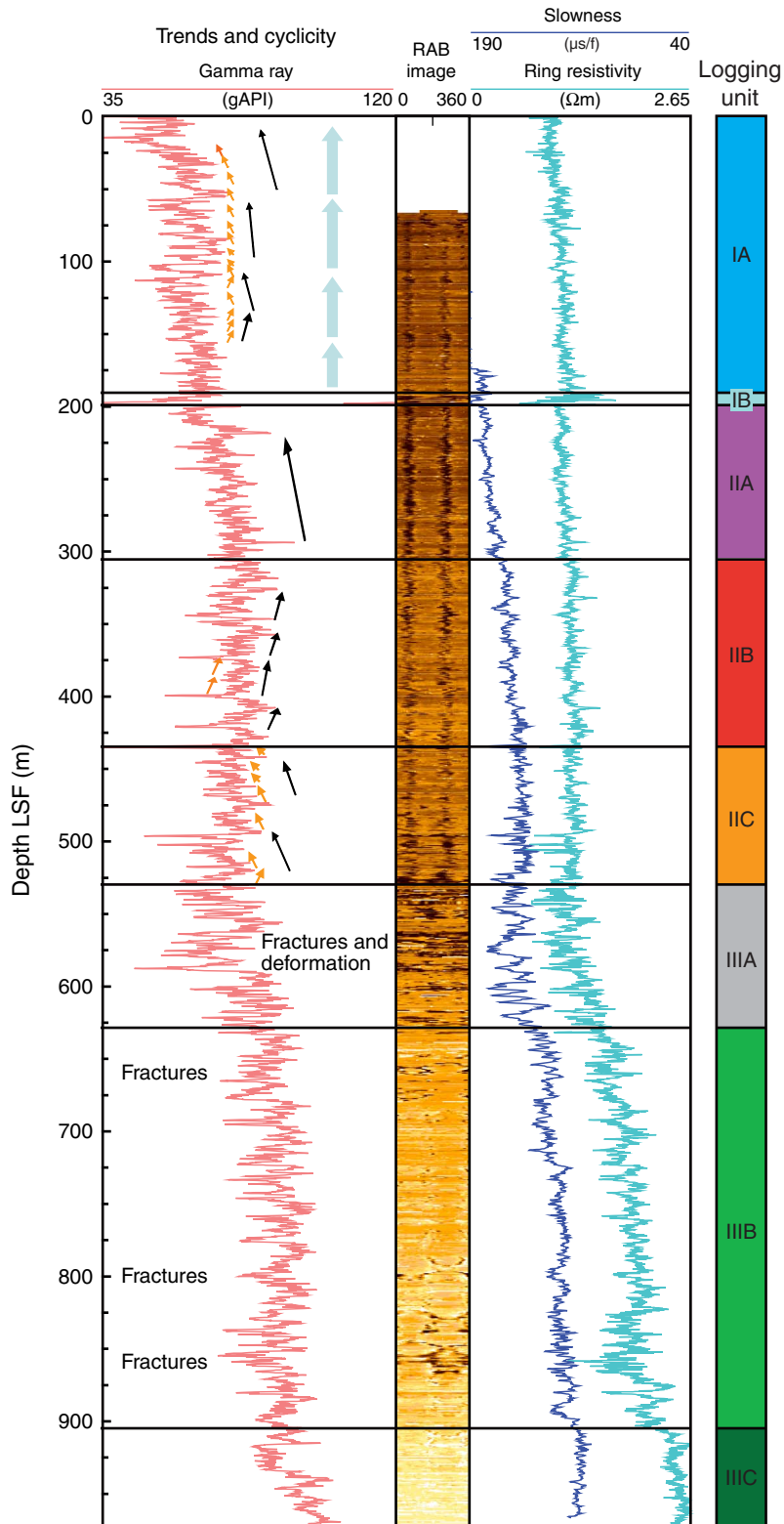
Figure F29. Correlation of logging units to the three-dimensional seismic reflection data around the drill site. SSF = seismic depth below seafloor.
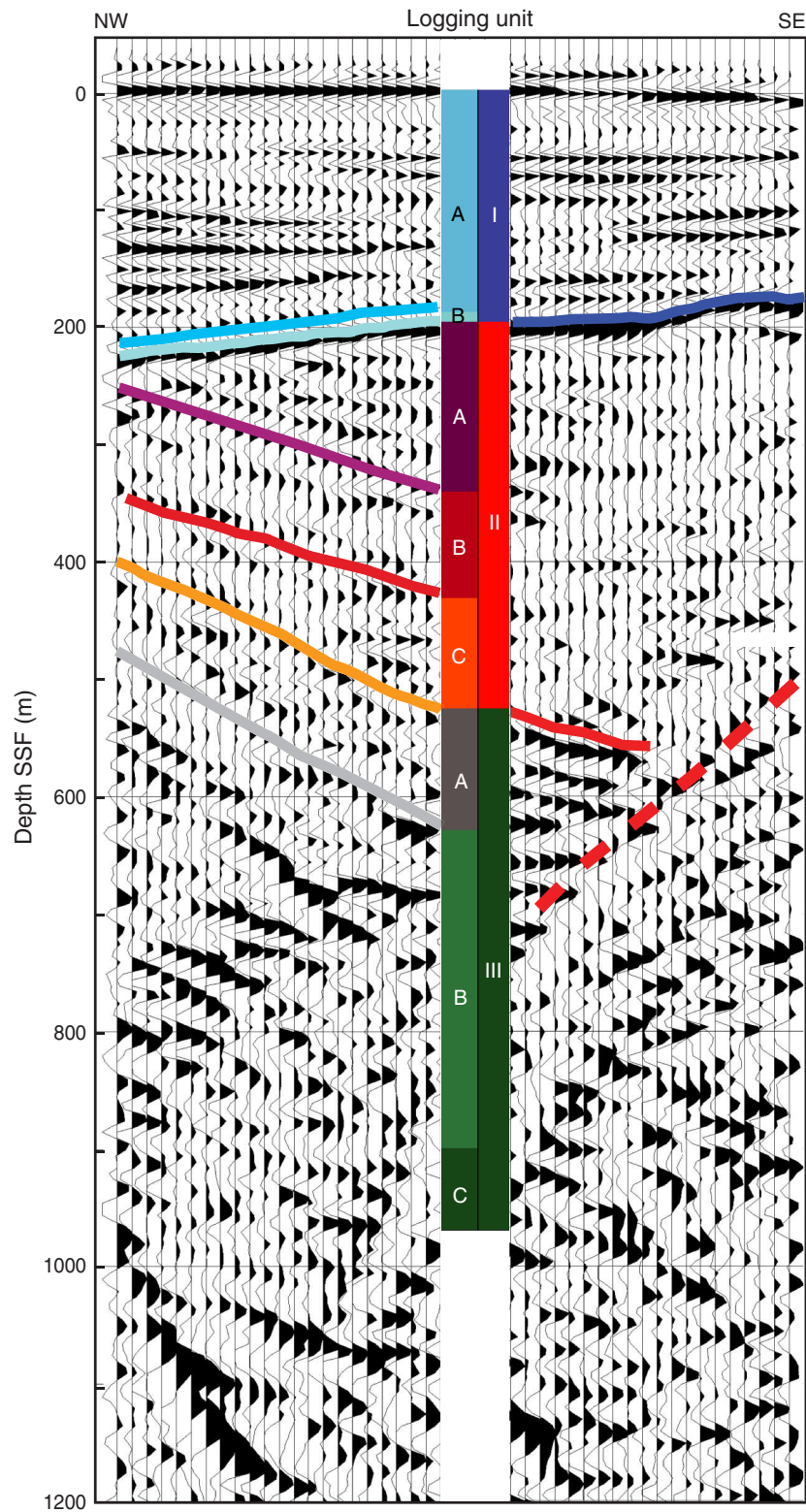
Figure F30. Image-derived density data (IDRO) profile from Hole C0001D. LSF = LWD depth below seafloor.
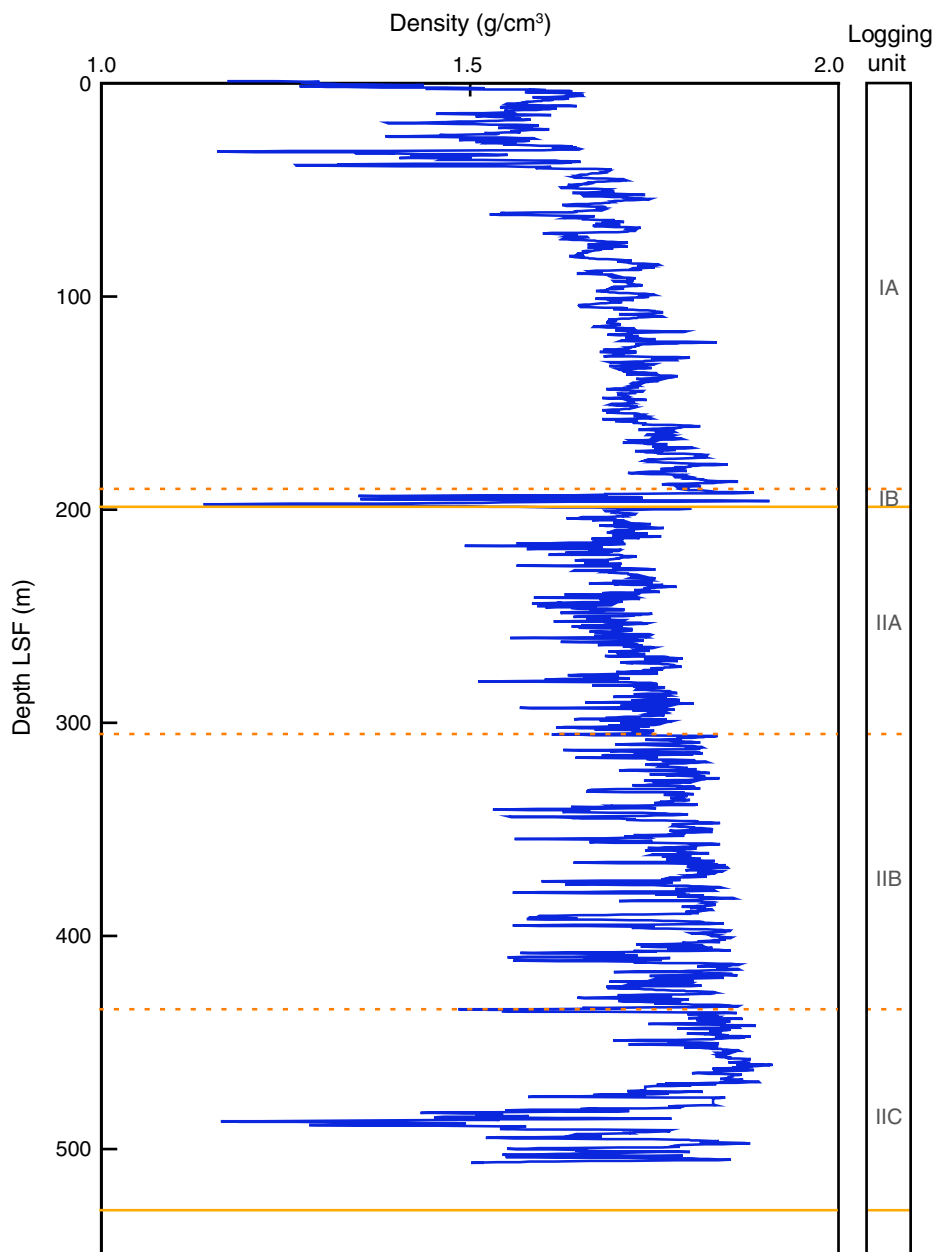
Figure F31. Neutron porosity (TNPH) data profile from Hole C0001D. LSF = LWD depth below seafloor.
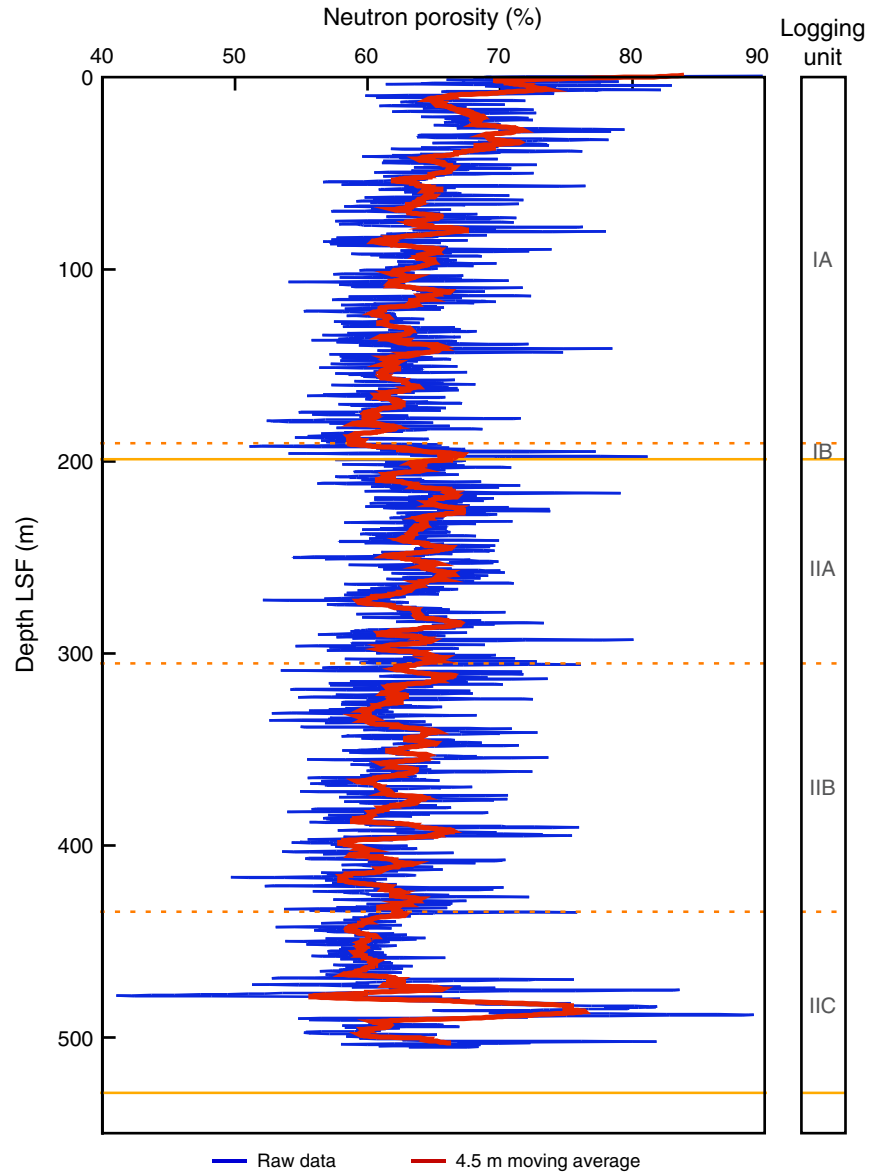
Figure F32. Smoothed ring and bit resistivity logs and smoothed shallow, medium, and deep button resistivity log. The smoothing results from a moving average of the resistivity values using a 21-point (~3 m) window. LSF = LWD depth below seafloor.
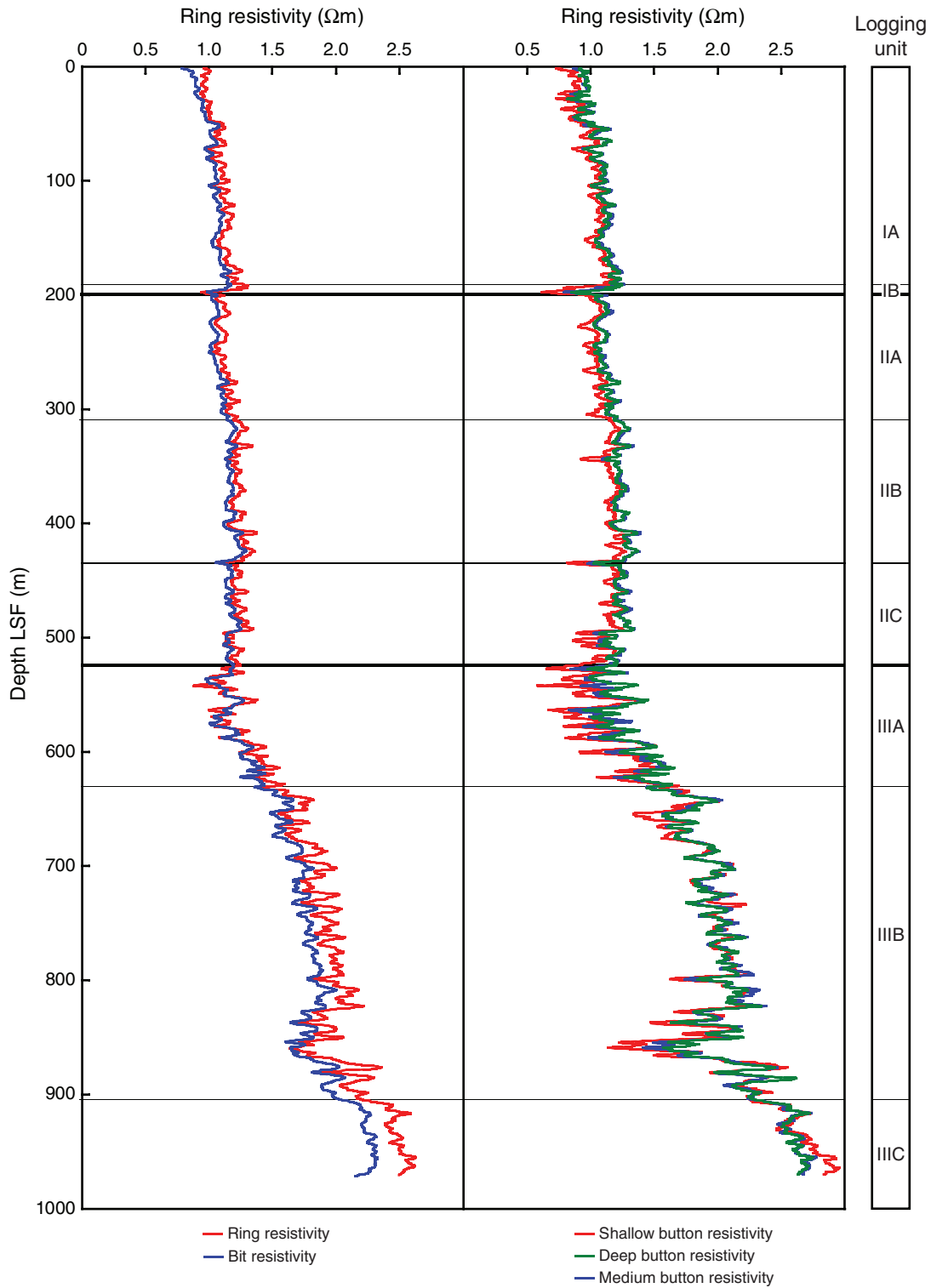
Figure F33. Correlation diagrams of (**A**) bit vs. ring resistivity and (**B**) shallow vs. deep resistivity. Black line = line of unit slope passing through origin, blue line = linear fit to data.
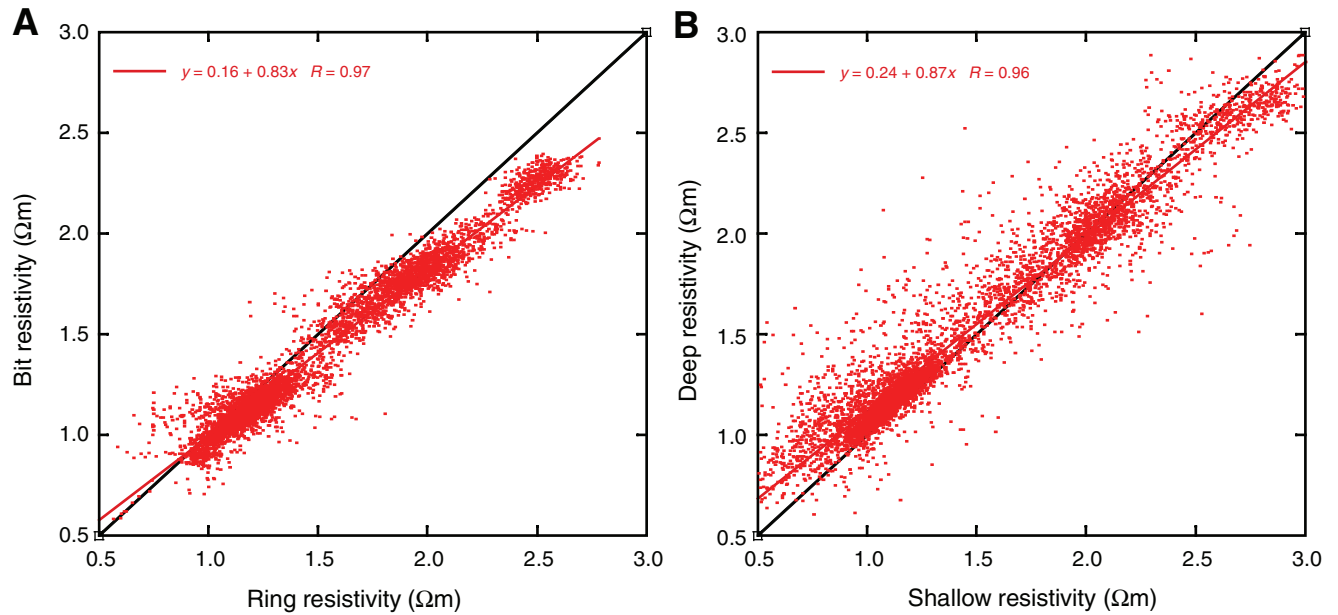
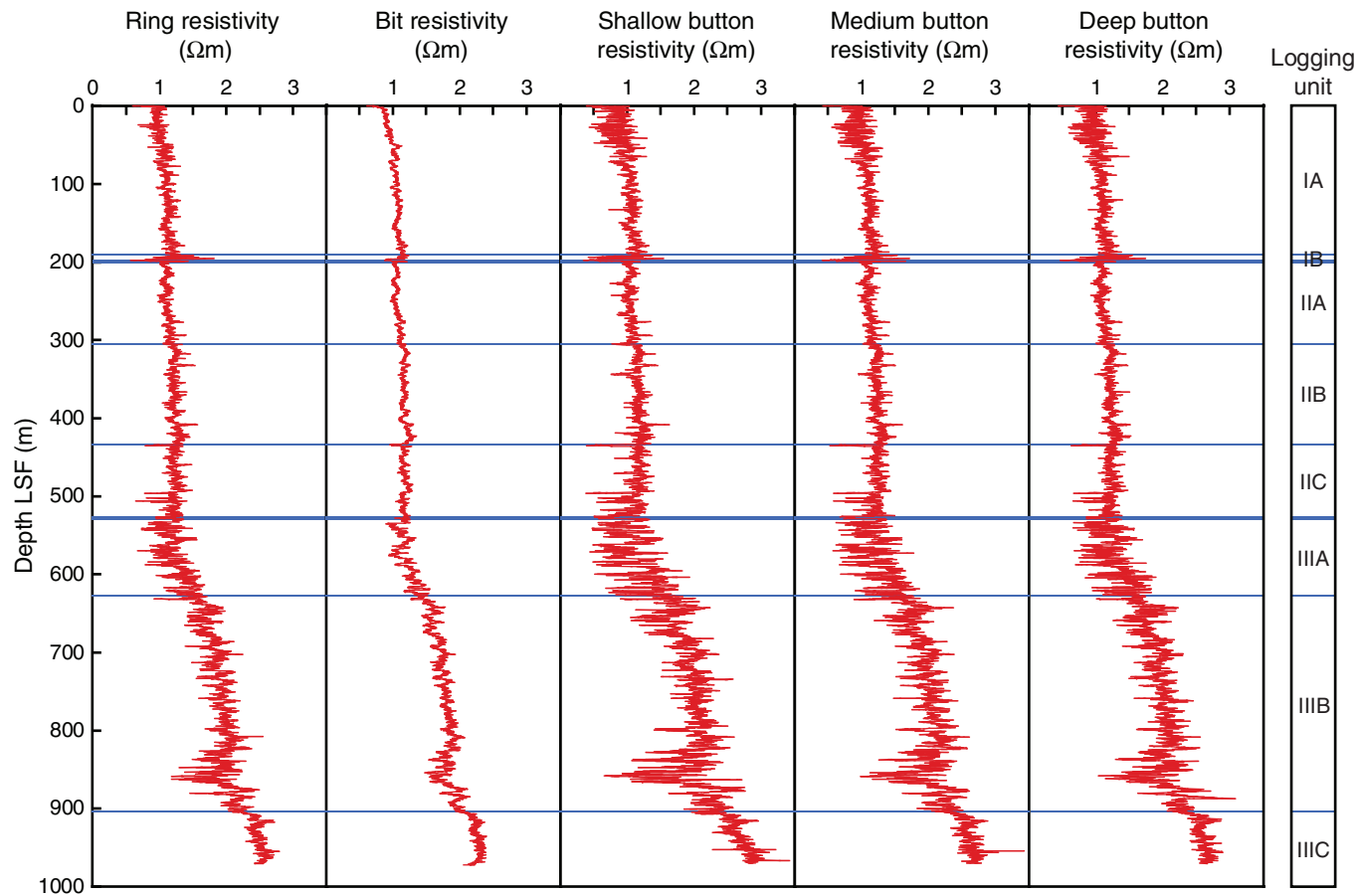**Figure F34.** All resistivity curves acquired in Hole C0001D. LSF = LWD depth below seafloor.

Figure F35. Sonic velocity profile in Hole C0001D. LSF = LWD depth below seafloor.
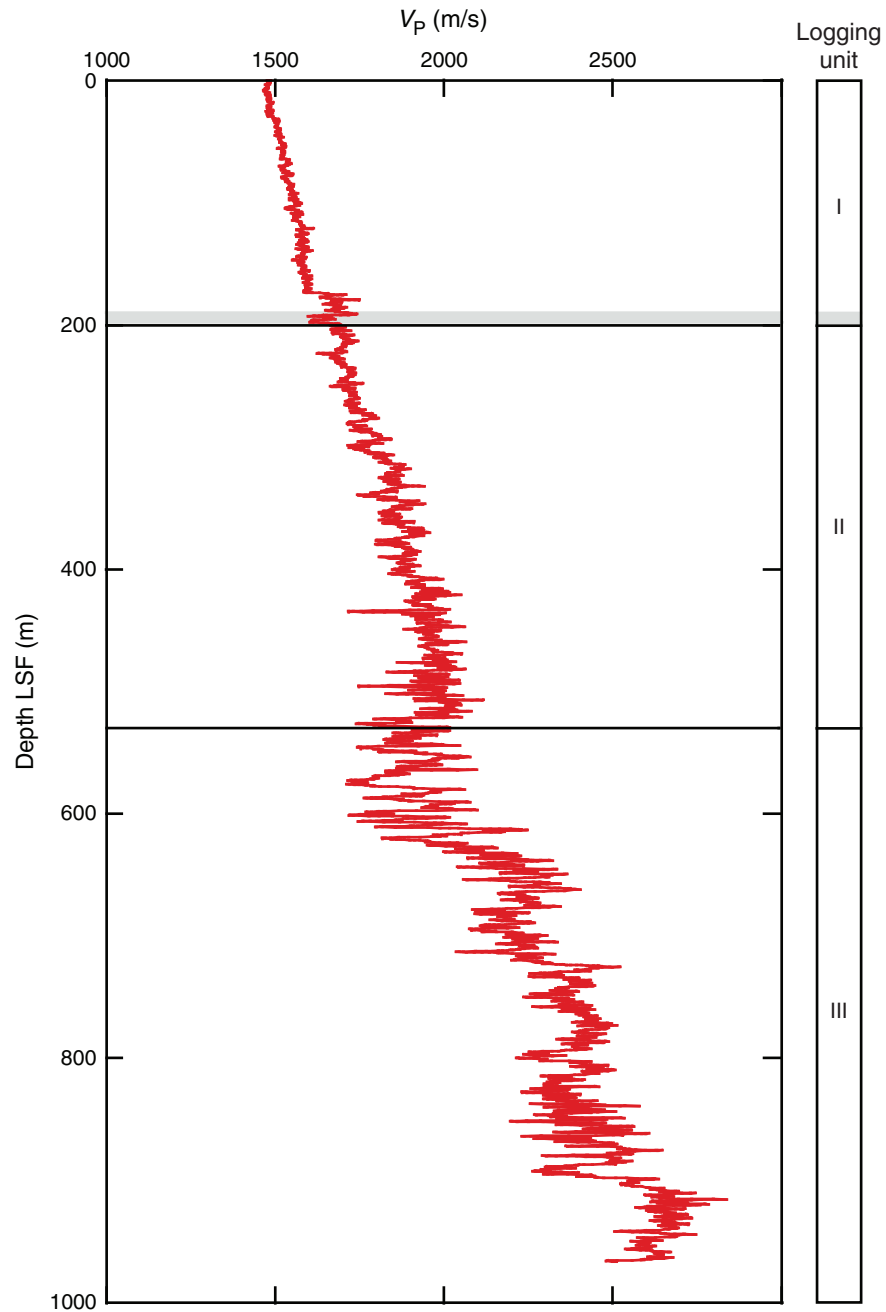
Figure F36. Bit resistivity–derived porosity in Hole C0001D using Archie's law with parameters $a = 1$ and $m = 2.4$ compared with Site 1175, 1176, and 808 core porosities. CSF = core depth below seafloor, LSF = LWD depth below seafloor.
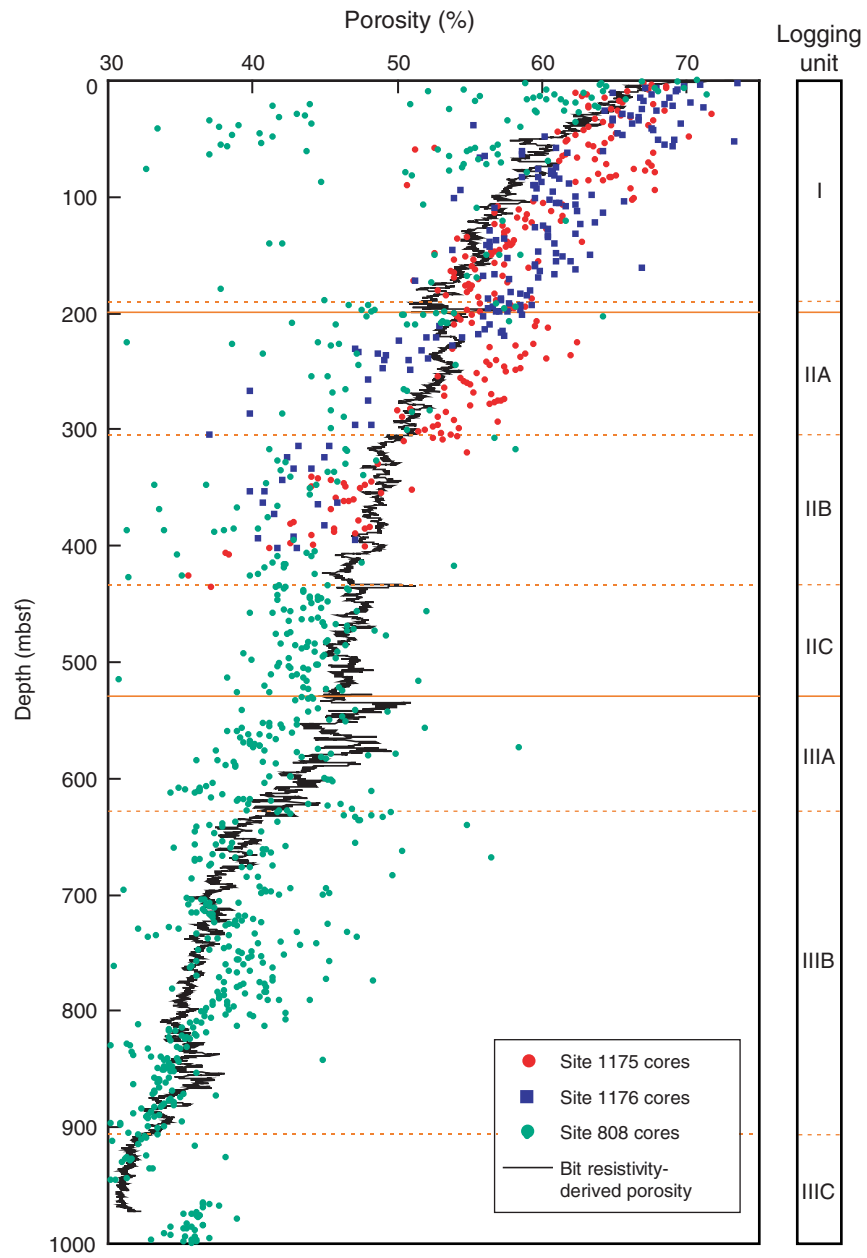
Figure F37. Bit resistivity–derived porosity using Archie's law with parameters *a* = 1 and *m* = 2.4 compared with porosity derived from IDRO and TNPH in Hole C0001D. LSF = LWD depth below seafloor.
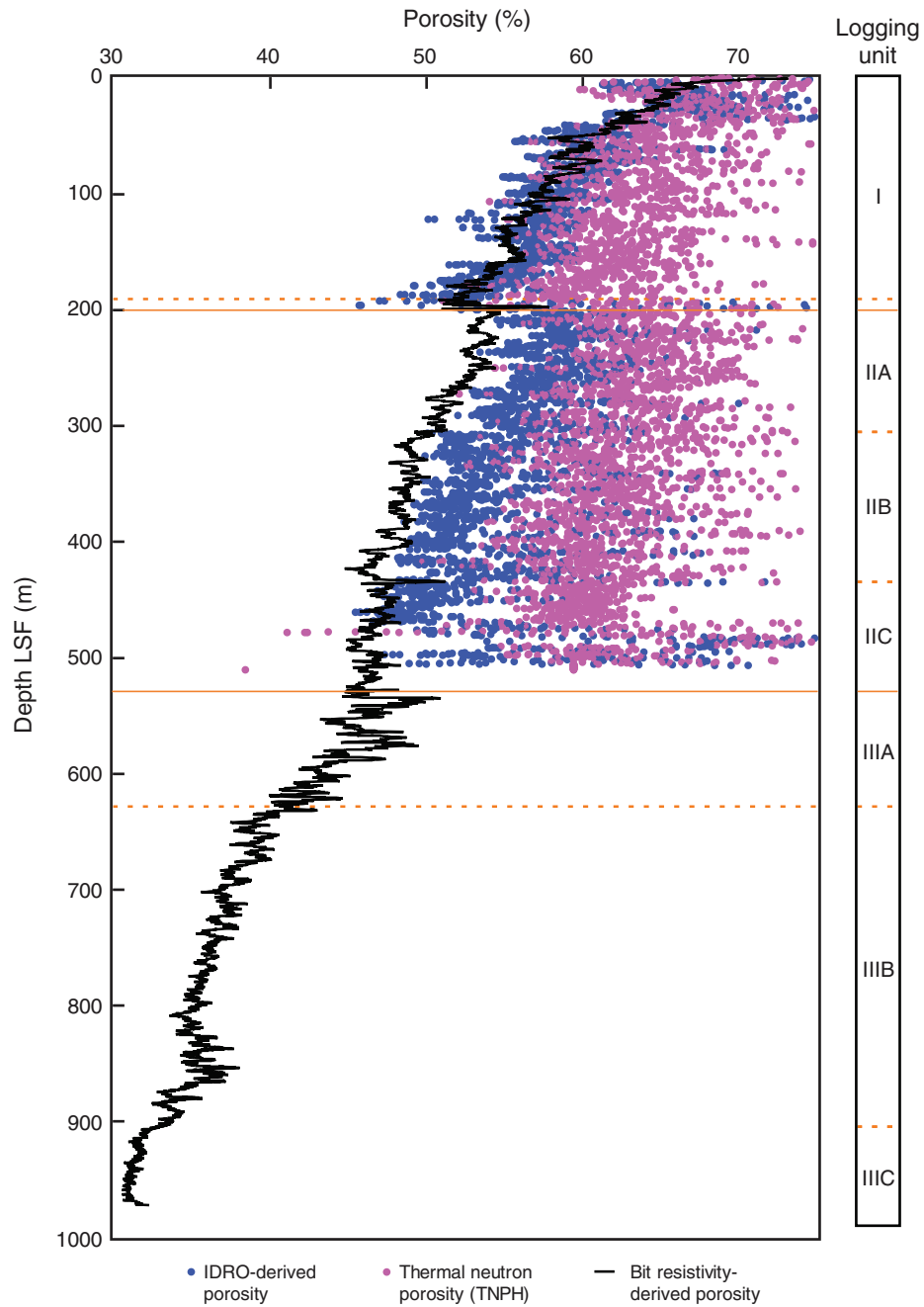
Figure F38. Relations between (**A**) sonic *P*-wave velocity and resistivity and (**B**) sonic *P*-wave velocity and resistivity-derived porosity.
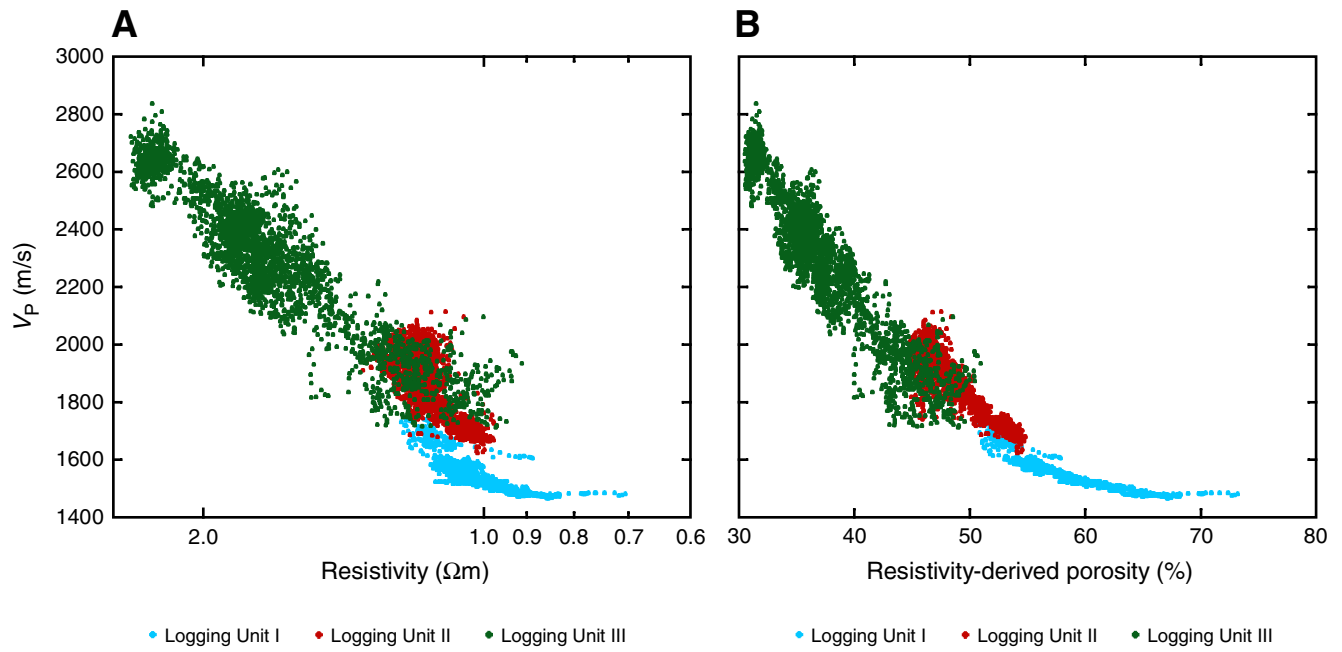
Figure F39. Shallow resistivity image (dynamic normalization) of Hole C0001D with measured bedding and fracture orientations and dips. Tadpole lines = dip direction of plane. LSF = LWD depth below seafloor.
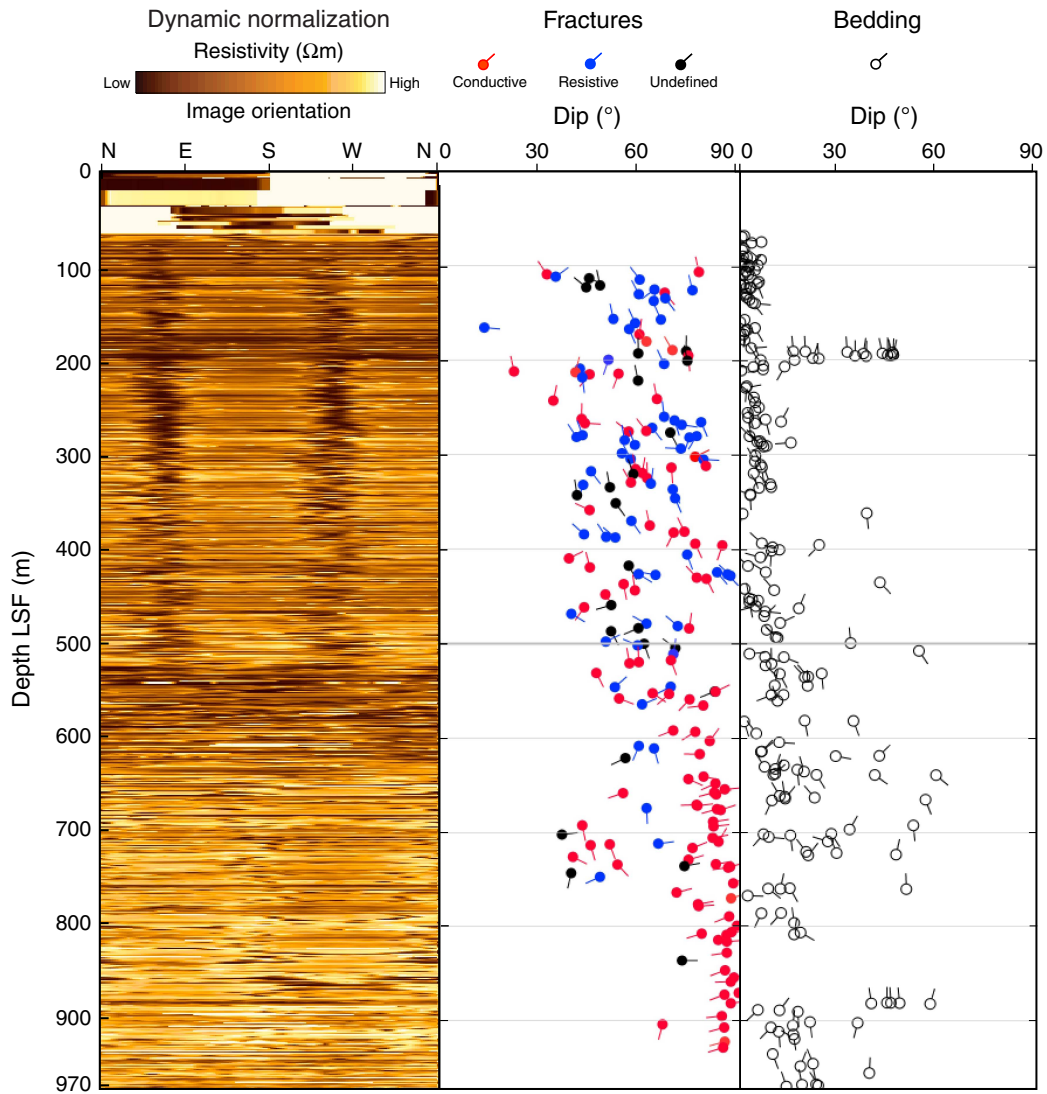
Figure F40. Equal-area lower hemisphere stereographic projection of (**A**) poles to bedding dips and (**B, C**) poles to fractures. Fracture poles are represented according to (**B**) resistivity and (**C**) fracture azimuth and dip divided into three classes. Class 1 pole trend = 040°–110° and 220°–290° (northwest–southeast trending planes), dip > 75°; Class 2 pole trend = 040°–110° and 220°–290° (northwest–southeast trending planes), dip < 75°; Class 3 pole trend = 110°–220° and 290°–040° (northeast–southwest trending planes), all dips. These divisions of azimuth represent natural breaks in the data. Rose diagrams represent fracture azimuths shown as dip direction – 90°.
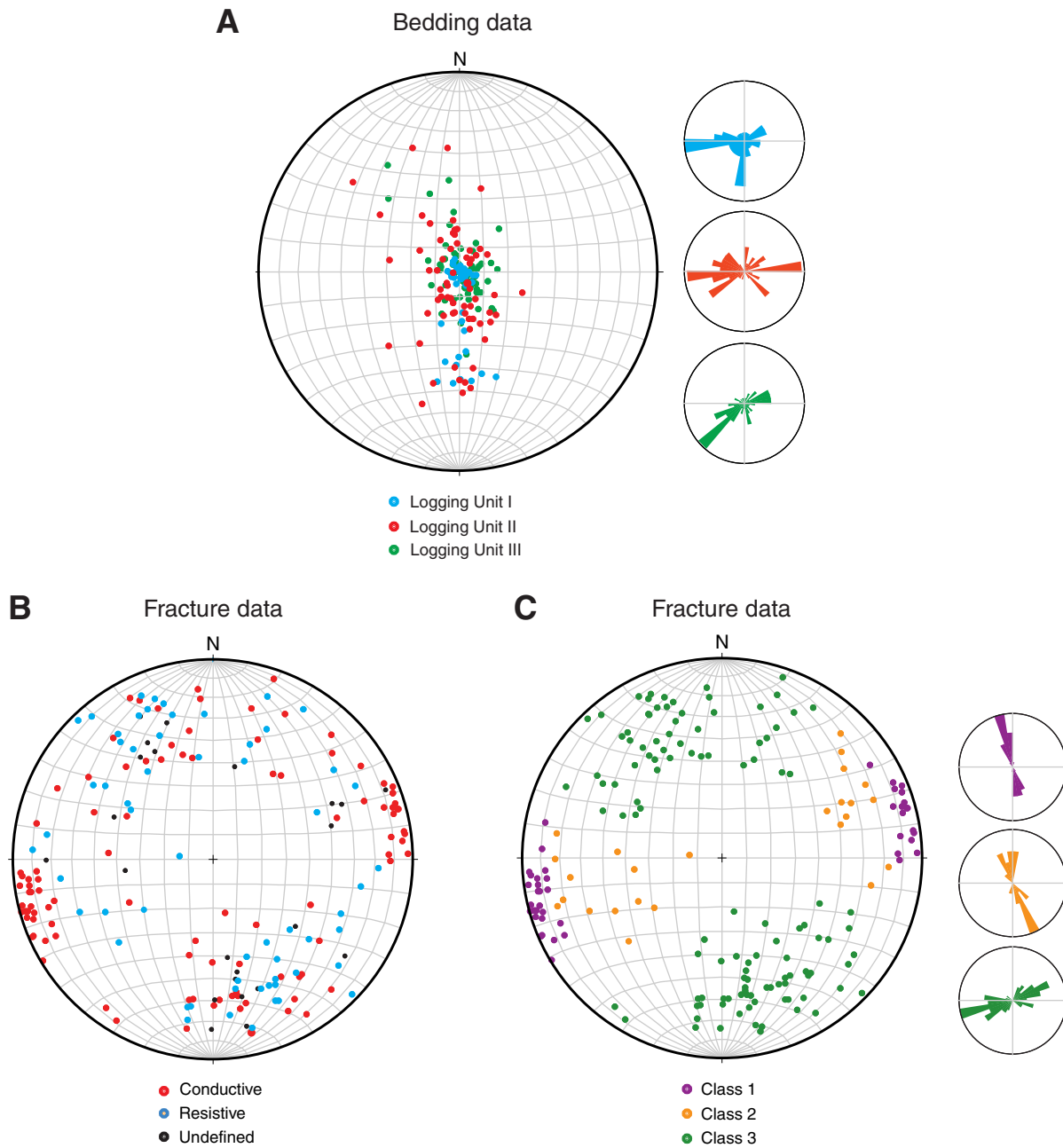
Figure F41. Close-up of resistivity image across logging Unit I/II boundary (187–207 m LWD depth below seafloor [LSF]). Subunit IB shows a systematic change and increase in bedding dip, whereas beds in Subunit IA and in the shallow part of Unit II are subhorizontal. Tadpole lines = dip direction of plane.

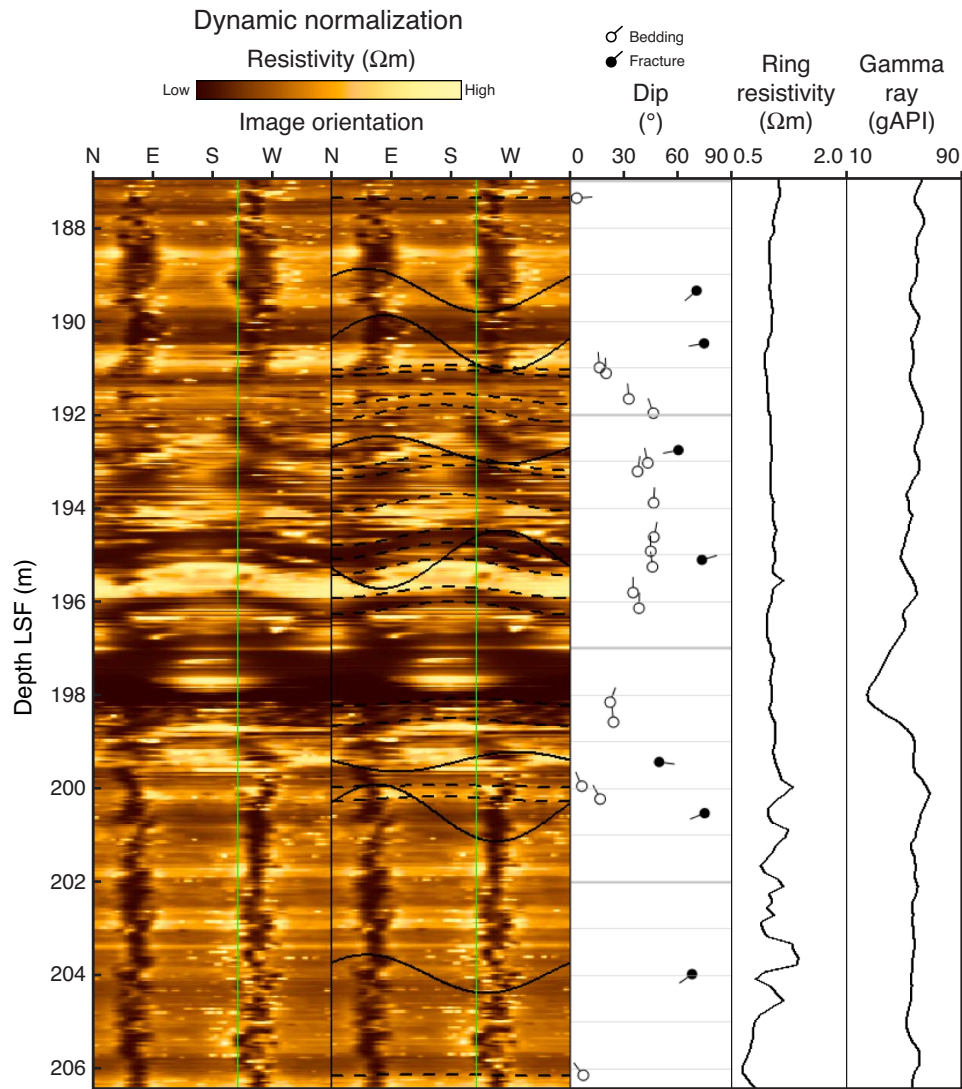**Figure F42.** Near-vertical undulating conductive fractures in the deepest part of Hole C0001D in shallow resistivity image (dynamic normalization). Examples shown suggest normal displacement by younger more shallowly dipping (~55°–75°) fractures. Fracture orientations are recorded as dip/dip direction. Tadpole lines = dip direction of plane. LSF = LWD depth below seafloor, 3-D = three-dimensional.
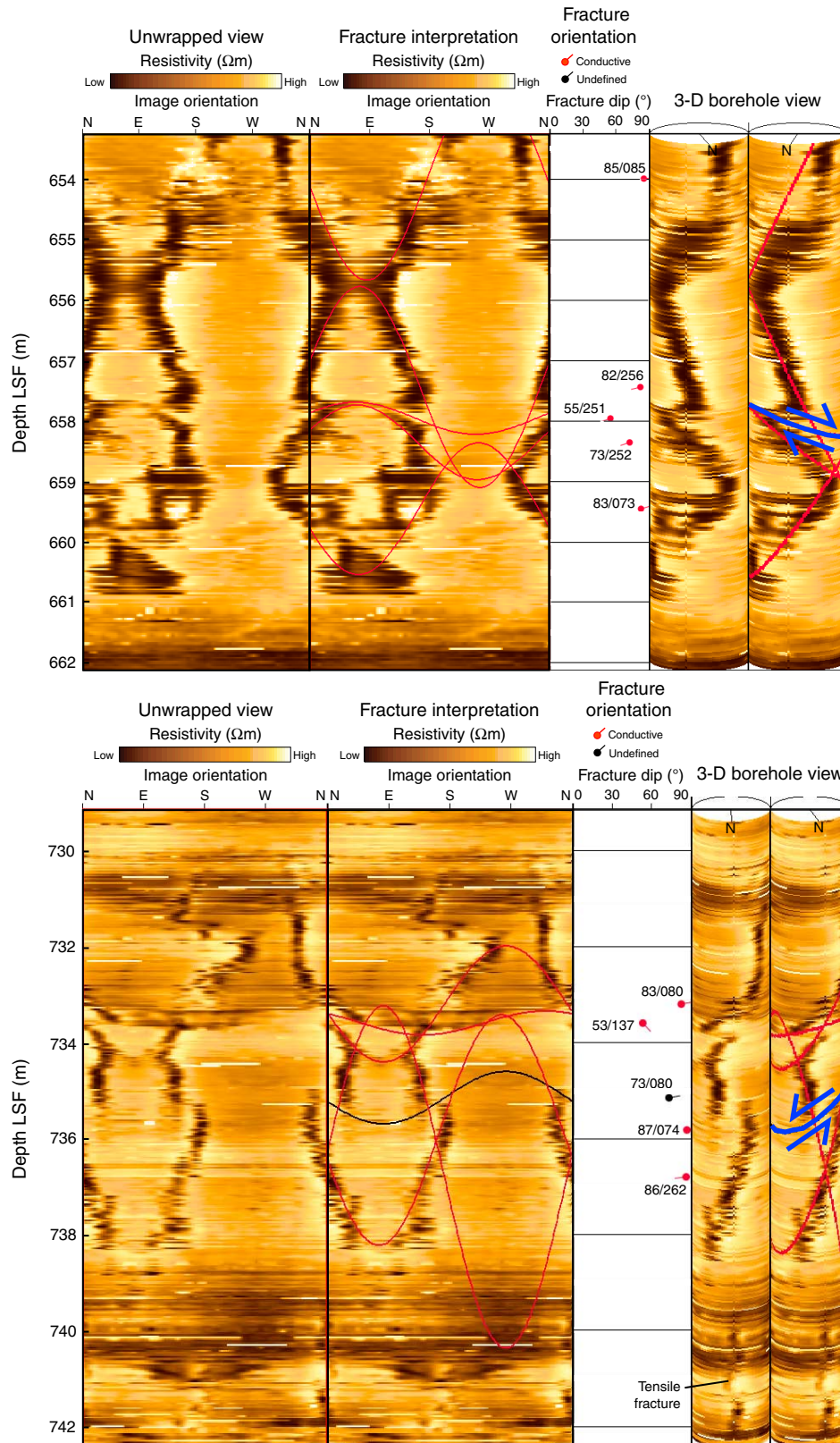
Figure F43. Images of disrupted zone at 543–565 and 577–599 m LWD depth below seafloor (LSF), showing range of disruption, including "block in matrix" texture (550–551 m LSF) and possible injection of more conductive sediment into more resistive sediment.
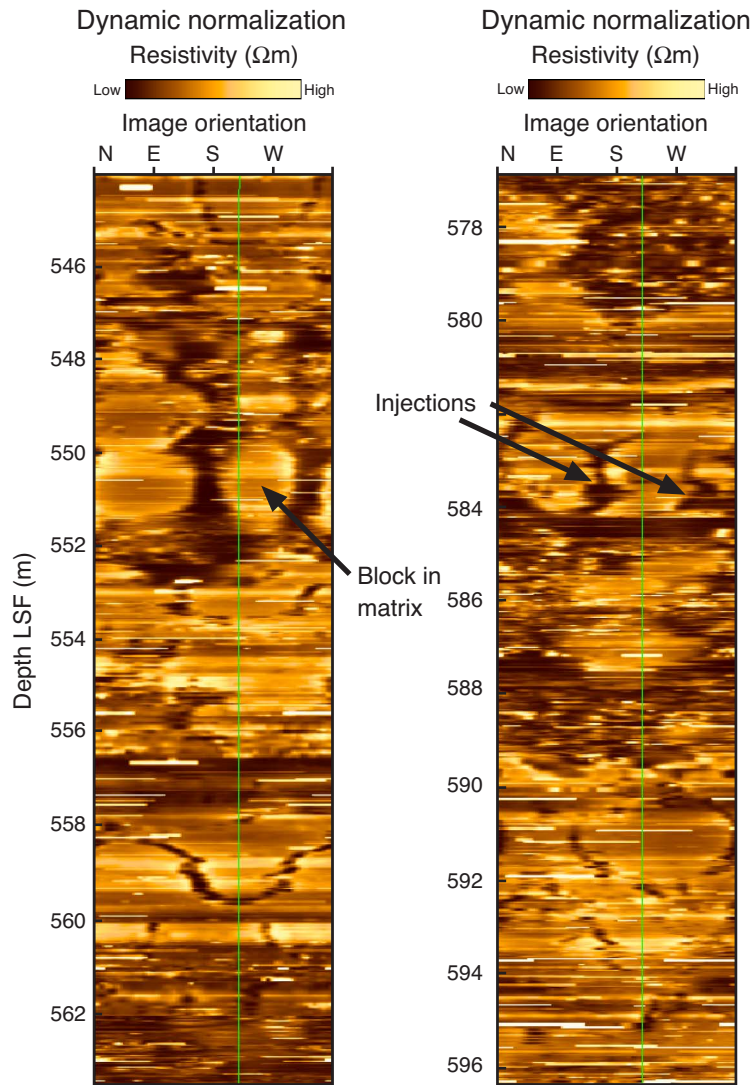
Figure F44. Resistivity image of breakouts and drilling-induced tensile fractures (66–88 m LWD depth below seafloor [LSF]).
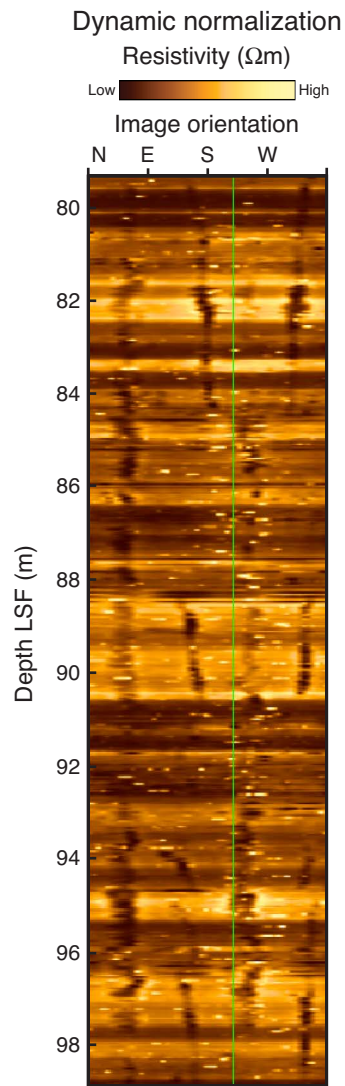
Figure F45. Azimuths and widths of borehole breakouts and drilling-induced tensile fractures in Hole C0001D. Std dev = standard deviation.
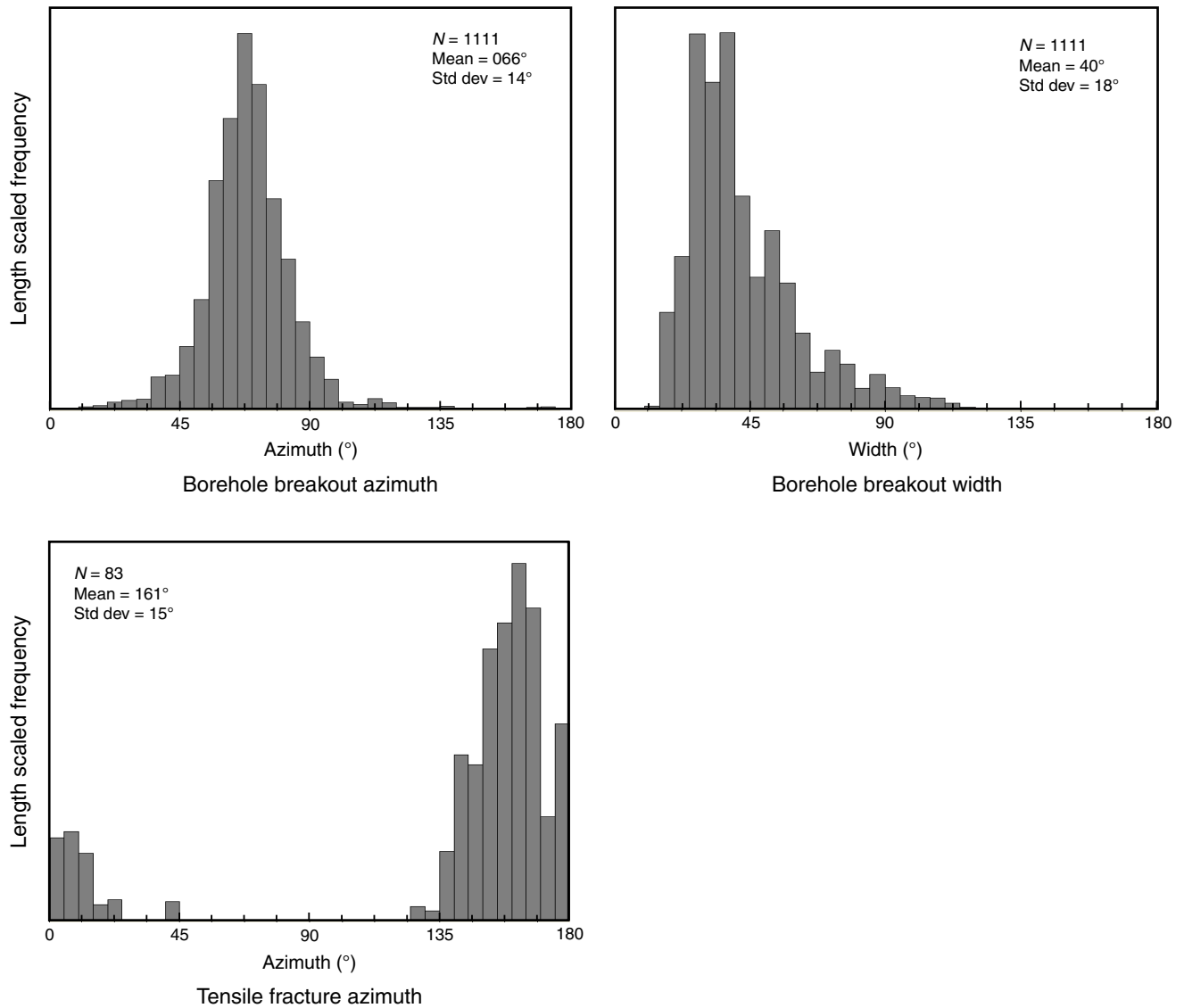
Figure F46. Stress polygons at depths in Hole C0001D where drilling-induced tensile fractures were detected. Possible ranges of in situ stress magnitudes indicated by tensile hoop stress criterion (red lines). **A.** 80 m LSF. **B.** 720 m LSF. **C.** 820 m LSF. **D.** 910 m LSF. APWD = annular pressure while drilling. Stress regime: NF = normal faulting, SS = strike-slip faulting, TF = thrust faulting. S_v = vertical stress.
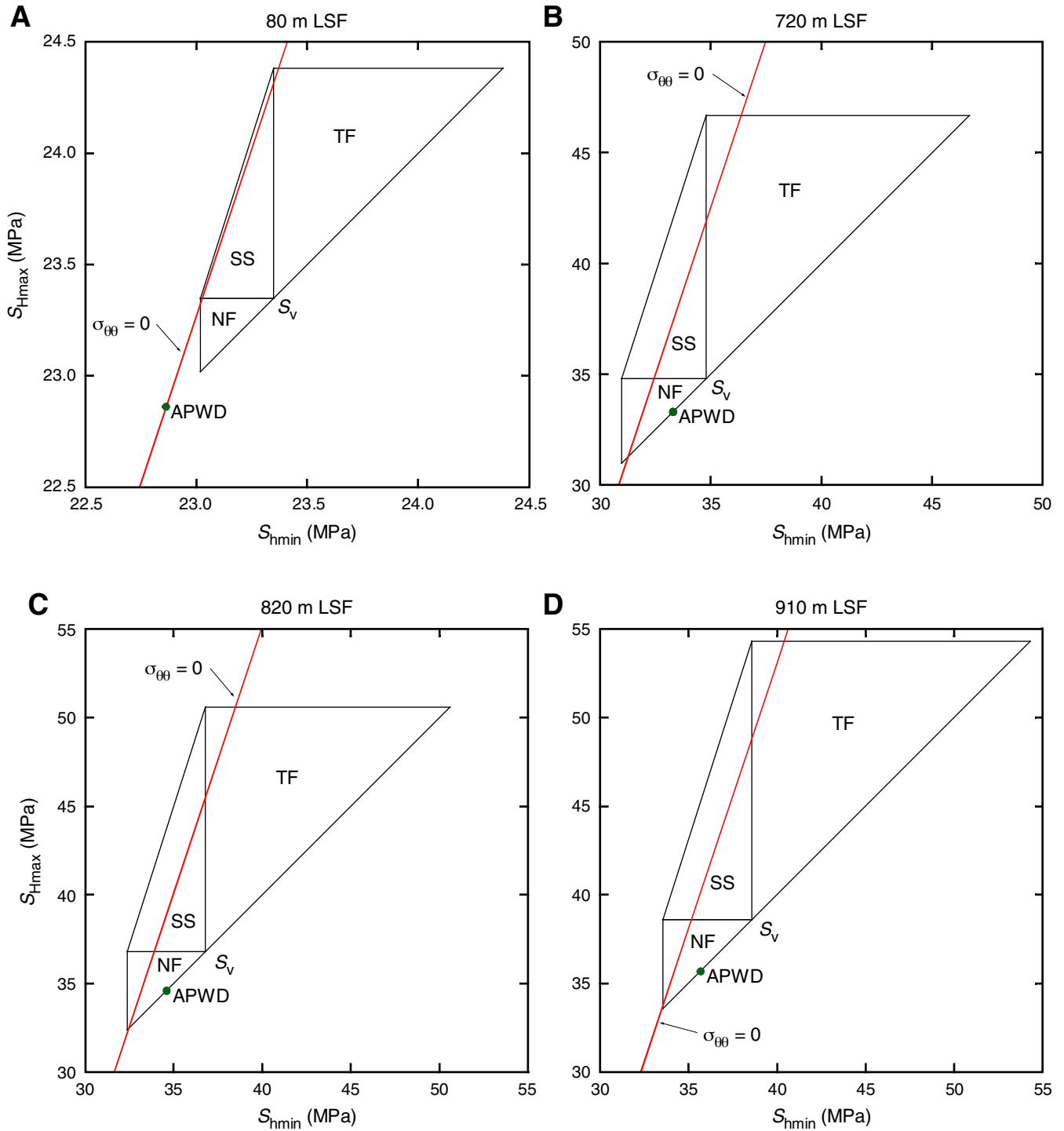
Figure F47. Check shot data for Hole C0001D. Each trace is the result of stacking selected shots fired while the tool was at a single depth. Red lines = first arrival picks. One-way traveltimes are from the seafloor to the depth of the seismicVISION tool. LSF = LWD depth below seafloor.
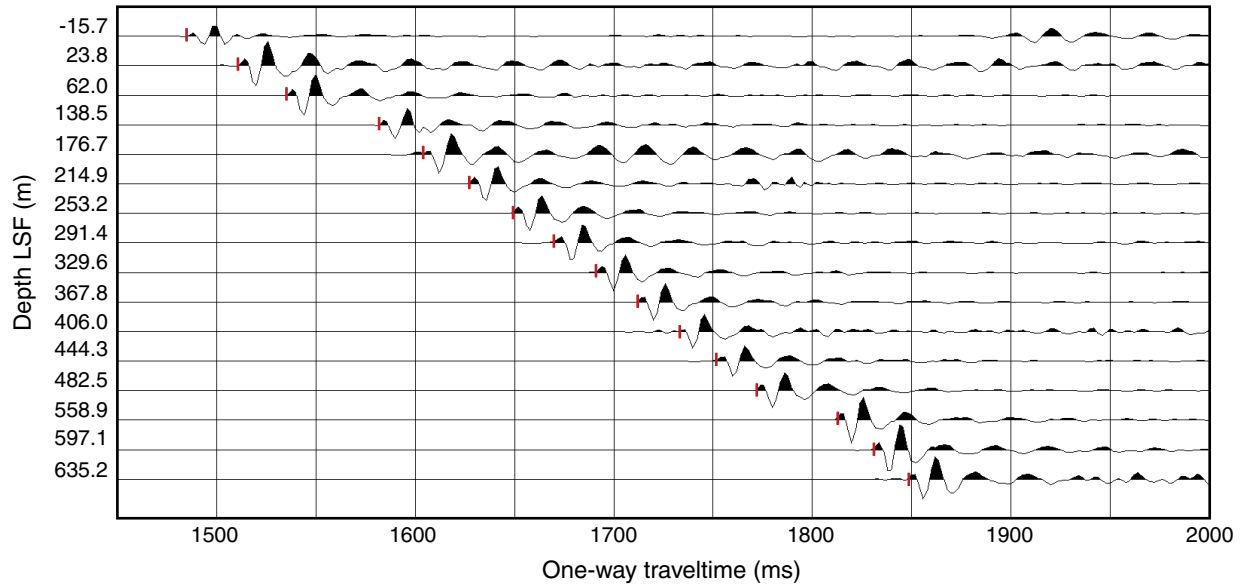
Figure F48. (**A**) Check shot arrival times and (**B**) interval velocities for raw and smoothed data. Smoothed arrival times are used for the synthetic seismogram generation and velocity depth conversion of seismic profiles at the site. LSF = LWD depth below seafloor.
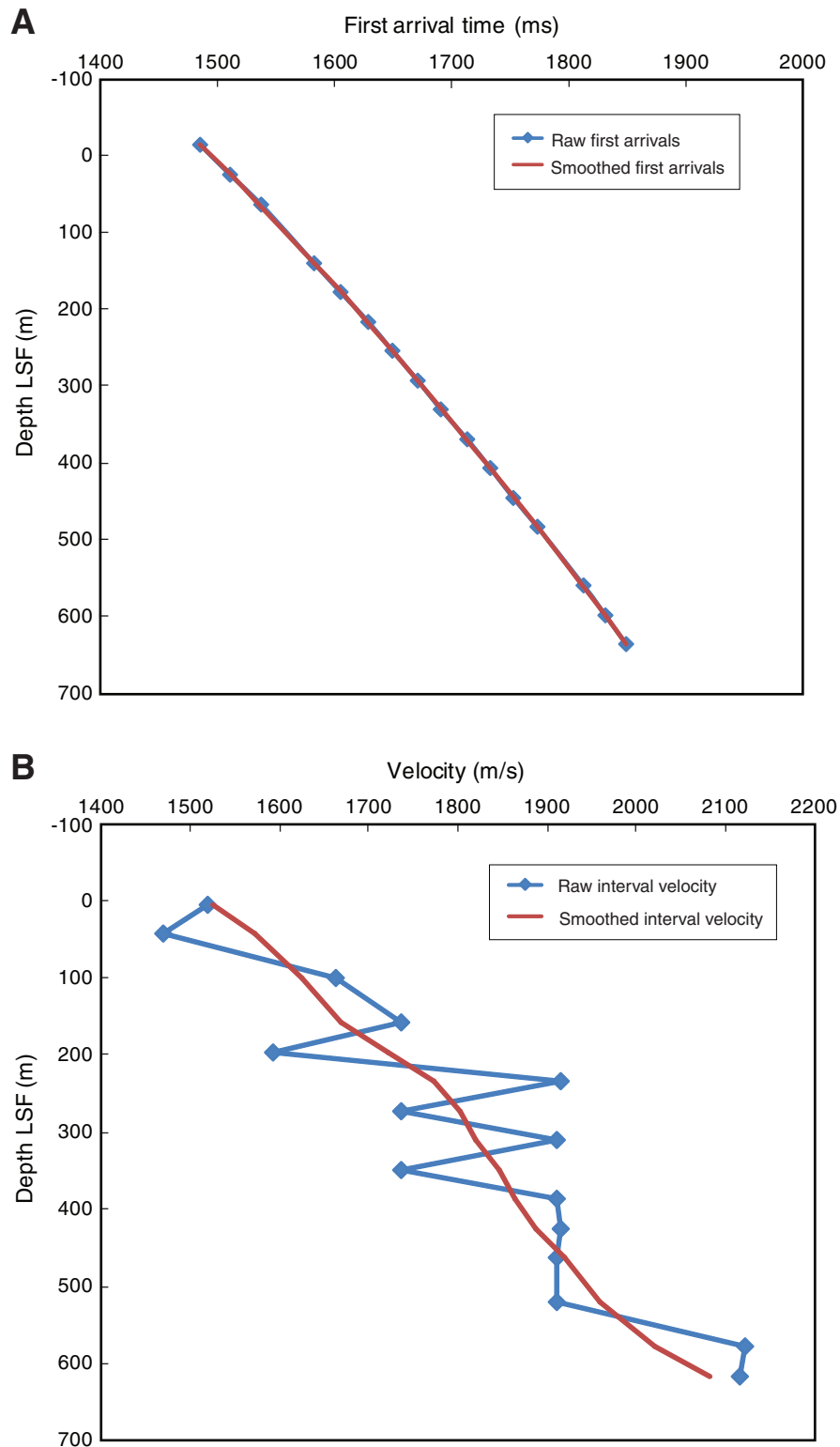
Figure F49. Comparison of smoothed interval velocities from check shot with processed sonic velocity log data. LSF = LWD depth below seafloor.
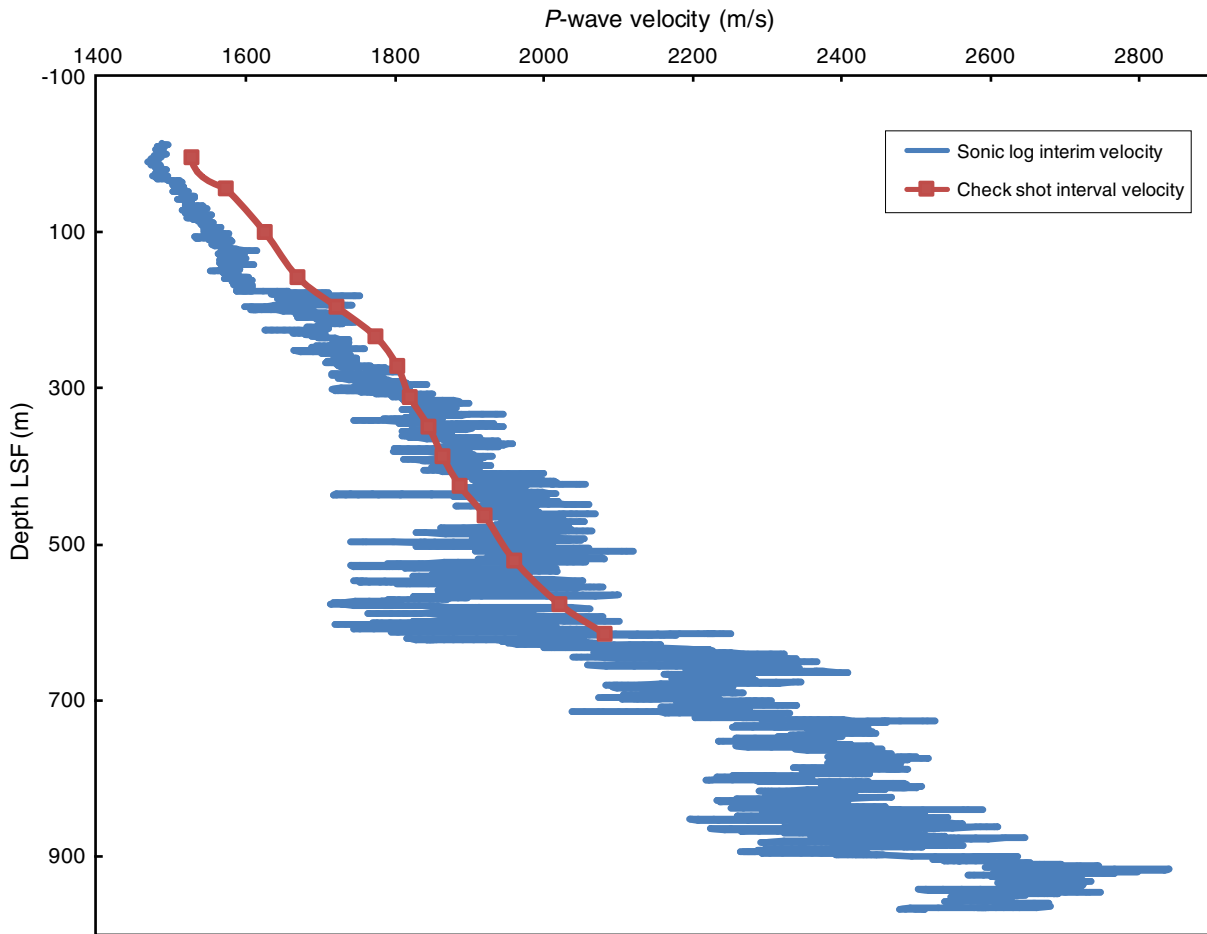
Figure F50. Density logs for Hole C0001D. **A.** Real-time (RT) bulk density log (RHOB). **B.** Density log with upper 49 m LWD depth below seafloor (LSF) real-time density values from Hole C0001C spliced into Hole C00001D. **C.** Pseudodensity log calculated from resistivity-derived porosity log. **D.** Spliced preferred density log for Site C0001 with set value for water column, real-time densities from 0 to 49 m LSF from Hole C0001C, real-time densities from 49 m LSF to just above 200 m LSF zone from Hole C0001D, and pseudodensities within 200 m LSF zone to total depth calculated from resistivity-derived porosity values. LRF = LWD depth below rig floor.
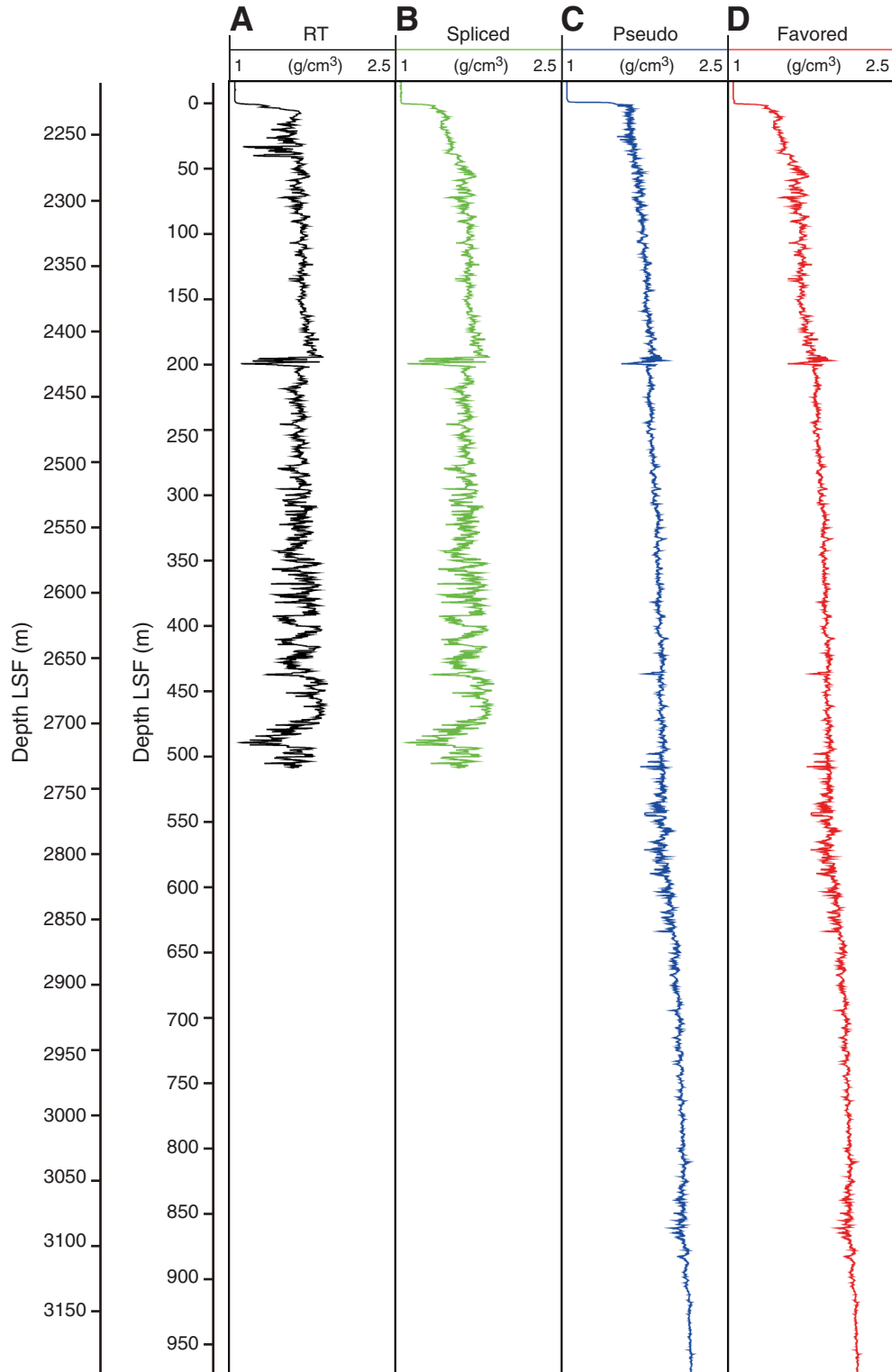
Figure F51. Comparison figure for synthetic seismogram generation for Hole C0001D. Source wavelet is 256 ms long with a 4 ms lag that was extracted at the borehole using a deterministic algorithm based on the power spectrum. **A.** Check shot allowing conversion from time to depth. TWT = two-way traveltime. **B.** Calibrated sonic log in slowness (DT). **C.** Spliced density log with real-time data above 192 m LWD depth below seafloor (LSF) and pseudodensity data to total depth. RHOB* = spliced bulk density measurement. **D.** Five identical traces showing the computed synthetic seismogram (Synth.). **E.** Reflection coefficients (Refl. coeff.) calculated from the sonic and density values at each depth. **F.** Source wavelet. **G.** Ten seismic traces on either side of the borehole from Inline 2680 of the three-dimensional volume. **H.** Gamma ray (GR) log.
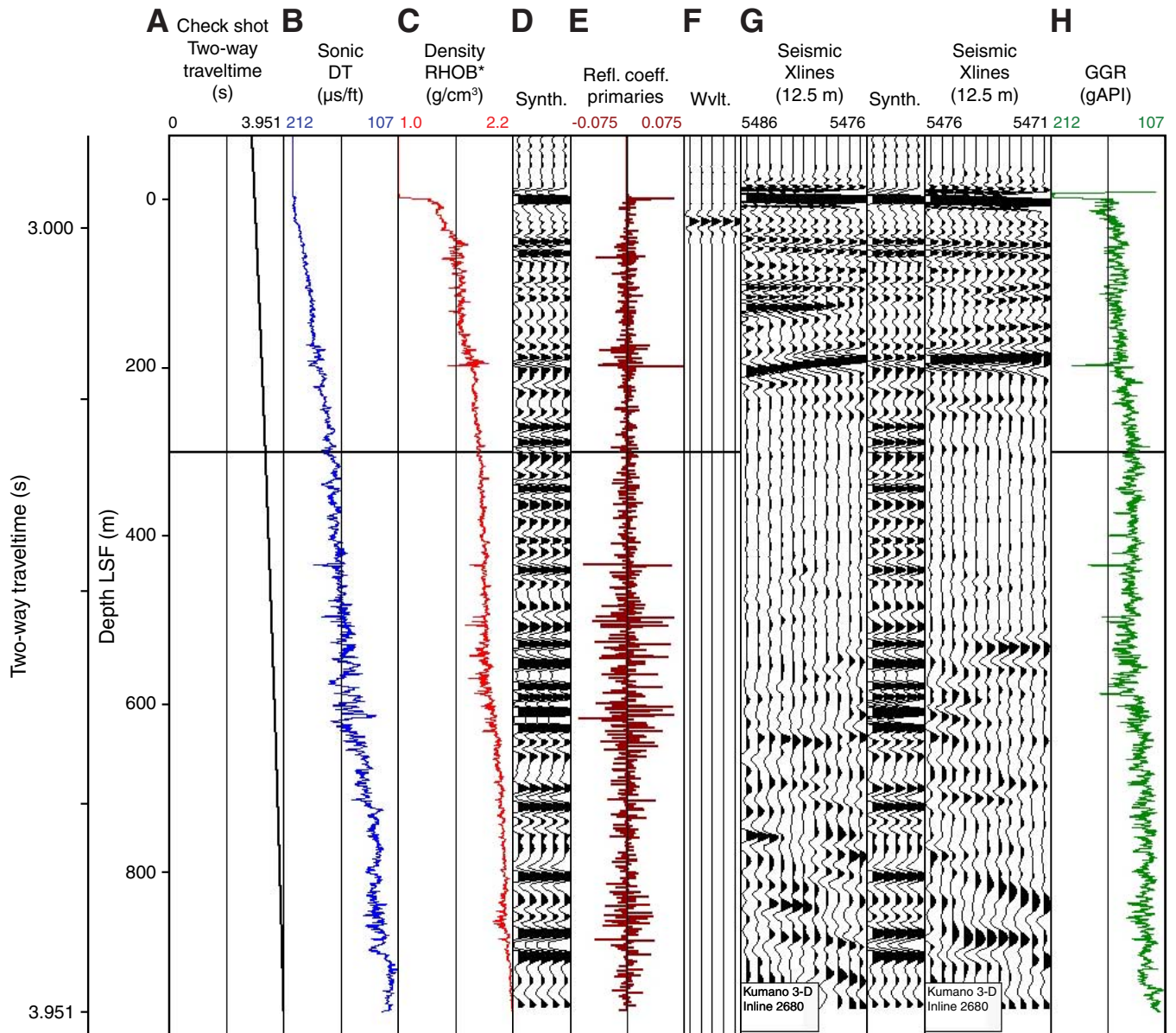
Figure F52. Seismic depth sections which intersect at Hole C0001D. These sections were formed by three-dimensional prestack depth migration. Strong positive reflector can be traced in the cross-line direction. SSL = seismic depth below sea level.
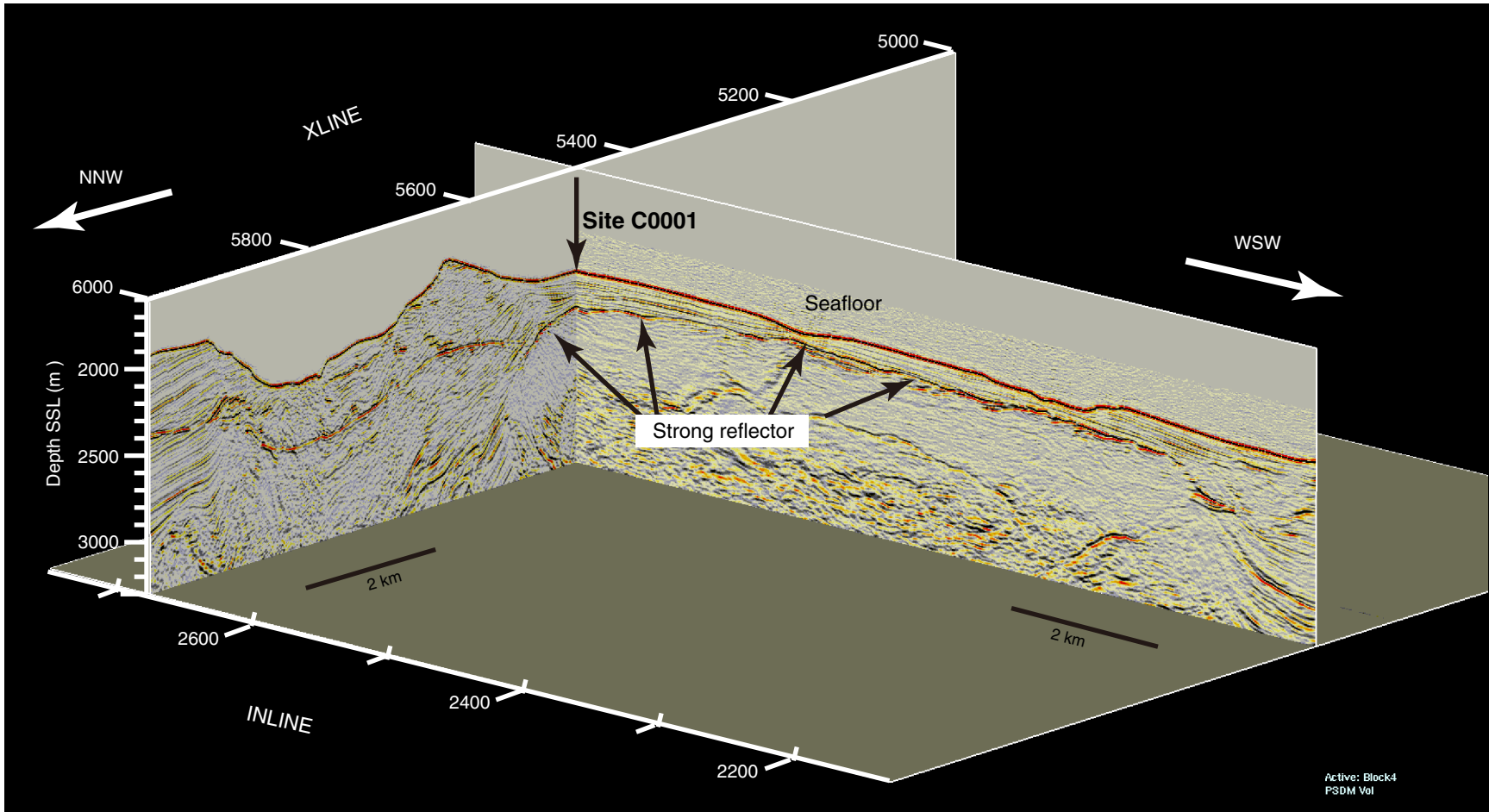
Figure F53. Distribution map of positive reflector at ~ 200 m SSF. Solid circle = Site C0001. The reflector is distributed across most of the width of the three-dimensional seismic survey area. The inset figure shows part of the 3D prestack time-migrated seismic section in the vicinity of Site C0001. Reflection events at ~ 3.2 s two-way traveltime (TWT) correspond to the ~ 200 m SSF zone. The character of the reflection events at ~ 3.2 s TWT is similar to that of the seafloor reflection at ~2.95 s TWT. This suggests that the reflector at ~ 3.2 s TWT has a waveform consistent with a positive polarity reflection.
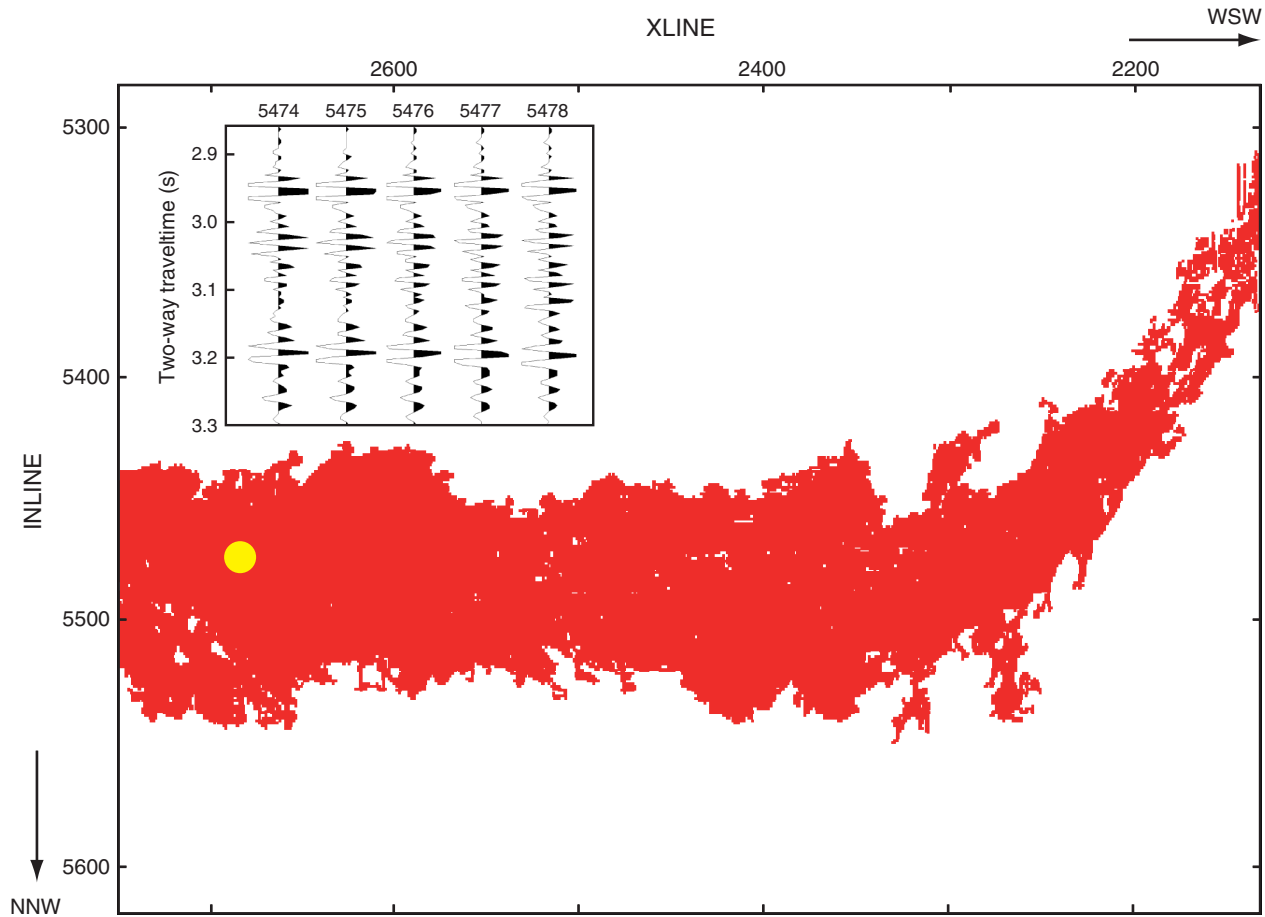
Figure F54. The 200 m layer with synthetic seismogram results that accompany changing the density values within the 5–8 m thick zone. Bulk density values (RHOB*) include measured, calculated, and modeled values. **A.** Favored merged density curve. **B.** Pseudodensity curve with a 1.5 m thick zone with 1.4 g/cm³ density. **C.** Pseudodensity curve with a 5.5 m thick zone with 1.4 g/cm³ density. **D.** Same zone as in C but with a sloping base. **E.** Pseudodensity curve with no zone. **F.** Pseudodensity curve with a 5.5 m thick zone with 2.1 g/cm³ density. **G.** 2.1 g/cm³ density boundary at the top of the zone that slopes back to measured densities over ~16 m. DT = slowness, Synth. = synthetic, Refl. coeff. = reflection coefficient, Wvlt. = source wavelet, GR = gamma ray value.

Table T1. Operations summary, Site C0001. (**See table notes.**) (**Continued on next page.**)

Hole C0001A
   Latitude: 33°14.2945'N
   Longitude: 136°42.7139'E
   Seafloor (drill pipe measurement from rig floor, m): 2228
   Distance between rig floor and sea level (m): 28.5
   Water depth (drill pipe measurement from sea level, m): 2199.5

Hole C0001B
   Latitude: 33°14.3135'N
   Longitude: 136°42.7252'E
   Seafloor (drill pipe measurement from rig floor, m): 2217.4
   Distance between rig floor and sea level (m): 28.5
   Water depth (drill pipe measurement from sea level, m): 2188.9

Hole C0001C
   Latitude: 33°14.3345'N
   Longitude: 136°42.7014'E
   Seafloor (drill pipe measurement from rig floor, m): 2226.5
   Distance between rig floor and sea level (m): 28.5
   Water depth (drill pipe measurement from sea level, m): 2198

Hole C0001D
   Latitude: 33°14.3286'N
   Longitude: 136°42.7040'E
   Seafloor (drill pipe measurement from rig floor, m): 2226
   Distance between rig floor and sea level (m): 28.5
   Water depth (drill pipe measurement from sea level, m): 2197.5

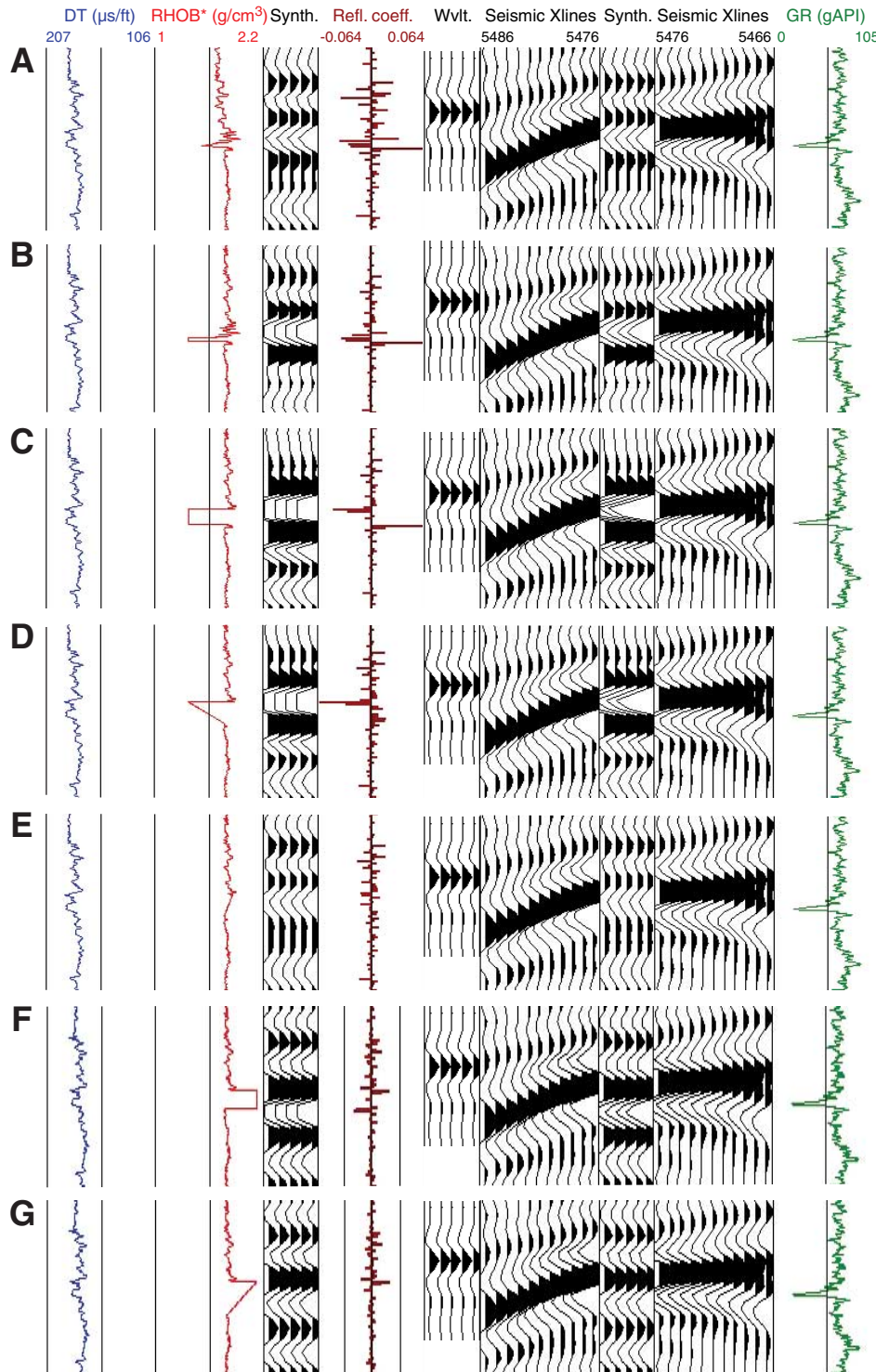| | Start | | Depth (m LSF) | | Drilled | |
| | Date (2007) | Local time (h) | Top | Bottom | (m LSF) | |
Operation						Comments
Hole C0001A pilot hole			0	1000	1000	8-1/2 inch MWD-APWD-GR
Tool preparation—tests	23 Sep	1430				
Tool rig up	23 Sep	1530				
Run into hole	24 Sep	0230				Delays resulted from GR shallow test and sinker bar release fall
ROV survey						
Tag seafloor	25 Sep	1200				
Spud-in	25 Sep	1215				
Reach total depth	27 Sep	1245				
Pull tools out of hole	27 Sep	1245				
Recover tools on rig floor	28 Sep	1200				Sign of packing off, stool stuck because of poor hole condition at 2623 and 2726 m DRF
Hole C0001B geotechnical coring hole			0	30.6	30.6	8-1/2 inch HPCS coring
Tool preparation	29 Sep	0315				
Coring	30 Sep	0000				
Hole C0001C LWD hole			0	77.5	77.5	8-1/2 inch LWD (GVR-sonic-SVWD-MWD-APWD-ADN)
Tool rig up	1 Oct	0000				
Install R/I source	1 Oct	0500				
Run into hole	1 Oct	0540				
Shallow test	1 Oct	0745				SVWD check shot test, repair geolograph failure
ROV survey	1 Oct	1840				
Tag seafloor	1 Oct	1840				
Spud-in	1 Oct	1915				
Deviation survey	2 Oct	0230				Deviation survey results: 6° at 2266 m DRF, 5.45° at 2304 m DRF
Reach total depth	2 Oct	0530				POOH at 2304 m DRF because of deviation
Pull tools out of hole	2 Oct	0530				Position nearby for new Hole C0001D
Hole C0001D LWD hole			0	976	976	8-1/2 inch LWD (GVR-sonic-SVWD-MWD-APWD-ADN)
ROV survey	2 Oct	0530				
Spud-in	2 Oct	0740				
Ream and sweep	3 Oct	1245				Sticky hole condition needed reaming and sweeping
Rig floor maintenance	4 Oct	0730				Short trip 2600 m DRF for WL BOP maintenance
Ream and sweep	4 Oct	1615				
Reach total depth	6 Oct	1030				adnVISION lost communication for real-time monitor
Pull tools out of hole	6 Oct	1200				
Recover tools on rig floor	7 Oct	0000				
Recover data	7 Oct	0100				GVR and sonic data recovered, SVWD data sent to Fuchinobe and ADN to China

Table T1 (continued).

Notes: DRF = drillers depth below rig floor, LSF = LWD depth below seafloor. MWD = measurement while drilling, APWD = annular pressure while drilling, ADN = Azimuthal Density Neutron tool (adnVISION). LWD = logging while drilling, GVR = geoVISION resistivity tool. sonic = sonic while drilling (sonicVISION), SVWD = seismicVISION while drilling, GR = gamma radiation. ROV = remotely operated vehicle. R/I = radioactive, POOH = pull out of hole, WL = wireline, BOP = blowout preventer, HPCS = hydraulic piston coring system, DRT = drillers depth below rotary table.

Table T2. Bottom-hole assembly, Hole C0001A. (**See table notes.**)

BHA component	Length (m)	Cumulative length from bit (m)
PDC bit	0.320	0.320
Stabilizer/float sub	1.500	1.820
Crossover sub	0.610	2.430
PNMDC	3.020	5.450
Crossover sub	0.481	5.931
Power pulse/APWD	8.650	14.581
Crossover sub	0.610	15.191
FG stabilizer	1.500	16.691
6-3/4 inch drilling collar	9.314	26.005
6-3/4 inch drilling collar	9.311	35.316
6-3/4 inch drilling collar	9.313	44.629
6-3/4 inch drilling collar	9.319	53.948
6-3/4 inch drilling collar	9.315	63.263
6-3/4 inch drilling collar	9.315	72.578
6-3/4 inch drilling collar	9.316	81.894
6-3/4 inch drilling collar	9.313	91.207
6-3/4 inch drilling collar	9.314	100.521
6-3/4 inch drilling collar	9.314	109.835
6-3/4 inch drilling collar	9.318	119.153
6-3/4 inch drilling collar	9.315	128.468
6-3/4 inch drilling collar	9.314	137.782
Jar	10.095	147.877
6-3/4 inch drilling collar	9.314	157.191
6-3/4 inch drilling collar	9.314	166.505
Crossover sub	0.610	167.115
Crossover sub	0.610	167.725
Crossover sub	0.610	168.335

Notes: BHA = bottom-hole assembly. PDC = polycrystalline diamond compact, PNMDC = pony nonmagnetic drill collar, APWD = annular pressure while drilling, FG = full gauge.

Table T3. Bottom-hole assembly, Holes C0001C and C0001D. (**See table notes.**)

BHA component	Length (m)	Cumulative length from bit (m)
PDC bit	0.320	0.320
Bit sub	0.610	0.930
Crossover sub	0.612	1.542
geoVISION	3.065	4.607
sonicVISION	7.620	12.227
Power pulse	8.555	20.782
seismicVISION	4.635	25.417
adnVISION	6.252	31.669
Crossover sub	0.610	32.279
6-3/4 inch drilling collar	9.315	41.594
6-3/4 inch drilling collar	9.319	50.913
6-3/4 inch drilling collar	9.313	60.226
6-3/4 inch drilling collar	9.315	69.541
6-3/4 inch drilling collar	9.316	78.857
6-3/4 inch drilling collar	9.313	88.170
6-3/4 inch drilling collar	9.315	97.485
6-3/4 inch drilling collar	9.314	106.799
6-3/4 inch drilling collar	9.314	116.113
6-3/4 inch drilling collar	9.318	125.431
6-3/4 inch drilling collar	9.315	134.746
6-3/4 inch drilling collar	9.314	144.060
Jar	10.095	154.155
6-3/4 inch drilling collar	9.314	163.469
6-3/4 inch drilling collar	9.314	172.783
Crossover sub	0.610	173.393
Heavy weight drill pipes	185.687	359.080
Crossover sub	0.610	359.690
Crossover sub	0.605	360.295

Notes: BHA = bottom-hole assembly. PDC = polycrystalline diamond compact.

Table T4. Quality control characteristics and sonic log data, Hole C0001D. (**See table notes.**)

Depth interval (m LSF)				
Top	Bottom	Zone	Quality	Comments
–12	0	1	0	Strong arrivals at ~203 μs/ft. No apparent change in the arrivals as the tool crosses the seafloor.
0	31	1	0	Strong arrivals at ~203 μs/ft. No apparent coherence at slowness less than mud velocity (Fig. **F7**).
31	84	1	0	Strong arrivals at ~200 μs/ft. Not clear if this is due to change in mud velocity. Occasional short (~1 m) increases in slowness of the mud arrival.
84	175	1	0	Strong arrivals at ~195 μs/ft. Not clear if this is mud velocity or the emergence of formation velocity.
175	192	1	1	Distinct formation and mud arrivals. Formation arrival variable around 180 μs/ft (Fig. **F8**).
192	202	1	0	No distinct separation between formation and mud arrival. Slowness varies around 195 μs/ft.
202	325	1	1	Distinct formation and mud arrivals. Formation slowness variable around 180 μs/ft and dropping gradually with depth (Fig. **F9**).
325	476	1	2	Distinct formation and mud arrivals. Coherence decreases, with occasional gaps several meters thick, in which picks are not clear. Formation slowness more variable with depth (Fig. **F10**).
476	524	1	2	Arrivals are more broken up in depth. The picks seem to be skipping between distinct arrivals creating noisy data with large slowness swings on a scale of 1–5 m.
524	589	2	2	Arrivals are broken up in depth. The picks seem to be skipping between distinct arrivals creating noisy data with large slowness swings on a scale of 1–5 m.
589	822	2	2	Arrivals are broken up in depth. The picks seem to be skipping between distinct arrivals creating noisy data with large slowness swings on a scale of 1–5 m. However, there seem to be longer sections 5–15 m that show continuous coherency and perhaps represent real slowness variability.
822	874	2	2	Large (10–20 m) gaps in coherent arrivals. Picks in this range are only sporadically reliable (Fig. **F11**).
874	964	1	2	Return to reasonable signal strength and coherence. There are still intervals with data gaps, but 10–20 m sections have continuous reliable data (Fig. **F12**).

Notes: LSF = LWD depth below seafloor. See **"Data and log quality."**

Table T5. Quality control characteristics and resistivity image data, Hole C0001D. (**See table notes.**)

Depth interval (m LSF)		Comments
Top	Bottom	
—	2	Start GVR rotation, beginning of image log
2	541	Excellent
541	543	Poor
543	602	Excellent
602	603	Poor
603	752	Excellent
752	867	Very good
867	990	Good
—	990	End of GVR image log

Notes: LSF = LWD depth below seafloor, GVR = geoVISION resistivity tool.

Table T6. Logging units, Site C0001. (**See table notes.**)

Depth (m LSF)	Logging		Interpretation	Description
	Unit	Subunit		
0–190.5	I	A	Hemipelagic mud and silty sediments	Slope sediments
190.5–198.9		B		Boundary sediments
198.9–305.4	II	A	Hemipelagic mud	
305.4–434.7		B		
434.7–529.1		C		
529.1–628.6	III	A	Mudstone	Thrust sheet
628.6–904.9		B		
904.9–TD		C		

Notes: LSF = LWD depth below seafloor. TD = total depth.

Table T7. Comparison of 25th and 75th percentile value ranges in gamma ray response between Site C0001 and Leg 196 Site 808. (**See table notes.**)

	Site C0001		Site 808			
Logging unit:	IA	II	1	2a and 2c	3	4a
Lithology	—	—	Sand and silt turbidites	Silt turbidites and hemipelagic mud	Clayey siltstone with ash/tuff	Ash/tuff and hemipelagic mud
Gamma ray (gAPI)	56–64	69–75	38–55	58–66	64–74	67–76
Breakouts	Yes	Yes	No	Yes	No	No

Notes: Gamma ray values are between 25th and 75th percentiles of values. See **"Log-based lithologic interpretation"** for comparison of Site C0001 and 808 gamma ray values and breakout occurrences.

Table T8. Check shot raw and smoothed traveltimes and calculated interval velocities, Site C0001. (**See table notes.**)

Depth* (m LSF)	Midpoint depth† (m LSF)	Raw		Smoothed	
		First arrival time* (ms)	Interval velocity† (m/s)	First arrival time* (ms)	Interval velocity† (m/s)
−15.7	4.05	1485.3	1519	1485.9	1525
23.8	42.90	1511.3	1469	1511.8	1572
62.0	100.25	1537.3	1663	1536.1	1624
138.5	157.60	1583.3	1736	1583.2	1668
176.7	195.80	1605.3	1591	1606.1	1720
214.9	234.05	1629.3	1915	1628.3	1773
253.2	272.30	1649.3	1736	1649.9	1801
291.4	310.50	1671.3	1910	1671.1	1819
329.6	348.70	1691.3	1736	1692.1	1845
367.8	386.90	1713.3	1910	1712.8	1863
406.0	425.15	1733.3	1915	1733.3	1886
444.3	463.40	1753.3	1910	1753.6	1919
482.5	520.70	1773.3	1910	1773.5	1959
558.9	578.00	1813.3	2122	1812.5	2021
597.1	616.15	1831.3	2116	1831.4	2082
635.2	—	1849.3	—	1849.7	—

Notes: Smoothed values were used in the generation of synthetic seismograms and time-depth conversion of seismic reflection profiles near the site. * = first arrival time picks associated with depths of observations, † = interval velocities associated with midpoints between depths of observations. LSF = LWD depth below seafloor. — = no data.